Trachyte phase relations and implication for magma storage conditions in the Chaîne des Puys (French Massif Central).

Caroline Martel, Rémi Champallier, Gaëlle Prouteau, Michel Pichavant, Laurent Arbaret, Hélène Balcone-Boissard, Georges Boudon, Pierre Boivin, Jean-Louis Bourdier, Bruno Scaillet

TRACHYTE PHASE RELATIONS AND IMPLICATION FOR MAGMA STORAGE CONDITIONS IN THE CHAINE DES PUYS (FRENCH MASSIF CENTRAL)

Caroline MARTEL[1,2,3*], Rémi CHAMPALLIER[1,2,3], Gaëlle PROUTEAU[1,2,3], Michel PICHAVANT[1,2,3], Laurent ARBARET[1,2,3], Hélène BALCONE-BOISSARD[4], Georges BOUDON[5], Pierre BOIVIN[6], Jean-Louis BOURDIER[1,2,3], and Bruno SCAILLET[1,2,3]

[1]Université d'Orléans, ISTO, UMR 7327, 45071, Orléans, France

[2] CNRS/INSU, ISTO, UMR 7327, 45071 Orléans, France

[3] BRGM, ISTO, UMR 7327, 45071 Orléans, France

[4]Institut des Sciences de la Terre de Paris (ISTeP), Univ Pierre et Marie Curie – CNRS, UMR 7193, Paris, France.

[5]Institut de Physique du Globe (IPGP), Paris, France.

[6]Laboratoire Magmas et volcans (LMV), Clermont-Ferrand, France.

*corresponding author

For submission to Journal of Petrology

ABSTRACT

Petrological data have been acquired on the natural trachytes from the Chaîne des Puys, French Massif Central, and on experimental products from phase equilibria in order to (i) constrain the storage conditions of the trachytic magmas that lead to explosive eruptions (dome destructions as block-and-ash flows or pumice-and-ash flows) and (ii) provide phase relationships and chemical compositions for differentiated alkaline liquids in intraplate continental context.

Phase assemblages, proportions, and compositions have been determined on six trachytes with SiO_2 contents varying from 62 to 69 wt % and alkali contents of 10.5-12.0 wt %. The samples contain up to 30 % of phenocrysts, mainly consisting of feldspar (15-17 %; plagioclase and/or alkali-feldspar), biotite (2-6 %; except in the SiO_2-poorest sample), Fe-Ti oxides (1-3 %) ± amphibole (< 5 %), ± clinopyroxene (~1 %). All samples have apatite and zircon as minor phases and titanite has been found in one sample. Pristine glasses (melt inclusions or residual glasses) in pumice from explosive events are trachytic to rhyolitic (65-73 wt % SiO_2 and 10.5-13.0 wt % alkali). H_2O dissolved in melt inclusions and the biotite+alkali feldspar+magnetite hygrobarometer both suggest pre-eruptive H_2O contents up to 8 wt %. These are so far the highest H_2O contents ever reported for alkaline liquids in an intraplate continental context. Melt inclusions also contain ~3400 ppm chlorine, ~700 ppm fluorine, and ~300 ppm sulphur.

Crystallisation experiments of the six trachytes have been performed between 200 and 400 MPa, 700 and 900°C, H_2O saturation, and oxygen fugacity of ΔNNO $\pm$1. The comparison between the natural and experimental phase assemblage, proportion, and composition suggests magma storage conditions at a pressure of 300-350 MPa (~10-12 km deep), melt H_2O content ~8 wt % (close to saturation), an oxygen fugacity close to ΔNNO~0.5, and temperatures increasing from 700 to 825°C with decreasing bulk SiO_2 of the trachyte. The high H_2O contents of the trachytes show that wet conditions may prevail during the differentiation of continental alkaline series.

Regardless of the size of the magma reservoir assumed to have fed the trachyte eruptions, calculation of the thermal relaxation timescales indicates that the tapped reservoir(s) are likely to be still partially molten nowadays. The four northernmost edifices may correspond to a single large reservoir with a lateral extension of up to 10 km, which could be possibly reactivated in weeks to months if intercepted by new rising basalt batches.

Keywords: trachyte - alkaline series – phase relationships – pre-eruptive conditions – Chaîne des Puys

INTRODUCTION

Alkali-rich magmas can produce highly explosive eruptions as illustrated by Vesuvius volcano (Italy, 79 AD), Phlegrean Fields (Italy, 39 ky BP), Neapolitan Yellow Tuff (Italy, 12 ky BP), Tenerife recent eruptions (Spain, 1563 AD and 1640 AD) or Tambora (Indonesia, 1815). However, while many studies have been carried out on phase relationships in rhyolitic or granitic systems (e.g., Tuttle & Bowen, 1958; Holtz & Johannes, 1991; Scaillet *et al.*, 1995) and calc-alkaline series (e.g., Rutherford *et al.*, 1985; Martel *et al.*, 1999; Prouteau & Scaillet, 2003) there is comparatively less information on evolved alkaline compositions. Most of the studies concern phonolites (Berndt *et al.*, 2001; Signorelli & Carroll, 2002; Freise *et al.*, 2003; Harms *et al.*, 2004; Andujar *et al.*, 2008; Scaillet *et al.*, 2008) and peralkaline rhyolites (e.g. Scaillet & Macdonald, 2001, 2003; Di Carlo *et al.*, 2010), whereas trachytes have received much less attention (Nelson & Hegre, 1990; Nekvasil *et al.*, 2004; Fowler *et al.*, 2007; Fabbrizio & Carroll, 2008). Petrological approaches combining characterization of natural products and experimental phase relationships have been shown to be particularly powerful for the determination of pre-eruptive conditions, such as reservoir depth, temperature, and melt volatile content (e.g., Gardner *et al.*, 1995; Martel *et al.*, 1998; Prouteau & Scaillet, 2003). Yet, only a few of such studies have been dedicated to the determination of storage conditions of trachytic magmas (i.e. Phlegrean Fields; Fabbrizio & Carroll, 2008; Fabbrizio *et al.*, 2009), leading to the conclusion that this class of magmas may hold a significant amount of dissolved water. Significant amounts of gases, combined to their silica-rich nature, make trachytes prone to explosive behaviour, through processes that need to be fully understood in order to minimize the associated risks.

Beyond volcanological purposes, trachytes and alkaline rhyolites represent end-members of the alkaline magmatic series, whose origin is still a matter of debate (e.g., Nekvasil *et al.*, 2004). In particular, several processes have been proposed to explain the alkaline affinity (e.g., Scaillet & Macdonald, 2003; Caricchi *et al.*, 2008) or the transition between silica-undersaturated and silica-oversaturated magmatic trends (e.g. crystallisation of non-stochiometric minerals, amphibole crystallisation, contamination by the continental crust), but the mechanisms that apply in specific cases still need clarification. The Chaîne des Puys (CDP) suite represents a world reference in continental alkaline series (Maury *et al.*, 1980; Villemant *et al.*, 1980), displaying a continuum from alkali basalts to trachytes, interpreted as resulting from fractional crystallisation in a nearly closed system. The CDP thus represents an ideal case for further investigation via experimental petrology.

In this study, we have acquired new petrological data on the CDP trachytes and we compared them to experimental phase equilibria performed on the same rocks, in order to determine (i) the pre-eruptive conditions of the trachytic reservoirs beneath the CDP volcanoes and (ii) phase relationships in differentiated alkaline series between 200 and 400 MPa.

VOLCANOLOGICAL SETTING AND SAMPLE SELECTION

Tertiary to Quaternary volcanism in the French Massif Central produced typical intraplate alkaline series (e.g., Villemant *et al.*, 1980) that have erupted during two major episodes: Oligocene to early Miocene and upper Miocene to Plio-Quaternary. Of the many volcanic fields formed in this time span, the CDP is the northernmost and among the youngests (ca 100 to 5-7 ky). The chain consists of a narrow (3-4 km wide and ca 30 km long) NS-trending group of about 80 monogenetic volcanoes, in the eastern vicinity of Clermont-Ferrand city. As it features spectacular fresh volcanic morphologies, the CDP has been one cradle of volcanology as a science and since then has remained the subject of a considerable geological literature. The modern volcanological knowledge acquired in the last three decades has been summarized in successive versions of a volcanological map of the CDP at the 1/25000 scale and its accompanying booklet (first edition by Camus *et al.*, 1975, last edition by Boivin *et al.*, 2009). The CDP volcanoes include a variety of volcanic forms and structures, i.e. mostly scoria cones and a few phreatomagmatic maars, silicic explosive craters, and lava domes. The CDP lavas provide a good example of a differentiation series produced by fractional crystallisation (Maury *et al.*, 1980, Villemant *et al.*, 1981) that ranges from slightly K-rich, alkali basalts to mugearites and less voluminous benmoreites and trachytes. About 8 km^3 of basalts were emitted as lava flows during 90 ky, in addition to 1-2 km^3 of trachytic derivatives which were extruded mostly as lava domes (Boivin *et al.*, 2009).

Trachytic eruptions in the CDP produced 7 discrete lava domes or spines (i.e. Kilian, Vasset, Puy de Dome, Clierzou, Aumone, Grand Sarcouy and Chopine volcanoes), the growth of which may have been preceded by explosive episodes. These explosive events are in some cases evidenced by conspicuous small-size (ca 1 km wide) explosive craters cut within the basement rocks (Kilian and Vasset volcanoes) and by related pumice-rich pyroclastic deposits (Kilian and Puy Chopine). Early explosive episodes cannot be proved nor ruled out for the other volcanoes, as craters from an early phase might be concealed beneath the lava domes.

The growth of lava domes and spines may have been accompanied by destabilizations into pyroclastic density currents (e.g. at Puy de Dome and Grand Sarcouy) or more explosive events (e.g. at Puy Chopine). For each event, the total volumes emitted are less than 0.5 km^3. Trachytic activity in the CDP has been restricted in both time and space. The 7 volcanoes cluster along a 4 km segment in the central part of the chain and thorough dating of the edifices yields ages falling within the range 9-15 ky (Miallier *et al.*, 2004; Boivin *et al.*, 2009).

Of the 7 trachytic volcanoes of CDP, 6 are included in this study. The Aumone trachyte is not considered as it is very similar to the nearby Clierzou in mineralogy, chemical composition and age. Most of the trachyte samples used herein (Table 1) come from massive lava bodies, i.e. lava domes and spines: Grand Sarcouy (SAR), Clierzou (CLI), Puy de Dôme (DOM), Chopine (CHO), Kilian (KIL). The other samples are juvenile clasts from pyroclastic deposits: Vasset (VAS) and pumice from explosive events of Chopine (CHO_Pumice) and Kilian (KIL_Pumice) (Figure 1). These two pumiceous samples will be more specifically used for glass analyses. Indeed, pumice from explosive events likely experienced faster magma ascent rates and quenching than dome lavas, thus better preserving the trapped volatiles in melt inclusions and preventing extensive crystallisation of the residual glasses (Martel *et al.*, 2000).

EXPERIMENTAL AND ANALYTICAL METHODS

Experimental methods

Starting material

The experiments were performed in parallel on all trachytes. Block samples, either from the lava dome or pyroclastic deposit, were fused in a Pt-crucible at 1400°C and 1 atm for 3 hours and powdered in an automatic mortar (grain size < 50 µm). The cycle of fusion and grinding was repeated once in order to ensure chemical homogeneity of the starting glasses.

Around 30-50 mg of the glass powder and enough deionized H_2O to achieve H_2O saturation at the target *P-T* were introduced in Au-capsules (2.5 mm ID, 2.9 mm OD, and 20 mm long) and sealed by arc-welding.

Equipment and run procedure

For each run, the six capsules were loaded together in an internally-heated pressure vessel pressurized with an Ar-H_2 gas mixture. Total pressure was continuously recorded by a transducer calibrated against a Heise Bourdon tube gauge, giving an uncertainty of $\pm$20 bars (including daily fluctuations). The capsules were placed at the hotspot of a Mo-windings furnace, where the thermal gradient is less than 5°C over ~3 cm. The furnace temperature was regulated by a Eurotherm controller and sample temperature was read continuously by S-type thermocouples with given uncertainty of $\pm$5°C. In order to keep the oxygen fugacity (f_{O2}) within ~1 log unit around the Ni-NiO buffer (NNO), 0.1 MPa of pure hydrogen was added cold to the Ar gas for each experiment (Martel *et al.*, 1999). Run durations varied from 2 to 17 days, typically increasing with decreasing temperature. Phases were compositionally homogeneous, attesting for chemical equilibrium. The samples were isobarically quenched by switching off the furnace power, inducing a temperature drop of ~100°C/min. The capsules that did not lose weight during experiments were opened for analyses.

Analytical methods

Phase identification

Few clasts of each charge were embedded in epoxy resin and polished for analysis using a scanning electron microscope (SEM; JEOL JSM-6400, ISTO). For the purpose of studying glass inclusions trapped in phenocrysts, the number of investigated crystals was optimized by hand picking from gently crushed pumice (sieved to the 500-1000 µm fraction). The extracted crystals were mounted into resin blocks for glass inclusion identification using the SEM.

Major elements

The natural and experimental samples were analysed using an electron microprobe (EMP; Cameca SX50, BRGM-ISTO) with an acceleration voltage of 15 kV, counting time of 10 s, and beam current of 6 nA (glasses) or 10 nA (crystals). The beam size was focussed (~2 µm) for mineral phases and enlarged to a spot of 8x8 μm^2 for glasses, in order to minimize alkali migration. EMP analytical errors are 1 % for SiO_2, Al_2O_3, and CaO, 3 % for FeO, MgO, and TiO_2, 5 % for MnO, Na_2O, and K_2O, ~300 ppm for P_2O_5, ~500 ppm for Cl and S, and 700 ppm for F.

Na_2O tends to volatilize during sample fusion (preparation of the starting glass for the experiments) and during EMP analyses under the electron beam. In order to evaluate the total Na loss during fusion and EMP analyses, the Na_2O content of the trachyte from Puy Chopine was analysed by atomic absorption spectrophotometry (AAS; Hitachi Z-8100, ISTO). The whole-rock finely-ground powder was dissolved by HF attack and diluted before AAS analysis. The Na_2O contents obtained by AAS (6.84 wt %) was compared to the Na_2O content measured by EMP on the dry and hydrated fused trachyte, because Na volatilization tends to be greater in H_2O-rich glasses (Pichavant, 1987). For glasses with 6.9 to ~10 wt % dissolved H_2O, the Na correction factor was about 1.23. Since our experiments were performed within this relatively restricted range of H_2O contents (pressure range of 200-400 MPa), we applied a constant correction factor of 1.23 to all EMP analyses of experimental glasses, as well as the H_2O-richest melt inclusions (6-8 wt % H_2O).

Water content

The water contents of three experimental liquidus and sub-liquidus glasses (800CHO3, 800CHO2, and 900CHO2) were determined by Karl-Fischer titration, following the procedure described in Behrens (1995) and using pyrophyllite crystals bearing 5.3 wt % H_2O as standards. These three glasses were used as H_2O-standard glasses for H_2O content determination following the EMP "by-difference" method (Devine *et al.*, 1995) in the other experimental crystal-bearing glasses and the natural glasses. H_2O contents determined by EMP “by-difference” method are given with an uncertainty of $\pm$0.5 wt %.

Phase proportions

The area proportions of phenocrysts and matrix (bubble-free residual glass plus microlites) in the natural samples was determined by point counting on thin sections (653 to 1300 points per sample), and converted into wt % using the following phase densities: 2.7 for feldspars (oligoclase or orthoclase), 5.2 for magnetite, 3.0 for biotite, 3.3 for clinopyroxene (augite), 3.1 for amphibole (pargasite), and 2.4 for the glass (Knoche *et al.*, 1995).

Since the experimental products were too small to determine phase proportion by point counting, the relative proportions of glass and crystals (without discrimination between the mineral phases) were determined by image analysis. The relative proportions of the different mineral phases were determined by mass balance using the program of Stormer (1978), but the results are (i) scarce because many crystals are too small to be accurately analysed and (ii)

calculation residuals are often too high in Na_2O, despite the Na corrections applied on the EMP glass analyses.

PETROLOGY OF THE TRACHYTES FROM CHAINE DES PUYS

Phase assemblage and chemical composition

Bulk-rock compositions

The six samples are metaluminous to slightly-alkaline trachytes, with bulk SiO_2 contents from 62.6 to 69.0 wt %, alkali (Na_2O+K_2O) contents from 10.5 to 12.1 wt %, and a peralkalinity index from 0.89 to 1.08 (Table 2). The CIPW norms suggest silica-oversaturated rocks (presence of normative quartz), rich in feldspars and pyroxenes (Table 2). These compositions are in good agreement with the previous bulk-rock analyses of these trachytes (Camus, 1975; Pupin, 1976, Maury *et al.*, 1980; Foury, 1983; Arnaud, 1989; Guittet, 1996), although our alkali contents are slightly higher in average (Figure 2), due to the Na_2O corrections we made on the EMP glass analyses, while the previous authors provided raw EMP data (our data show similar Na_2O contents without alkali corrections). With bulk SiO_2 increasing from 62 to 69 wt % (CLI to CHO), K_2O increases from 4.1 to 5.3 wt %, CaO decreases from 3.2 to 0.9 wt %, FeO decreases from 4.0 to 1.6 wt %, MgO decreases from 1.0 to 0.2 wt %, while Na_2O remains constant at 6.6-7.3 wt %. With the increase of bulk SiO_2, the content in P_2O_5 decreases from 0.29 wt % (CLI) to 0.03 wt % (CHO). All samples have F contents between 0.1 and 0.2 wt %, Cl contents < 0.5 wt %, and SO_3 ~0.1 wt %.

Phenocryst assemblage and proportions

The main phenocryst assemblage was taken as crystals free of reaction rims and systematically varies with the SiO_2 bulk-content of the trachyte (Table 2). All samples have two mineral groups in common: Fe-Ti oxides and plagioclase (Pl). Fe-Ti Oxides are titanomagnetite (Mt) and ilmenite (Ilm). DOM and CHO also show alkali feldspars (Afs) up to sanidine compositions, CHO having a continuous trend from Pl to Afs. All samples contain biotite (Bt), except CLI. Amphibole (Am) is present in CLI, VAS, and KIL. CHO shows clinopyroxene (Cpx). Note that DOM is here Cpx-free, as seen in the main facies of Puy de Dôme, whereas other minor facies contain a green Cpx (Miallier *et al.*, 2010). Some Cpx have been detected in KIL and CLI samples, but their rarity and compositions similar

to those of the basalts (see below) suggest an inherited nature. As accessory phases, all trachytes contain apatite (Ap) and zircon (Zr). CHO additionally contains titanite (Tit). The phenocryst assemblages in CHO_Pumice and KIL_pumice are identical to their respective dome-related trachytes.

The major phenocrysts represent modal proportions from 7 to 24 % (mass proportions from 10 to 27 wt %; Table 2). For all samples, Fe-Ti oxides do not exceed 1-3 % and feldspars range from 7 to 17 %. In another CHO sample, Foury (1983) reported 8 and 10 wt % of Pl and Afs, respectively. Bt varies between 1 and 5 %. Am represents about 2-4 % and Cpx in CHO is ~1 %. Accessory minerals (Ap, Zr, and Tit) are < 1 wt %.

On a textural point of view, the feldspars sometimes show cloudy cores (full of devitrified glass inclusions) and strong optical zonings that are more reflecting growth rims than true chemical zonings (Figure 3c). In CHO, Afs is dominant on Pl and commonly rims Pl, whereas the opposite in DOM samples. The ferromagnesian phases (Am, Bt, Cpx) can be strongly oxidized, especially Bt in SAR samples (Figure 3e). Although the phenocrysts are mostly free of reaction rims (e.g. Figure 3a,d), all samples also contain small amounts of destabilized phenocrysts (Figure 3b) or small mafic enclaves (more abundant in CLI). Mafic xenocrysts appear in such small proportions that they likely not affect significantly the trachytic equilibrium. Groundmasses in all samples, but pumice from CHO and KIL, are fully microcrystallised with mainly feldspars, showing typical trachytic textures (oriented elongated microlites; e.g. Figure 3a,b,d). CHO_Pumice and KIL_pumice have a glassy (microlite-free) matrix.

Compositions of the natural phenocrysts and glasses

Selected compositions of the natural phenocrysts and glasses are reported in Table 3.

With SiO_2 bulk content increasing from 62 to 69 wt % (CLI to CHO), Pl evolves from andesine (30-42 mol % of anorthite, An_{30-42}) to oligoclase (An_{11-27}) and progressively enriches in K_2O towards anorthoclase (10-20 mol % of orthose, Or_{10-20}) and sanidine compositions (> Or_{35}). For convenience, we will hereafter associate anorthoclase to the Pl group, since they form a continuum compositional trend, in contrast to the sanidine group that will be referred as to Afs. Afs in DOM and CHO are ~An_3-Or_{50} (Figure 4). Most of Pl show limited chemical zoning, with a maximum variation of ~15 mol % An, i.e. An_{42} to An_{28} and An_{28} to An_{12} from core to rim in CLI and CHO, respectively.

Fe-Ti oxides are solid solutions of magnetite-ulvospinel and more rarely, of ilmenite-hematite. Most of the Mt contain 80-90 mol % magnetite (Mt_{80-90}, using the projection

scheme of Andersen *et al.*, 1993), but the whole compositional range for a given sample is Mt_{74-92} (Figure 5), with 74 to 84 wt % FeO, 2 to 8 wt % TiO_2, and 2 to 5 wt % MnO. Ilm composition varies from Ilm_{70-90}, with 45 to 48 wt % FeO and 37 to 44 wt % TiO_2.

Clinopyroxenes in CHO are a Ca-rich augites (Figure 6), with 1-2 wt % Al_2O_3, 10-11 wt % MgO, and TiO_2 < 0.5 wt %, being compositionally similar to that reported for DOM trachytes (Maury *et al.*, 1980). In contrast to CHO, CLI shows Cpx richer in Al_2O_3 (5 to 10 wt %), TiO_2 (1-2 wt %), and MgO (12-15 wt %), being compositionally similar to those reported for the CDP basalts (Maury *et al.*, 1980). Therefore, Cpx in CLI is likely inherited from mafic magmas and will not be considered as belonging to the CLI trachyte assemblage. Similarly in KIL, the two Cpx identified show compositions intermediate between those in CHO and CLI (2-5 wt % Al_2O_3, ~0.7 wt % TiO_2, and 12-15 wt % MgO), and will not be considered as stable phases in the KIL trachyte.

Biotites contain 5-6 wt % TiO_2, 14-15 wt % Al_2O_3, and 12-13 wt % MgO, with those in CHO being slightly enriched in FeO with respect to the other samples (Figure 7), that is, having Mg* [Mg/(Fe+Mg)] ~0.50 against ~0.54-0.57.

Amphiboles in KIL, VAS, and CLI are titanian-hastingsite to titanian-pargasite after the nomenclature of leake *et al.* (1997), with ~11 wt % Al_2O_3 (Al^{IV} ~1.7-1.9 pfu; Figure 8a), ~11 wt % CaO, 3-4 wt % TiO_2, and Mg* ~0.55. In CLI, a second population of Am, kaersutites (Al^{IV} ~2.0-2.2 pfu; Figures 3f and 8b), coexist with the hastingsite/pargasite. One kaersutite has also been analysed in VAS. These kaersutites are similar in composition to the amphiboles analysed in the CDP basalts (Maury *et al.*, 1980), suggesting their inherited nature in CLI.

The glasses in the lava-dome related samples, either as melt inclusions or matrix glasses, were too crystallised for analyses. Therefore, glasses have been analysed in KIL_Pumice and CHO_Pumice, the pumice from explosive events (Table 3). In CHO_Pumice, the glasses are rhyolites, with SiO_2 ranging from 70 to 73 wt %, with the matrix glasses compositionally more evolved than the glass inclusions (SiO_2 ~70 against 72 wt % in average, respectively; Figure 9a). In KIL_Pumice, glasses in both, matrix and inclusions (hosted in Pl, Am, Mt, and Bt), are rhyodacites, with SiO_2 ranging from 65 to 70 wt %, 15 to 17.5 wt % Al_2O_3, 0.6 to 18 wt % CaO, ~2-3 wt % FeO, and 6 to 7.5 wt % Na_2O (Figure 9b).

Volatile content of the glasses

The volatiles dissolved in glasses are assumed to be mainly H_2O, with minor contents of F, Cl, and S (< 0.5 wt %; Table 4).

In CHO_Pumice, the glass inclusions trapped in Cpx, Tit or Zr contain up to $7.9_{\pm 0.5}$ wt % H_2O (Table 4; Figure 3g). In contrast, glass inclusions in Bt and Afs phenocrysts are H_2O poorer ($\leq$ 4 wt %), which may be explained by volatile loss through the cleavage planes typical for these crystals. Matrix glasses show maximum H_2O contents of 1-2 wt %. The melt inclusions have relatively high concentrations in chlorine, i.e. $3400_{\pm 1400}$ ppm, that decrease to ~1700 ppm in the matrix glasses. Sulphur concentrations are of $300_{\pm 300}$ in the glass inclusions. Only one residual glass has been analysed for S, showing ~900 ppm, so that the comparison with melt inclusions may not be reliable. Fluorine contents in melt inclusions or residual glasses are around the limit of detection of our analytical technique, i.e. ~700 ppm.

In KIL_Pumice, the glass inclusions trapped in phenocrysts of Pl and Am (Figure 3h) have H_2O contents up to $7.8_{\pm 0.5}$ wt % (Table 4; the shrinkage air-bubble in one of these inclusions gives confidence in its volatile-tight nature). The maximum H_2O contents analysed in the matrix glasses is again 1-2 wt %. Cl, S, and F have not been analysed in KIL_Pumice.

Results and limitations of the estimations of the trachyte storage conditions

Temperature and f_{O2}

The presence of coexisting Mt and Ilm as phenocrysts in most trachyte samples may constrain the *T*-f_{O2} crystallisation conditions. Before using the Mt-Ilm oxythermometer of Ghiorso & Sack (1991), which has not been formulated originally for trachytic compositions, we tested it for one of our experimental charges (800DOM2) that crystallised Mt and Ilm at 800°C, 200 MPa, and reducing conditions (~ΔNNO -1). The formulation gives a *T* of $834_{\pm 38}$°C and ΔNNO-1.3 at 200 MPa (Table 5), thus validating its use for trachytes. Couples of spatially close Mt and Ilm that passed the test of chemical equilibrium (Bacon & Hirschman, 1988) were thus used to retrieve *T*-f_{O2} values after Ghiorso & Sack (1991). The results show a negative correlation between *T* and bulk SiO_2 content of the host rock, with *T* increasing from ~772°C in DOM to 874°C in SAR and ~955°C in VAS, for ΔNNO varying from +0.4 to +1.7 (Table 5). For CLI sample, the Mt-Ilm geothermometer suggests an unrealistically low *T* of 635°C, which likely reflects Mt-Ilm re-equilibration processes during magma cooling. Indeed,

it has been experimentally shown that 5-µm sized Fe-Ti oxides could re-equilibrate within 4-5 days (Venezky & Rutherford, 1999; Martel & Schmidt, 2003; Devine *et al.*, 2003).

Temperature may also be estimated from Am-Pl equilibrium. Testing the geothermometer of Holland & Blundy (1994) on an experimental charge (800CLI2) that crystallised both phases at 800°C and 200 MPa, yields a *T* of 790°C at 200 MPa (Table 6), so that the formulation can be used with confidence for trachytic compositions. Assuming a *P* of 200-300 MPa, the natural minerals suggest crystallisation temperatures of 821-824°C for VAS and 815-840°C for CLI (Table 6), which are significantly lower *T* than those obtained from the Mt-Ilm oxythermometer (955°C for VAS).

T and f_{O2} may be retrieved from Am composition using the formulations of Ridolfi & Renzulli (2012). This model is based on Am composition recalculated on the basis of 13 cations and has been calibrated for basaltic to dacitic compositions. Tested against our Am-bearing run products, the calculated *T* agree within error (25°C) with run *T*, except for two runs in which the calculated *T* is about 120°C away from run *T* (Table 7). Applied to the CDP, this thermometer calculates *T* from 780 to 940°C. Similarly, using the formulation of Ridolfi & Renzulli (2012) to calculate f_{O2} from Am composition suggests conditions from ΔNNO -0.5 to +3.4 for the natural trachytes (Table 7).

Pressure

Pressure may be estimated from Am composition. Since the existing Am-barometers have not been calibrated on trachytic compositions (at best on quartz latite; Johnson and Rutherford, 1989, or calc-alkaline tonalite; Schmidt, 1992), we first tested our run products with the formulation of Anderson & Smith (1995). This model is valid in the 620-820°C *T* range for *P* from 100 to 1000 MPa, and for a phase assemblage consisting in Am + Qz + Pl (An_{25-35}) + Afs (sanidine) + Bt + Mt (+ melt + fluid). Only two of our experiments fulfil the required paragenesis, with the exception of Afs (thus calculating maximum *P*): CLI sample at 800°C-200 MPa (800CLI2) and 800°C-300 MPa (800CLI3). For both runs, the formulation calculates a *P* of $300_{\pm 60}$ MPa at 800°C, which agrees with the run performed at 300 MPa (Table 7). The run performed at 200 MPa shows a dominance of Ilm over Mt, which reflects reducing conditions that constitutes a source of Al_{tot} enrichment in Am, and possibly results in *P* overestimation (Anderson & Smith, 1995). Regardless, we used the formulation of Anderson & Smith (1995) to estimate crystallisation *P* in the CDP trachytes. This geobarometer is highly sensitive to *T* (up to 200 MPa per 100°C), so that in absence of conclusive *T* estimation for the natural trachytes, we calculated *P* at 800 and 850°C (Table 7).

In the natural trachytes, Am have mean Al_{tot} from 1.98 in KIL to 2.37 in CLI, giving *P* from 391 to 547 MPa at 800°C and from 236 to 380 MPa at 850°C. However, as suggested above, some of these Am belong to a different (basaltic) phase assemblage, which may lead to higher *P* than expected for the trachytic reservoirs.

The formulation of Ridolfi & Renzulli (2012) that gives *P* from Am composition has the advantage of being calibrated for alkaline magmas and does not require a given phase assemblage. Tested against our run products, the formulation suggests correct *P* for the runs at 400 and 300 MPa, whereas *P* is overestimated by 150 MPa at 200 MPa (Table 7). Applied to the natural Am, the calculated *P* range from 288 to 380 MPa for the Am with Al_{tot} from 1.98 to 2.20, and a *P* of 469 MPa for the CLI Am that contains 2.37 Al_{tot} (Table 7).

Pre-eruptive volatile content

The pre-eruptive volatile content may be retrieved from the volatiles dissolved in the glass inclusions assuming they were trapped in the magma chamber and remained volatile-tight after entrapment. The highest H_2O concentrations in CHO and KIL glass inclusions are ~8.0 wt %, which corresponds to a minimum value in case of leakage after entrapment. Since Cl, S, and F concentrations in the glass inclusions are < 0.5 wt % (Table 4), we consider H_2O as the main dissolved volatile species. H_2O solubility models place constraints on minimum pre-eruptive pressures. The H_2O solubility model of Di Matteo *et al.* (2004; calibrated for trachytic compositions) predicts a *P* of ~250 MPa at ~850°C for a melt H_2O content of 8.0 wt %. Our own H_2O solubility data acquired on CHO composition give 6.9 and 8.5 wt % dissolved H_2O at 200 and 300 MPa, respectively (Table 4).

Further insight on the magma water concentration may be obtained from the Bt-Afs-Mt equilibrium (Czamanske & Wones, 1973), three phases that are present as phenocrysts in CHO_Pumice (Table 3). For Afs, the activity-composition model of Waldbaum & Thompson (1969) yields an activity for the $KAlSi_3O_8$ component of 0.6 (Fabbrizio *et al.*, 2006). For Mt, structural formulae calculations and activity-composition relations as in Fabbrizio *et al.* (2006) have been adopted, yielding activities for the Fe_3O_4 component around 0.9. Fe^{3+} in Bt was calculated as equal to $Al^{IV} - 2 + (Na + K - 2)$ (Deer *et al.*, 1992), corresponding to a proportion of Fe as Fe^{3+} around 10-15 % in CHO_Pumice Bt. The activity-composition model of Czamanske & Wones (1973), also used by Fabbrizio *et al.* (2006), was adopted in this study for Bt. Results (Table 8) sensitively depend on *T* and f_{O2}, but f_{H2O} corresponding to near H_2O-saturation are obtained for 750°C and ΔNNO +0.7, i.e. for the *T*-f_{O2} determined from Mt-

Ilm oxythermometry for CHO_Pumice (Table 5). This suggests that the phenocrysts crystallised under H_2O-rich conditions in the CHO magma.

Pre-eruptive conditions

In summary, the pre-eruptive conditions determined from the petrological study of the natural trachytes are (i) *T* of ~780-850°C for CLI, ~806-955°C for VAS, ~775°C for DOM, depending on the geothermometer used, (ii) f_{O2} between -0.5 to +3.4, (iii) *P* from 200 to 400 MPa, and (iv) melt H_2O contents up to 8.0 wt %. Besides potential differences in storage conditions specific to each studied trachytic centre, the variation in the estimated pre-eruptive conditions may arise from (i) mineral re-equilibrations upon magma ascent or emplacement as dome, (ii) use of inappropriate phase assemblage (crystal inheritance from mafic magmas), and (iv) application of models outside compositional calibration range.

PHASE EQUILIBRIA

Phase relations

In order to better constrain the pre-eruptive *P*-*T*-f_{O2}-H_2O conditions deduced from the CDP trachytes, phase equilibria were determined for *P* ranging from 200 to 400 MPa, *T* between 700 and 900°C, ΔNNO from -1 to +1, and H_2O-saturation conditions (Table 9). Such data also bring information on the phase relationships of variously fractionated trachytic liquids in a given *P*-*T* space.

Effect of bulk-rock composition

The phase relationships show a general consistency in crystal appearance with melt evolution (Table 9). At 800°C and 200 MPa, liquidus conditions are obtained for 69.0 wt % SiO_2 (CHO), then Fe-Ti oxides and Bt appear in melts with 66.7 wt % SiO_2 (DOM), followed by Cpx for 65.0 wt % SiO_2 (KIL, VAS), while Pl + Am replace Cpx in melts with SiO_2 < 62.6 wt % (CLI). Although the order of phase appearance is consistent for most of the *P*-*T* conditions investigated, some cases show more complicated relations. For instance, Cpx is present in CHO between 700-750°C and 200-350 MPa (runs #4, 5, 10 and 11), disappears in DOM, and is present again in melts with lower SiO_2 contents, which we attribute to differences in bulk chemistry. In particular, the bulk composition of DOM is slightly depleted in alkali

components compared to the other trachytes with SiO_2 > 64 wt % (Figure 2), which may explain the absence of Cpx. As noted in other experimental studies (Dall'Agnol *et al.*, 1999), some Am can display Cpx cores, which possibly reflects growth of the Cpx during the early stages of the run (heating up period) when H_2O has not yet diffused homogeneously across the melt. This, together with the overall small size of crystals, makes difficult the straightforward distinction between Am and Cpx in some charges (KIL in particular). As a result, whenever positive identification was lacking, the corresponding phase boundary was inferred on the basis of phase relationships observed in other trachytes.

Effect of pressure and temperature

The phase relations between 700-900°C and 200-400 MPa of each trachytic composition are shown in Figure 10. For all compositions, Fe-Ti oxides are the liquidus phase, crystallizing at T > 900°C and at 800-850°C in CHO. Fe-Ti oxides are mostly Mt under moderately oxidized conditions (ΔNNO ~0 to +1), together with Ilm in the reduced experiment (~ΔNNO -1).

In CHO (69.0 wt % SiO_2; Figure 10a), Mt crystallisation is shortly followed by Cpx appearance. Bt crystallisation only concerns the low-T and high-P space (below 725°C-300 MPa and 800°C-400 MPa). Afs rimmed by Pl appear at T < 750°C, in volume proportion roughly equal. Minor phases have been detected, such as Zr at 900°C and 200 MPa (liquidus conditions for the other phases) and Tit in two charges at $P \leq 300$ MPa.

In DOM (66.7 wt % SiO_2; Figure 10b), Fe-Ti oxide crystallisation is followed by Bt at T ~850°C. Pl and Afs coexist below 800°C. In contrary to CHO, Pl is rimmed by Afs and is volumetrically dominant on Afs. Cpx is absent in the investigated P-T range. Zr has been detected in nearly all charges.

SAR (65.5 wt % SiO_2; Figure 10c) shows Mt, Bt, Pl, and Afs phase appearance very close to DOM, and additionally crystallises Cpx at T < 800°C. It was not possible to discriminate the saturation curves of Cpx from Pl+Afs. Zr and Tit are present in most charges.

KIL (65.1 wt % SiO_2; Figure 10d) shows similar Mt, Bt, Pl and Afs phase relationships than for DOM and SAR (with a volumetrically-dominant Pl rimmed by Afs). In KIL, Cpx crystallises at higher T than in SAR, i.e. between 825 and 900°C (potentially close to Bt). For T < 800°C and P of 300-400 MPa, the composition of the ferromagnesian phase is intermediate between Am and Cpx, suggesting Am crystallisation at low T and high P and intergrowths between both phases. Zr and Tit have been observed as minor phases in some charges.

VAS sample (65.0 wt %; Figure 10e), which has a SiO_2 content similar to KIL, displays similar phase boundaries for feldspars (with Afs finely rimming Pl), Mt, and Bt. The Cpx/Am phase relations seems different than in KIL, but significant intergrowths and the very small size of these crystals likely distort the exact Cpx/Am topological relationships. Am appears between 825 and 900°C in VAS and is replaced with Cpx at *T* between 750 and 800°C, while in KIL, Cpx appears first (between 825 and 900°C) being replaced with Am at lower *T*. Therefore, Am stability is favoured in VAS at the expense of Cpx, whereas the opposite in KIL. This can be attributed to differences in minor element contents such as F that would favour Am crystallisation in VAS. Zr and Tit are present in most charges.

CLI (62.6 wt %; Figure 10f) shows phase relations very distinct from the other trachytes. Mt and Am are the liquidus phases at $T > 900$°C. Am destabilizes into Cpx below a *P-T* domain defined by 750°C-400 MPa and 800°C-200 MPa. Co-precipitation of Pl and Bt occurs in a restricted *T* range of 800-825°C. Afs is only stable at *T* below ~750°C. The determination of the mineral phases in the charges at $T \leq 750$°C was particularly difficult due to high fractions and small sizes of the crystals.

Phase compositions

The compositions of the experimental Fe-Ti oxides are reported in Table 10. Fe-Ti oxides are liquidus or near-liquidus phases. Mt seem to be little dependent on the bulk-rock composition of the starting melt (Figure 5). In contrast, Fe-Ti oxides are strongly f_{O2} dependent, with crystallisation of $Mt_{88\text{-}98}$ with 2-5 wt % of TiO_2 in the experiments performed at $\Delta NNO > 0$, $Mt_{68\text{-}74}$ with 10-11 wt % of TiO_2 for ~ΔNNO -0.5, and Mt_{53} with TiO_2 up to 15 wt % where coexisting with $Ilm_{91\text{-}93}$ at ~ΔNNO -1.3.

The compositions of the experimental Bt are reported in Table 11. Bt shows Al contents between 30 and 40 mol %, Mg contents between 20 and 45 mol %, and Fe+Mn ranging from 20 to 45 mol % (Figure 7a). In DOM, SAR, KIL, and VAS, Bt is the sub-liquidus phase (crystallizing after Mt), whereas it appears later (at lower *T*) in the crystallizing sequence of CHO and CLI (Figure 10). However, the similarity in Bt composition in the different trachytes for given *P-T-*f_{O2} conditions suggests little compositional control (Figure 7a). All other parameters being equal, Bt composition is also little affected by *P* (slight increase of ~5-10 Mg mol % with *P* decreasing from 400 to 200 MPa at 750°C). In contrast, *T*

and f_{O2} have both strong effects on Bt composition, with Fe+Mn increasing from 22 to 45 mol % for a *T* increase from 700 to 825°C at ~ΔNNO +0.5 and from 22 to 35 mol % with f_{O2} decreasing over ~1.5 log units at 800°C. The combined variations of Mt and Bt compositions were used as an oxythermometer (Figure 7b).

The experimental Cpx are augites to salites, with 40-50 Wo mol % and 15 to 35 En mol % (Table 12; Figure 6). The experimental Cpx tend to grow poorer in Wo component with the starting melt enriching in bulk-SiO_2 content (-5 mol % Wo from CLI to CHO). In the most differentiated melts (CHO, SAR, and KIL), Cpx have similar compositions within error for given *P*-*T*-f_{O2} conditions, whereas they are slightly enriched in En content (~5 mol %) in VAS and CLI.

Am are only present in the two less evolved compositions, i.e. VAS and CLI. They are titanian-hastingsites to titanian-pargasites after Leake *et al.* (1997), containing 11-12 wt % Al_2O_3, ~2.5 wt % Na_2O, and ~3 wt % TiO_2 (Table 13). Am is very sensitive to *P*, *T*, f_{O2}, and melt composition (Figure 8). For instance, using CLI composition, all other parameters being equal, increasing *P* from 200 to 400 MPa at 800-825°C, increases the cation number in A-site from ~0.82 to 1.02 pfu and Al^{IV} from 1.78 to 1.94 pfu (Figure 8a). Increasing *T* from 800 to 900°C at 200 MPa increases the cation number in A-site from 0.82 to 0.90 pfu while Al^{IV} decreases slightly. The effect of the starting melt composition is highlighted by the runs performed either at 800°C-300 MPa or 825°C-400 MPa, in which Al^{IV} slightly decreases and the cation number in A-site slightly increases with increasing bulk-SiO_2 content of the starting melts (from CLI to VAS). The Mg* of Am reflects redox conditions (Figure 8b), with Mg* ~0.45 characterizing runs performed at ~ΔNNO -0.5, Mg* ~0.6 for ~ΔNNO +0.5, and Mg* ~0.7 for ~ΔNNO +1 (the redox conditions are deduced from the Fe-Ti oxide compositions; Figure 5).

The experimental feldspar compositions are reported in Table 14. Both Pl and Afs crystallised in all samples, except in CLI where only Pl is present. With increasing degree of fractionation of the bulk rock, the feldspars get slightly enriched in alkali component (i.e. shifting towards the Ab and Or components from CLI to CHO; Figure 4). Pl composition is known to be particularly sensitive to both *T* and melt H_2O content, as observed in our experiments. All other parameters being equal, An-in-Pl increases in CLI from An_{19} to An_{35} when *T* increases from 750 to 800°C at 300 MPa or from An_{26} to An_{42} for the same *T* increase at 200 MPa. The influence of melt H_2O content is here directly related to *P* (H_2O-saturated

conditions) and has little effect on Pl composition (Pl compositions at 200, 300 and 400 MPa often plotting very closely).

The experimental residual glasses are trachytes to rhyolites, with SiO_2 ranging from 65.2 to 75.8 wt %, CaO from 2.8 to 0.5 wt % (Figure 9), and alkali content from 11.0 to 7.9 wt % (Table 15). The residual glass compositions directly rely on the *P*-*T* crystallisation conditions, and thus, on the proportion and nature of the crystallised phases. Plotting rock-glass tie-lines as a function of *P*-*T* for a given bulk-rock composition shows that decreasing *T* leads to more differentiated residual melts (enriched in normative Qz in comparison to Ab, whereas constant in Or; Figure 11) and to a decreasing peralkalinity index (e.g., from 0.88 to 0.70 with *T* decreasing from 900 to 775°C; Table 15). The less-evolved trachyte (CLI) seems to show residual melts enriched in normative Or with decreasing *P* (Figure 11). For given *P*-*T* conditions, increasing SiO_2 content of the starting melt (from CLI to CHO) leads to residual melts that show (i) a decrease in SiO_2 and CaO (Figure 9), (ii) quasi-constant FeO contents (Figure 9), and (iii) a decrease in peralkalinity (Table 15).

TRACHYTE STORAGE CONDITIONS AT CHAINE DES PUYS

We compare hereafter the paragenesis, phase proportions and compositions of each of the six sampled trachytes with their respective experimental phase equilibria, in order to propose pre-eruptive *P*-*T*-f_{O2}-melt H_2O conditions for the CDP trachytes and a petrogenetic model for the magma reservoirs.

Puy Chopine (CHO; 69.0 wt % SiO_2)

The natural phase assemblage of CHO consists of Fe-Ti oxides + Cpx + Bt + Afs + Pl, which is experimentally reproduced for $T < 725$°C and *P* between 250 and 400 MPa (Figure 10a). Only one experiment (700°C and 300 MPa) falls within the natural paragenesis field, but the Mt, Pl, and Bt crystals were too small to be accurately analysed, so that we lack both phase compositions and mass balance calculations. However, the total crystal proportion of 41 % determined by image analysis in this charge (Table 9) is too high compared to the natural crystallinity of 21-24 % (Table 2). Crystallinity can be lowered by either getting closer to the phase liquidus (increasing *T*) or by increasing *P* (as illustrated for DOM at 750°C in Figure 10b). It follows that the 21-24 % of phenocrysts analysed in the natural CHO sample can be

produced by crystallisation at ~700°C and ~350 MPa. The natural CPx compositions are not well-reproduced experimentally in terms of their Fe-Mg ratio (En_{30-40} against En_{15-30}), except for the most oxidized experiment at ~ΔNNO +1.1 (run at 750°C and 300 MPa; Figure 6). This suggests pre-eruptive conditions slightly more oxidized than those inferred from the Fe-Ti oxides (0 < ΔNNO < +0.5; Figure 5). The natural feldspars cover a continuum trend from Pl to Afs, which turns out to be of little help for constraining *P*-*T* conditions. The compositions of the natural Bt and Mt are compatible with crystallisation at $T \leq 750$°C, especially if Mt compositions underestimate f_{O2} (Figure 7b). The melt inclusions trapped in Cpx, Tit, or Zr phenocrysts suggest H_2O contents ~8 wt % (Figure 9), corresponding to a saturation pressure of ~300 MPa (Table 4). Therefore, we suggest pre-eruptive conditions for CHO close to $720_{\pm 20}$°C, 300-350 MPa, ~8 wt % H_2O, and ΔNNO +1.

Puy de Dôme (DOM; 66.7 wt % SiO_2)

The DOM sample contains Fe-Ti oxides + Bt + Pl + Afs, a paragenesis experimentally reproduced for $T < 775$°C (Figure 10b). The natural Bt and Mt compositions in DOM are compatible with crystallisation at *T* between 750 and 800°C at ~ΔNNO +0.5 (Figure 7b). Yet, the experimental phase assemblages at *T* ~750°C poorly constrain *P* that requires phase proportions and compositions to be determined. The natural Pl and Afs compositions are reproduced at 750°C for *P* between 200 to 400 MPa (Figure 4), so that feldspars do not help much constraining *P*. Yet, the crystallinity of 20-23 % measured in the natural products is reproduced at 750°C between 325 and 350 MPa (Figure 10b). In detail, the individual phase proportions (14-15 wt % of Pl+Afs, 5-6 wt % of Bt, 77-80 wt % of Gl; Table 2) are reproduced in the experiments at 750°C and 350 MPa (15 wt % of Pl + Afs, 4 wt % of Bt, 79 wt % of Gl; Table 9). Therefore, we propose pre-eruptive conditions of $750_{\pm 20}$°C, 350 MPa, ΔNNO +0.5, and H_2O contents close to saturation conditions.

Grand Sarcouy (SAR; 65.5 wt % SiO_2)

SAR naturally contains Fe-Ti oxides + Bt + Pl. This assemblage lacking a ferromagnesian phase such as Am or Cpx (in addition to Bt) and the low phase proportions of 10 % constitute

a specificity in comparison to the other trachytes. Although our experimental results do not allow separation between the saturation curves of Pl and Afs, there could be a restricted *P*-*T* domain between 775 and 800°C and between 200 and 400 MPa of Pl + Mt + Bt coexistence without Afs (Figure 10c). The natural Bt and Mt suggest a f_{O2} close to ΔNNO < +0.5 and crystallisation *T* between 750 and 800°C (Figure 7b). The natural Pl are depleted in Or component with respect to the experimental ones (Figure 4), and the Pl-Afs co-precipitation in the experiments may reflect a starting material slightly too rich in K, possibly resulting from some Na loss during fusion of the starting SAR dome sample. The very low crystallinity of the natural SAR sample (5 wt %) would be compatible with crystallisation at high *P* (300-400 MPa), as suggested by the experimental products at 750°C, in which crystallinity decreases with increasing *P*. Therefore, we propose pre-eruptive conditions around $775_{\pm 20}$°C, 200-400 MPa, ΔNNO +0.5, and H_2O contents close to saturation conditions.

Cratère Kilian (KIL; 65.1 wt % SiO_2)

The KIL sample contains Fe-Ti oxides + Pl + Bt + Am. In the experiments, Cpx crystallises at *T* < 850°C. In the low *T* and high *P* domain of the KIL phase diagram (*T* < 800°C and *P* of 300-400 MPa; Figure 10d), some weird but reproducible analyses of a ferromagnesian phase likely suggest intimate mixing between Cpx and Am (analyses marked with * in Table 12). Assuming Am replaces Cpx at *T* < 800°C and *P* of 300-400 MPa, and considering a *T* domain between 750 and 800°C (*P* = 200-400 MPa) where Pl exists without Afs, there may be a *P*-*T* domain at 300-400 MPa and 750-800°C, for which the experiments reproduce the natural paragenesis (Figure 10d). The compositions of natural Bt and Mt are compatible with crystallisation *T* between 750 and 800°C and ΔNNO +0.5 (Figure 7b), whereas the Pl compositions are closely approached (Figure 4). The slight misfit between the compositions of the experimental glasses and that of melt inclusions trapped in Am, Pl, and Bt phenocrysts (especially in FeO content; Figure 9) may result from difference in f_{O2}. Nevertheless, the highest H_2O contents measured in the glass inclusions, i.e. ~8 wt % (Figure 9), compare well to those found in the CHO sample (Table 4). We thus propose pre-eruptive conditions close to $775_{\pm 20}$°C, 300-400 MPa, ΔNNO +0.5, and 8 wt % H_2O in the melt.

Puy Vasset (VAS; 65.0 wt % SiO_2)

The VAS sample contains Fe-Ti oxides + Pl + Bt + Am, a phase assemblage experimentally reproduced for *T* between 775 and 800°C and *P* between 300 to 400 MPa, assuming an experimental domain where Pl exists without Afs (Figure 10e). The compositions of the natural Mt and Bt are compatible with crystallisation *T* ~800°C and 0 < ΔNNO < +0.5 (Figure 7b). The natural Am compositions have been experimentally reproduced at 800°C and 300 MPa. From the compositional evolutions of the experimental Am with *P*-*T*, we can infer that the natural compositions would be also reproduced for *P* ranging from 250 to 350 MPa and *T* from 700 to 900°C (Figure 8a). The Mg* of the natural Am suggests -0.5 < ΔNNO < +0.5 (Figure 8b). The natural Pl compositions are experimentally reproduced in the *T* range 750-775°C and *P* from 200 to 400 MPa (Figure 4). Assuming glass inclusion compositions similar to those in KIL (due to the similarities in both bulk-rock compositions; Table 2), we suggest similar *T* of 750-825°C, *P* of 300-400 MPa, and 7-8 wt % of dissolved H_2O in the melt. We propose pre-eruptive conditions close to those for KIL, i.e. $775_{\pm 20}$°C, 300-400 MPa, 0 < ΔNNO < +0.5, and H_2O contents close to saturation conditions.

Clierzou (CLI; 62.6 wt % SiO_2)

The CLI sample contain Fe-Ti oxides Pl + Am, a paragenesis that is reproduced for a restricted range of *T* between 800 and 825°C for *P* between 200 and 400 MPa, assuming a *T* field where Pl exists without Bt; Figure 10f). The natural Mt span a relatively large compositional range from Mt_{80} to Mt_{94} (Figure 5) suggesting 0 < ΔNNO < +1. The Mg* of the natural Am in CLI confirms redox conditions close to ΔNNO +0.5 (Figure 8b). Figure 8a shows that the natural Am covers a wide range of composition, with Al^{IV} from ~1.75 to 2.25 and 0.8-0.9 cations in the A site. The experiments also highlight that Am with Al^{IV} > 2.0 cannot crystallise from trachytic melts at $P \leq 400$ MPa. Therefore, some of the Am in CLI are likely inherited from more mafic melts, whereas the others are consistent with crystallisation from a trachytic liquid at *T* ~800°C and *P* of 200-350 MPa. The natural Pl compositions are experimentally reproduced at *T* between 750 and 800°C and *P* of 200-300 MPa (Figure 4). Therefore, we propose pre-eruptive conditions close to 800-825°C, 200-350 MPa, 0 < ΔNNO < +1 and H_2O contents close to saturation conditions.

The trachytic reservoirs: pre-eruptive conditions and petrogenetic relations

The comparison between the natural and experimental phase assemblages, proportions, and compositions for all trachytes points to a pre-eruptive *P* of 300-350 MPa (~10-11 km deep), f_{O2} around 0 < ΔNNO < +1, and melt H_2O contents ~8 wt %. Besides H_2O, $300_{\pm 300}$ ppm S, $670_{\pm 300}$ ppm F, and $3400_{\pm 1400}$ ppm Cl have been analysed in the CHO glass inclusions (EMP; Table 4), showing that the CDP trachytic liquids are not strictly saturated with H_2O, but also contain less than 0.5 wt % of Cl, S, and F. In comparison, 1500-2000 ppm Cl, ~1000 to 2000 ppm S, have been analysed in olivine-hosted basaltic glass inclusions in scoria from CDP Puy Beaunit (Jannot *et al.*, 2005), hinting at a volatile loss between the deep mafic source and the upper trachytic magma chamber(s). Although no dissolved CO_2 in the basaltic melt inclusions has been reported, Jannot *et al.* (2005) documented the occurrence of CO_2-rich fluid inclusions strongly suggesting the presence of CO_2 in the magmas parental to trachytes. Considering that trachytes are produced by ca 80-90 wt% crystallisation of basalt (Maury *et al.*, 1980; Villemant *et al.*, 1980), a strictly incompatible behaviour of Cl would have resulted in Cl contents higher than 1 wt % in the trachytic derivatives, which are much higher than accepted solubility values for such melts at mid crustal pressures (e.g., Signorelli & Carroll, 2002), hence pointing to significant degassing of that element during fractionation. Similarly, the fact that the S content drastically drops from 1000-2000 ppm in the basaltic melt inclusions to ~300 ppm in the trachyte melt inclusions, suggests a strong degassing at the level of magma chamber or deeper. Therefore, performing phase equilibria under H_2O-saturated conditions (a_{H2O} = 1), represents an end-member case that may not fully reproduce real conditions, since some Cl, S, and F were present in the trachytic magmas, and possibly CO_2 at early stages. Both F and S have been shown to affect amphibole stability in arc magmas (e.g., Costa *et al.*, 2004), and future work will have to explore the role of such elements on trachyte phase equilibria.

In contrast to the other parameters, the pre-eruptive *T* vary in a systematic way with bulk SiO_2 content of the trachyte, decreasing from 800-825°C in CLI to ~720°C in CHO (Figure 12). Similarly, the pre-eruptive conditions deduced from the phase equilibria suggest storage at a constant depth ~10-11 km, so that the compositional differences likely represent various stages of magma differentiation with *T*. The experimental results bring further evidence for the hypothesis of magma differentiation, by showing residual melt compositions

for the less differentiated trachytes at *P-T* conditions close to pre-eruptive (e.g. 750KIL3 or 800CLI3 in Table 15) that are very close to the bulk-rock composition of the most differentiated trachytes (e.g. CHO or DOM; Table 2). Yet, there is no correlation between the bulk SiO_2 content of all trachytes (Table 2) and the eruption age (CLI, SAR, DOM, CHO, VAS, KIL in chronological order; Table 1), which at first sight argues against the idea of a magma differentiation with time. In detail, however, the four northernmost edifices define a coherent trend of bulk SiO_2 versus age, which opens the possibility for these vents to be connected to a single common reservoir, which would have been tapped to produce CLI, SAR DOM and CHO magmas whereas VAS and KIL would belong to a distinct, southernmost chamber, albeit located at the same depth.

The depth of ~10-11 km determined experimentally for the trachyte reservoirs fully agrees with the seismic data of Zeyen *et al.* (1997). Indeed, these authors suggested a three-layer crust corresponding to different velocities: an upper crust up to 10-12 km deep, a felsic lower crust up to 18-20 km, and a mafic lower crust up to ~26 km below the CDP where the Moho uplifts and primitive basalts accumulate. Since the second reflector has been interpreted as a change in rheology between the mafic and felsic crust, there is possibly an intermediate level of magma differentiation and storage at 18-20 km deep. Therefore, the basaltic magmas make their way to the surface through a network of connected pull-apart fractures, with or without temporary intermediate storage (Figure 13).

Implications for the CDP plumbing system and future eruptive scenarios

The prevailing view is that each trachytic vent was fed by small, isolated, and ephemeral reservoirs (Boivin *et al.*, 2009). The size of each reservoir can be approximated assuming a spherical shape, and considering the volume of trachytic magma ejected, which is in the range 0.2-0.4 km^3 for each event. Since about 80% of basalt crystallisation is needed to produce these felsic derivatives, it implies a volume of 1-2 km^3 for each reservoir (assuming trachyte production in the mid crust), which translates into a sphere with radius R of 0.6-0.8 km. The conductive cooling time t of a sphere can be calculated using analytical solutions developed by Carslaw & Jaeger (1959). Here for simplicity we use the following standard approximation:

$$t = R^2/\kappa_l$$

where κ_l is the thermal diffusivity ($7.7\ 10^{-7}$ m^2 s^{-1}). For the above radius range, cooling times of 15-25 ky are found. This shows that, albeit small, such reservoirs are likely to be still hot nowadays, if not partially molten. Reactivation of any such reservoir will thus depend on the likelihood that forthcoming basalt batches intercept one of cooling magma bodies. The observed scattered pattern of basalt emission centres along the chain, both in time and space, makes such a hypothesis relatively unlikely.

However, the existence of a coherent *T* versus age trend among the northernmost edifices opens up the possibility of having a single reservoir at depth. In such a view, the area of a putative single reservoir is constrained to a first order approximation by the surface dispersion of the four concerned vents, which is roughly equivalent to 4x8 km^2 (Figure 1). Our data document a continuous *T* decrease from 820°C to 720°C. According to available geochronological constraints (Boivin *et al.*, 2009), such a decrease occurred within 5-6 ky. These data can be confronted with fluid dynamical analyses of the thermal regime of magmatic reservoirs to assess whether they are compatible with the existence of a large magma volume at depth.

We first address the question of the size of the reservoir using the analysis put forward by Koyaguchi & Taneko (2000). These authors have shown that under steady state conditions, i.e. periods during which magma input versus output are broadly balanced, the average size R of a felsic reservoir is governed by the long term heat balance ΔQ (heat loss due to eruption minus heat gain owing to basalt input), according to the following equation which corresponds to the steady solution of heat loss by conduction of a sphere embedded in a solid medium at a temperature T_s:

$$R = \Delta Q / 4\ \pi\ k\ (T_{EFT}-T_s)$$

where T_{EFT} is the effective fusion temperature and k the thermal conductivity (2.4 W m^{-1} K^{-1}). The effective fusion temperature is the temperature at which the magma viscosity becomes too high for thermal convection to occur, which is generally considered to happen when the crystallinity approaches or exceeds 50%. For trachytic compositions at 300-400 MPa, T_{EFT} can be inferred from our data to be around 700°C (solidus in Figure 10). Following Koyaguchi & Kaneko (2000), ΔQ can be approximated by the long term eruption rate when the silicic reservoir was active. Over the time span of 5-6 ky, approximately 2 km^3 of trachytic magma was erupted along the four considered vents. The equation for ΔQ hence writes as:

$$\Delta Q = E\ \rho\ (c\ (T_b-T_{EFT}) + L\ (1-X_{crit}))$$

where E is the long term eruption rate (m^3 s^{-1}), ρ the magma density (2400 kg m^{-3}), c the specific heat (1300 J $kg^{-1}K^{-1}$), T_b the temperature of the input basalt (1200°C), L the latent heat (2.5 10^5 J kg^{-1}) and X_{crit} the critical melt fraction beyond which the magma locks up (0.5). For a time span of 6 ky, ΔQ is found to equal 0.8 10^5 kJ s^{-1}. Considering a far field T_s of 300°C, this in turn yields an average R of about 6 km for the reservoir or a sphere whose diameter would correspond broadly to the north-south extension of the four vents of interest. It needs to be stressed that this estimate is quite sensitive to the long term eruption rate. For instance, if E was 1.5 km^3/6 ky (instead of 2 km^3/6 ky), then R would drop to 2.7 km. In contrast, an increase of the far field temperature to 350°C would increase R to 7.5 km (for E= 2 km^3/6 ky). Considering the error associated to dating (±1 ky) and using a time interval of 4 ky would increase R to 11 km (for 2 km^3). Regardless, our point is to show that the *T* trend recorded between some CDP silicic centres is compatible with the existence of a large reservoir at depth with a lateral extension of several km, possibly exceeding 10 km, at least when the silicic chain was active.

The next question obviously arising is that of the possible present-day existence of such a reservoir, in view of its considerable size and of the relatively recent age of eruptions. To address this question, we first calculate the heat flux F corresponding to the case of a vigorously convecting reservoir. The classical relationship reads as (Turner, 1973):

$$F = \lambda\, k\, (\alpha\, g / \kappa_l\, \nu)^{1/3}\, (T_l - T_{EFT})^{4/3}$$

where λ is a constant (0.1), k is the thermal conductivity (2.4 W m^{-1} k^{-1}), α is the coefficient of thermal expansion of the liquid (5 10^{-5} K^{-1}), g is the gravitational acceleration (9.8 m s^{-2}), κ_l the thermal diffusivity (7.7 10^{-7} m^2 s^{-1}), ν is the kinematic viscosity (4 10^{-2} m^2 s^{-1} calculated for a melt with 8 wt % H_2O which gives a viscosity of ca 100 Pa s; Whittington *et al.*, 2001), T_l the temperature of the magma interior taken as the trachyte liquidus at saturation and 300-400 MPa (~850°C). This yields a convective heat flux F = 4.7 kJ s^{-1} m^2. If the documented cooling Δ*T* of ca 100°C was due to convection then its timescale can be estimated by calculating the heat loss H_{loss} corresponding to such a *T* drop. This is given by the following relationships:

$$H_{loss} = M_{trachyte}\, (\Delta T^{*} c + L(1-X))$$

where $M_{trachyte}$ is the mass of the cooling trachytic magma body (kg), and X the % of crystallisation occurring during cooling, with other parameters as above. The mass of the magma body can be approximated as that of a tabular body with 4x8 km edges, with a conservative thickness of 0.5 km. The extent of crystallisation needed to evolve from the

more mafic toward the more felsic trachyte is approximately 20% (X = 0.2). This gives a H_{loss} of 5 10^{18} J. The time t (s) is now given by the simple relationships:

$$t = H_{loss}/F\ S$$

S being the surface of heat exchange (4x8 km^2). This yields a cooling time of about 1 year. A similar result was obtained by Cottrell *et al.* (1999) for the Santorini Minoan magma that bears evidence of fast *T* change (85°C heating of 30 km^3 of magma in 3 months) prior to eruption. Admittedly, much of the parameter values adopted here, in particular those concerning the dimensions of the reservoir, are loosely constrained but the essential result, already expressed in previous studies (e.g. Huppert & Sparks, 1988a,b), is that the timescale of cooling for a vigorously convecting system is exceedingly short on geological timescales (see also Koyaguchi & Kaneko, 2000). Increasing the mass of magma by a factor of 100, clearly an unrealistic scenario, would increase the timescale by the same factor, which will remain still well below the ky range of thermal relaxation documented by radiometric dating.

That is not to say that any reservoir at depth has completely solidified by now, as already illustrated for the case of isolated reservoirs first discussed. As emphasized by many authors (e.g. Koyaguchi & Kaneko, 2000), conduction timescales are much longer than those by convection, typically on the order of 10^4-10^5 y. In detail, according to Koyaguchi & Kaneko (1999, 2000), most silicic reservoirs follow a two-stage evolution, with a first shortlived one (few years to decades) during which convection is active, followed by a conduction dominated regime lasting several millennia, which sets in as soon as the crystallinity is higher than a characteristic threshold (say 50%). A typical conduction timescale is given by the simple conduction equation:

$$t = D^2/\kappa_l$$

where D is the thickness of the cooling magma layer. A layer of 500 m will cool in about 10 ky which is indeed comparable to the radiometric time span recorded at CDP silicic centres. In other words, any sizeable reservoir (i.e. several km of lateral extension and half km thick) could still be present nowadays in a partially molten state. The amount of silicic magma required by such a hypothesis is on the order of 6-15 km^3 (for a layer 200-500 m thick). Since trachyte production needs ~80% basalt crystallisation (Maury *et al.*, 1980; Villemant *et al.*, 1980), this in turn implies that some 30-75 km^3 of basalt was intruded in the crust. About 8 km^3 of basalt have been extruded during the last 80-90 ky at CDP (Boivin *et al.*, 2009). Considering an intrusive/extrusive ratio of 4-5 (White *et al.*, 2006), this suggests that at least 32-40 km^3 of basalt has entered the system during the last 80 ky, thus falling at the low end of the previous estimate, but in general agreement with it.

The possibility of having a present-day reservoir fed by a silicic mush has implications for the timescale of volcanic unrest at CDP. Clearly, owing to its high crystallinity, any such reservoir is unlikely to erupt on its own. Replenishment of such a magma chamber by fresh and hot basalt may, however, drive the system again beyond the threshold of magma mobility, thereby unlocking it for an eruption. Various studies have modelled such a situation (e.g., Snyder, 2000; Couch *et al.*, 2001; Burgisser & Bergantz, 2011), which is common place in arc settings (e.g. Pallister *et al.*, 1992), and concluded that reactivation of silicic mushes can occur over periods as short as hours to months following basalt injection. The problem is conveniently treated in the context of a thermal boundary layer occurring when two fluids of different temperatures (hence different viscosities) are juxtaposed to each other. Following classical fluid dynamic theory (e.g. Brandeis & Jaupart, 1986; Snyder, 2000), the thickness of the boundary layer δ (m) that develops before convection starts, is calculated as:

$$\delta = (R_c\, \kappa_l\, \mu / g\, \alpha\, \Delta T\, \rho)^{1/3}$$

where R_c is the critical Rayleigh number defining the onset of convection (here taken as $\sim 10^3$), and ΔT the thermal gradient across the boundary layer. Application of the above relationships to heavily crystallised CDP cold trachyte (i.e. with a viscosity of $\sim 10^6$ Pa s and a ΔT of 400°C), yields a boundary layer half a meter thick. The timescale τ_i for layer instability (taken as a proxy to the timescale of eruption triggering following basalt injection; see Snyder, 2000) is now given by:

$$\tau_i = \delta^2\, \rho\, c / k\, \pi$$

Application to CDP context gives a timescale of about 5 days. Use of a viscosity two orders of magnitude higher (10^8 Pa s) will increase τ_i to about 3 months.

The main conclusion that emerges from the above scaling analysis is the possible existence of a single large felsic reservoir which implies that a felsic eruption should not be ruled out for the near future, though a basalt eruption is generally considered as the most likely scenario. More generally, the temporal geochemical evolution of the whole CDP series clearly shows that felsic derivatives were almost exclusively produced at the end of the CDP time evolution (Boivin *et al.*, 2009), that is to say close to present day. Since CDP trachytes derive primarily from basalt fractionation (Maury *et al.*, 1980; Villemant *et al.*, 1980), as opposed to crustal melting, this in turn implies that the rate of basalt influx must have slowed down prior to the period of trachyte production (10-20 ky) so as to allow the system to cool substantially. Such a decrease may correspond to a progressive and irreversible magmatic shut

down of the area. Alternatively, fluctuations in recharge rates are known in arc settings (e.g. Druitt *et al.*, 2012) and there are no reasons why basalt supply rates would not fluctuate as well in continental settings. On this basis, the observed decay in basalt eruption rate following trachyte eruptions cannot be taken as evidence of the waning stage of magmatic activity at CDP.

Comparison with the trachytic system of the Phlegrean Fields

Only one experimental study has been performed starting from a phono-trachytic liquid, in order to determine the storage conditions of the Breccia Museo eruption in the Phlegrean Fields in Italy (Fabbrizio & Carroll, 2008; Fabbrizio *et al.*, 2009). Yet, this study concerns alkaline magmas in a subduction context (not rifting as for CDP). Two starting compositions have been used, PR8 pumice with 60.4 SiO_2, 3.9 Na_2O, 9.1 K_2O, in wt %, and ZAC obsidian with 62.2 SiO_2, 6.2 Na_2O, 7.1 K_2O, in wt %, which both represent less evolved compositions (no normative quartz and presence of nepheline and olivine) than the CDP trachytic series. The investigated range of experimental conditions covers *P* from 50 to 200 MPa, *T* from 700 to 885°C, NNO+1 and H_2O saturation. At 200 MPa, the liquidus phase in PR8 and ZAC are the Fe-Ti oxides, crystallizing at $T > 850$°C, followed by Bt, CPx, and Afs as *T* decreases. The main difference between the phase assemblages at 200 MPa of Breccia Museo and the more differentiated CDP trachytes is the absence of Am in the Breccia Museo, whereas present for $T > 775$°C in CLI and VAS (Figure 10e-f). Fabbrizio & Carroll (2008) proposed that higher K_2O/Na_2O molar ratio (0.9 in the Breccia Museo against 0.7 in CLI) favours Bt crystallisation at the expense of Am. However, Am and Bt are both found in CLI so that it is not clear whether the difference in phase appearance can be ascribed to the K_2O/Na_2O ratio. We can note that at 200 MPa, the *T* appearance of both Cpx and Afs decrease with increasing bulk SiO_2 content of the trachyte (i.e. from PR8, ZAC, to CLI).

The major-phase assemblage and proportion of the Breccia Museo rocks have been experimentally reproduced under H_2O-saturated conditions at 780°C and *P* from 140 to 200 MPa, which are shallower, but otherwise comparable, storage conditions to CDP. The Breccia Museo eruption has been interpreted as a chemically-zoned reservoir, in which the early eruptive phase tapped the most differentiated level followed by the drainage of the underlying less evolved magma (Fabbrizio & Carroll, 2008). Such models of a compositionally-zoned single reservoir are often proposed where large magma volumes are involved (e.g. Bishop

Tuff; Johnston *et al.*, 1994), but they may apply as well to smaller magma volumes such as involved in the CDP monogenic volcanoes, owing to evidence of compositional zoning of some eruptions (e.g. the Pariou eruptive sequence successively displayed trachy-andesite and basaltic products; Boivin *et al.*, 2009). Both studies agree for a H_2O-rich nature of the trachytic or phono-trachytic liquids.

PETROGENETIC IMPLICATIONS

The CDP volcanic series results from the fractional crystallisation of silica-deficient alkali basalts. The differentiation is characterized by an important increase of silica activity and leads to oversaturated trachytes. Maury *et al.* (1980) proposed that the increase of silica activity results mainly from the fractionation of amphibole (depleted in SiO_2 with respect to the residual liquid) at the level of intermediate compositions. These authors used least-squares-mass balance calculations to estimate fractionating minerals and their proportions in the successive cumulates. Amphibole is a major fractionating phase (up to 28 wt %), suggesting that high water fugacity prevails during this process. Considering a water content of ~8 wt % in the trachytic liquids (retrieved from melt inclusions and phase equilibria) and assuming a water content of 2 wt % in amphibole, we calculate a minimum amount of dissolved water in parental basaltic magmas of ~1.5 wt %, using the modal proportions of fractionating phases calculated by Maury *et al.* (1980) (Table 16). This suggests that wet conditions prevail during the differentiation of alkaline continental series, which agrees with the model of "wetspots", rather than "hotspots" proposed by Wilson (2008).

The documented water content of ~1.5 wt % is comparable to estimations in oceanic island basalts (OIB): Reunion basalt (0.7 to 1 wt %, Bureau *et al.*, 1999) or Hawaii alkalic basalt (1.3-1.9 wt %; Dixon *et al.*, 1997). Water has already been recognised has playing a key role in generating OIB (e.g. Schilling *et al.*, 1980; Dixon *et al.*, 1997). However, liquid lines of descent observed in oceanic and continental intra-plate contexts are radically different. Indeed, the differentiated magmas are undersaturated with silica in oceanic context (e.g. phonolites), whereas silica-oversaturated in continental context (e.g. trachytes), which suggests contrasting processes in the magma en route to the surface for these two geodynamical contexts and/or substantial differences in mantle sources.

ACKNOWLEDGMENT

We thank Olivier Rouer and Ida Di Carlo for assistance with SEM and EMP, and Patricia Benoist for the ASS measurements. We also thank Juan Andujar for discussions about alkaline magmas and amphiboles. We are grateful to Catherine Deniel and Didier Miallier for update information on the paragenesis and ages of the CDP trachytes. We are grateful to Jenni Barclay, Ray Macdonald, and Mike Carroll for their beneficial reviews, and to Marjorie Wilson for the careful editorial handling.

FUNDING

This project mostly benefited from the own resources of the Institut des Sciences de la Terre d'Orléans (ISTO), which mainly come from the Institut des Sciences de l'Univers (INSU), Centre National de la Recherche Scientifique (CNRS), and Orléans University.

REFERENCES

Andersen, D. J., Lindsley, D. H. & Davidson, P. M. (1993). Quilf: a Pascal program to assess equilibria among Fe-Mg-Ti oxides, pyroxenes, olivine, and quartz. *Computers and Geosciences* **19**, 9, 1333-1350.

Anderson, J. L. & Smith, D. R. (1995). The effect of temperature and fO_2 on the Al-in-hornblende barometer. *American Mineralogist* **80**, 549-559.

Andujar, J., Costa, F., Marti, J., Wolff, J. A. & Carroll, M. R. (2008). Experimental constraints on pre-eruptive conditions of phonolitic magma from the caldera-forming El Abrigo eruption, Tenerife (Canary Islands). *Chemical Geology* **257**, 173-191.

Arnaud, N. (1989). Les éruptions trachytiques de la Chaîne des Puys: Apport de l'étude des enclaves congénères à l'évolution des magmas trachytiques. Master Memoir, University of Clermont-Ferrand, France.

Annen, C., Pichavant, M., Bachmann, O. and Burgisser, A. (2008). Conditions for the growth of a long-lived magma chamber below Mount Pelée volcano (Martinique, Lesser Antilles Arc). *Journal of Geophysical Research*, B07209, doi:10.1029/2007JB005049.

Babuska, V., Plomerova, J., Vecsey, L., Granet, M. & Achauer, U. (2002). Seismic anisotropy of the French Massif Central and predisposition of Cenozoic rifting and volcanism by Variscan suture hidden in the mantle lithosphere. *Tectonics* **21**, 11-20.

Bachmann, O, Dungan, M. A. & Lipman, P. W (2002). The Fish Canyon magma body, San Juan volcanic field, Colorado: Rejuvenation and eruption of an upper crustal batholith. *Journal of Petrology* **43**, 1469-1503.

Bacon, C.R. & Hirschmann, M.M. (1988). Mg/Mn partitioning as a test for equilibrium between coexisting Fe-Ti oxides. *American Mineralogist* **73**, 57-61.

Behrens, H. (1995). Determination of water solubilities in high-viscosity melts: an experimental study on $NaAlSi_3O_8$ and $KAlSi_3O_8$ melts. *European Journal of Mineralogy* **7**, 905-920.

Berndt, J., Holtz, F. & Koepke J. (2001). Experimental constraints on storage conditions in the chemically zoned phonolitic magma chamber of the Laacher See volcano. *Contributions to Mineralogy and Petrology* **140**, 469-486.

Boivin, P., Besson, J.-C., Briot, D., Camus, G., Goër De Herve, A., Gourgaud, A., Labazuy, P., Langlois, E., Larouzière, F.-D., Livet, M., Mergoil, J., Miallier, D., Morel, J.-M., Vernet, G. & Vincent, P. M. (2009). Volcanologie de la Chaîne des Puys, Massif Central Français (5° édition). Parc Naturel Régional des Volcans d'Auvergne, 196 p. + 1/25.000 map.

Brandeis, G. & Jaupart, C. (1986). On the interaction between convection and crystallization incooling magma chambers. *Earth and Planetary Science Letters* **77**, 345-361.

Bureau, H., Métrich, N., Semet M.P. & Staudacher T. (1999). Fluid-magma decoupling in a hot-spot volcano. *Geophysical Research Letter* **26**, 3501–3504.

Burgisser, A. & Bergantz, G. W. (2011). A rapid mechanism to remobilize and homogenize highly crystalline magma bodies. *Nature* **471**, 212–215.

Burnham, C. W. (1979). The importance of volatiles constituents. In: Yoder, H.S. (ed.) *The Evolution of the Igneous Rocks: Fifth Anniversary Perspectives*. Princeton, NJ: Princeton University Press, pp. 439–482.

Burnham, C. W., Holloway, J. R. & Davis, N. F. (1969). Thermodynamic properties of water to 1000°C and 10 000 bars. *Geological Society of America, Special Paper* **132**, 1–96.

Camus, G. (1975). La Chaîne des Puys (Massif Central Français): Etude structurale et volcanologique. PhD thesis, University of Clermont-Ferrand, France.

Camus, G., Goer de Herve, A., Kieffer, G., Mergoil, J. & Vincent, P. M. (1975). Volcanologie de la Chaîne des Puys. Parc Naturel Régional des Volcans d'Auvergne, 112 *P*. + 1/25.000 map.

Caricchi, L., Ulmer, P. & Peccerillo A. (2008). A high-pressure experimental study on the evolution of the silicic magmatism of the Main Ethiopian Rift. *Lithos* **91**, 46-58.

Carslaw, H. S. & Jaeger, J. C. (1959). *Conduction of Heat in Solids*, Oxford Univ. Press, London, 510 pp.

Cottrell, E., Gardner, J. E. & Rutherford, M. J. (1999). Petrologic and experimental evidence for the movement and heating of the pre-eruptive Minoan rhyodacite (Santorini, Greece). *Contribution to Mineralogy and Petrology* **135**, 315–331.

Couch, S., Sparks, R. S. J. & Carroll, M. R. (2001). Mineral disequilibrium in lava explained by convective self-mixing in open magma chambers. *Nature* **411**, 1037– 1039.

Costa, F., Scaillet, B. & Pichavant, M. (2004). Petrological and experimental constraints on the preeruption conditions of Holocene dacite from Volcán San Pedro (36ºS, Chilean Andes) and the importance of sulphur in silicic subduction-related magmas. *Journal of Petrology* **45,** 855-881.

Czamanske, G. K. & Wones, D. R. (1973). Oxidation during magmatic differentiation, Finmarka Complex, Oslo area, Norway: Part 2: the mafic silicates. *Journal of Petrology* **14**, 349-380.

Dall'Agnol, R., Scaillet, B. & Pichavant, M. (1999). An experimental study of a lower Proterozoic A-type granite from the Eastern Amazonian craton, Brazil. *Journal of Petrology* **40**, 1673-1698.

Di Carlo, I., Rotolo, S. G., Scaillet, B., Buccheri, V. & Pichavant, M. (2010). Phase equilibrium constraints on pre-eruptive conditions of recent felsic explosive volcanism at Pantelleria Island, Italy. *Journal of Petrology* **51**, 2245-2276.

Deer, W. A., Howie, R. A. & Zussman, J. (1992). An introduction to the rock-forming minerals, 2nd edition. Longman Scientific and Technical, London.

Devine, J. D., Gardner, J. E., Brack, H. P., Layne, G. D. & Rutherford, M. J. (1995). Comparison of microanalytical methods for estimating H_2O contents of silicic volcanic glasses. *American Mineralogist* **80**, 319-328.

Devine, J. D., Rutherford, M. J., Norton, G. E. & Young, S. R. (2003). Magma storage region processes inferred from geochemistry of Fe-Ti oxides in andesitic magma, Soufrière Hills volcano, Montserrat, W.I. *Journal of Petrology* **44**, 1375-1400.

Di Matteo, V., Carroll, M. R., Behrens, H., Vetere, F. & Brooker, R. A. (2004). Water solubility in trachytic melts. *Chemical Geology* **213**, 187-196.

Dixon, J. E., Clague, D. A., Wallace, P. & Poreda, R. (1997). Volatiles in alkalic basalts from the North Arch Volcanic Field, Hawaii: extensive degassing of deep submarine-erupted alkalic series lavas. *Journal of Petrology* **38**, 911–939.

Druitt, T., Costa, F., Deloule, E., Dungan, M. & Scaillet, B. (2012). Decadal to monthly timescales of magma transfer and reservoir growth at a caldera volcano. *Nature* **482**, 77-80. doi:10.1038/nature10706.

Fabbrizio, A. & Carroll, M. R. (2008). Experimental studies of the differentiation process and pre-eruptive conditions in the magmatic system of Phlegrean Fields (Naples, Italy). *Journal of Volcanology and Geothermal Research* **171**, 88–102.

Fabbrizio, A., Rouse, P. J. & Carroll, M. J. (2006). New experimental data on the biotite + magnetite + sanidine saturated phonolitic melts and application to the estimation of magmatic water fugacity. *American Mineralogist* **91**, 1863-1870.

Fabbrizio, A., Scaillet, B. & Carroll, M. J. (2009). Estimation of pre-eruptive magmatic water fugacity in the Phlegrean Fields, Naples, Italy. *European Journal of Mineralogy* **21**, 107-116.

Foury, P. (1983). Etude pétrologique et expérimentale (à une atmosphère) d'une série alcaline continentale: la série de la Chaîne des Puys (MCF). 3rd Cycle Thesis, University of Clermont-Ferrand, France.

Fowler, S. J., Spera, F. J., Bohrson, W. A., Belkin, H. E. & De Vivo, B. (2007) Phase equilibria constraints on the chemical and physical evolution of the Campanian ignimbrite. *Journal of Petrology* **48**, 459-493.

Freise, M., Holtz, F., Koepke, J., Scoates, J. & Leyrit, H. (2003). Experimental constraints on the storage conditions of phonolites from Kerguelen Archipelago. *Contributions to Mineralogy and Petrology* **145**, 659-672.

Gardner, J. E, Rutherford, M. J., Carey, S. & Sigurdsson, H. (1995). Experimental constraints on pre-eruptive water contents and changing magma storage prior to explosive eruptions of Mount St Helens volcano. *Bulletin of Volcanology* **57**, 1-17.

Ghiorso, M. S. & Sack, R. O. (1991). Fe-Ti oxide geothermometry: thermodynamic formulation and estimation of intensive variables in silicic magmas. *Contributions to Mineralogy and Petrology* **108**, 485-510.

Guittet, J. (1996). Géochimie isotopique Sr et Nd des trachytes de la Chaîne des Puys (MCF): Datation par thermoluminescence et déséquilibres radiocatifs du dôme du Sarcoui. M2 Memoir, University of Clermont-Ferrand, France.

Harms, E., Gardner, J. E. & Schmincke, H.-U. (2004). Phase equilibria of the Lower Laacher See tephra (east Eifel, Germany): constraints on pre-eruptive storage conditions of a phonolitic magma reservoir. *Journal of Volcanology and Geothermal Research* **134**, 125-138.

Holland, T. & Blundy, J. (1994). Non-ideal interactions in calcic amphiboles and their bearing on amphibole-plagioclase thermometry. *Contributions to Mineralogy and Petrology* **116**, 433-447.

Hollister, L. S., Grissom, G. C., Peters, E. K., Stowell, H. H. & Sisson, V. B. (1987). Confirmation of the empirical correlation of Al in hornblende with pressure of solidification of calc-alkaline plutons. *American Mineralogist* **72**, 231-239.

Holtz, F. & Johannes, W. (1991). Genesis of peraluminous granites I. Experimental investigation of melt compositions at 3 and 5 kbars and various H_2O activities. *Journal of Petrology* **32**, 935-958.

Huppert, H. E. & Sparks, R. S. J. (1988a). Melting of the roof of a chamber containing a hot, turbulently convecting fluid. *Journal of Fluid Mechanics* **188**, 107–131.

Huppert, H. E. & Sparks, R. S. J. (1988b). The generation of granitic magma by intrusion of basalt into continental crust. *Journal of Petrology* **29**, 3, 599– 624.

Jannot, S., Schiano, P. & Boivin P. (2005). Melt inclusions in scoria and associated mantle xenoliths of Puy Beaunit Volcano, Chaîne des Puys, Massif Central, France. *Contributions to Mineralogy and Petrology* **149**, 600-612.

Johnson, M. C. & Rutherford, M. J. (1989). Experimentally determined conditions in the Fish Canyon Tuff, Colorado, Magma chamber. *Journal of Petrology* **30**, 3, 711-737.

Knoche, R., Dingwell, D. B. & Webb, S. L. (1995). Melt densities for leucogranites and granitic pegmatites: partial molar volumes for SiO_2, Al_2O_3, Na_2O, K_2O, Li_2O, Rb_2O, Cs_2O, MgO, CaO, SrO, BaO, B_2O_3, P_2O_5, F_2O_{-1}, TiO_2, Nb_2O_5, Ta_2O_5, and WO_3. *Geochimica and Cosmochimica Acta* **59**, 22, 4645-4652.

Koyaguchi, T. & Kaneko, K. (1999). A two-stage thermal evolution model of magmas in continental crust. *Journal of Petrology* **40**, 2, 241–254.

Koyaguchi, T. & Kaneko, K. (2000). Thermal evolution of silicic magma chambers after basalt replenishments. *Transactions of the Royal Society of Edinburgh Earth Sciences* **91**, 47– 60.

Leake, B. E., Woolley, A. R. Arps, C. E. S., Birch, W. D., Gilbert, C. M., Grice, J. D., Hawthorne, F. C., Kato, A., Kisch, H. J., Krivovichev, V. G., Linthout, K., Laird, J., Mandarino, J. A., Maresch, W. V., Nickel, E. H., Rock, N. M. S., Schumacher, J. C., Smith, D. C., Stephenson, N. C. N., Ungaretti, L., Whittaker, E. J. W. & Youzhi., G. (1997). Nomenclature of amphiboles: Report of the subcommittee on amphiboles of the International Mineralogical Association, Commission on New Minerals and Mineral Names. *The Canadian Mineralogist* **35**, 219-246.

Le Bas, M. J., Le Maître, R. W., Streckeisen, A. & Zanettin B. (1986). A chemical classification of volcanic rocks based on the total alkali-silica diagram. *Journal of Petrology* **27**, 745-750.

Martel, C., Bourdier, J.-L., Pichavant, M. & Traineau, H. (2000). Textures, water content and degassing of silicic andesites from recent plinian and dome-forming eruptions at Mount Pelee volcano (Martinique, Lesser Antilles arc). *Journal of Volcanology and Geothermal Research* **96**, 191-206.

Martel, C., Pichavant, M., Holtz, F., Scaillet, B., Bourdier, J.-L. & Traineau, H. (1999) Effect of fO_2 and H_2O on andesite phase relations between 2 and 4 kbars. *Journal of Geophysical Research* **104**, 29453-29470.

Martel, C. & Schmidt, B. C. (2003) Decompression experiments as an insight into ascent rates of silicic magmas. *Contributions to Mineralogy and Petrology* **144**, 397-415.

Maury, R., Brousse, R., Villemant, B., Joron, J.-L., Jaffrezic, H. & Treuil, M. (1980). Cristallisation fractionnée d'un magma basaltique alcalin: la série de la Chaîne des Puys (Massif Central, France). I. Pétrologie. *Bulletin de Minéralogie* **103**, 250-266.

Merle, O. & Michon, L. (2001). The formation of the West European rift: a new model as exemplified by the Massif Central area. *Bulletin de la Société Géologique de France* **172**, 213-221.

Miallier, D., Boivin, P., Deniel, C., Gourgaud, A., Lanos, P., Sforna, M. & Pilleyre, T. (2010) The ultimate summit eruption of Puy de Dôme volcano (Chaîne des Puys, French Massif Central) about 10,700 years ago. *Comptes Rendus Geoscience* **342**, 847-854.

Miallier, D., Michon, L, Evin, J., Pilleyre, T., Sanzelle, S. & Vernet, G. (2004) Volcans de la chaîne des Puys (Massif Central, France): point sur la chronologie Vasset-Kilian-Pariou-Chopine. *Comptes Rendus Geoscience* **336**, 1345-1353.

Nekvasil, H., Dondolini, A., Horn, J., Filiberto, J., Long, H. & Lindsley, D. H. (2004) The Origin and evolution of silica-saturated alkalic suites: an experimental study. *Journal of Petrology* **45**, 693–721.

Nelson, S. A. & Hegre, J. (1990). Volcan Las Navajas, a pliocene-pleistocene trachyte/peralkaline rhyolite volcano in the northwestern Mexican volcanic belt. *Bulletin of Volcanology* **52**, 186-204.

Pallister J. S., Hoblitt, R. P. & Reyes, A. G. (1992). A basalt trigger for the 1991 eruptions of Pinatubo volcano? *Nature* **356**, 436–428.

Pichavant, M. (1987). The effects of boron and water on liquidus phase relations in the haplogranite at 1 kbar. *American Mineralogist* **72**, 1056-1070.

Prouteau, G. & Scaillet, B. (2003). Experimental constraints on the origin of the 1991 Pinatubo dacite. *Journal of Petrology* **44**, 2203-2241.

Pupin, J.-P. (1976). Signification des caractères morphologiques du zircon commun des roches en pétrologie – Base de la méthode typologique et applications. PhD thesis, University of Nice, France.

Richard, L. R. & Clarke, D. B. (1990). Amphibol: a program for calculating structural formulae and for classifying and plotting chemical analyses of amphiboles. *American Mineralogist* **75**, 421-423.

Ridolfi, F. & Renzulli, A. (2011). Calcic amphiboles in calc-alkaline and alkaline magmas: thermobarometric and chemometric empirical equations valid up to 1130°C and 2.2 GPa. *Contribution to Mineralogy and Petrology* DOI: 10.1007/s00410-011-0704-6.

Rutherford, M. J., Sigurdsson, H., Carey, S. & Davis, A. (1985). The May 18, 1980, eruption of Mount St. Helens 1. Melt composition and experimental phase equilibria. *Journal of Geophysical Research* **90**, N° B4, 2929-2947.

Scaillet, B. & Macdonald, R. (2001). Phase relations of peralkaline silicic magmas and petrogenetic implications. *Journal of Petrology* **42**, 825-845.

Scaillet, B. & Macdonald, R. (2003). Experimental constraints on the relationships between peralkaline rhyolites of the Kenya Rift Valley *Journal of Petrology* **44**, 1867-1894.

Scaillet, B. & Evans, B. W. (1999). The 15 June 1991 eruption of Mount Pinatubo. I. Phase equilibria and pre-eruption *P*-T-fO_2-aH2O. *Journal of Petrology* **40**, 381-411.

Scaillet, B., Pichavant, M. & Cioni, R. (2008). Upward migration of Vesuvius magma chamber over the past 20,000 years. *Nature* **455**, 216-219.

Scaillet, B., Pichavant, M. & Roux, J. (1995). Experimental crystallization of leucogranite magmas. *Journal of Petrology* **36**, 3, 663-705.

Schilling, J.-G., Bergeron, M. B. & Evans, R. (1980). Halogens in the mantle beneath the North Atlantic. *Philosophical Transactions of the Royal Society of London* **297**, *147*–178.

Schmidt, M. W. (1992). Amphibole composition in tonalite as a function of pressure: an experimental calibration of the Al-in-hornblende barometer. *Contribution to Mineralogy and Petrology* **110**, 304-310.

Signorelli, S. & Carroll, M. R. (2002). Experimental study of Cl solubility in hydrous alkaline melts: constraints on the theoretical maximum amount of Cl in trachytic and phonolitic melts. *Contributions to Mineralogy and Petrology* **143**, 209-218.

Snyder, D. (2000). Thermal effects of the intrusion of basaltic magma into a more silicic magma chamber and implications for eruption triggering. *Earth and Planetary Science Letters* **175**, 257-273.

Stormer, J. (1978). XLFRAC: a program for the interactive testing of magmatic differentiation models. *Computers & Geosciences* **4**, 143-159.

Turner, J. S. (1973). *Buoyancy Effects in Fluids.* Cambridge University Press.

Tuttle, O. F. & Bowen, N. L. (1958). Origin of granite in the light of experimental studies in the system $NaAlSi_3O_8$-$KAlSi_3O_8$-SiO_2-H_2O. Geological Society of America Memoir 74, 153 p.

Venezky, D. Y. & Rutherford, M. J. (1999). Petrology and Fe-Ti oxide reequilibration of the 1991 Mount Unzen mixed magma. *Journal of Volcanology and Geothermal Research* **89**, Unzen volcano Special issue, 213-230.

Villemant, B., Joron, J.-L., Jaffrezic, H. & Treuil, M. (1981). Distribution coefficients of major and trace elements: fractional crystallization in the alkali basalt series of Chaîne des Puys (Massif Central, France). *Geochimica and Cosmochimica Acta* **45**, 1997–2016.

Villemant, B., Joron, J.-L., Jaffrezic, H., Treuil, M., Maury, R. & Brousse, R. (1980). Cristallisation fractionnée d'un magma basaltique alcalin: la série de la Chaîne des Puys (Massif Central, France). II. Géochimie. *Bulletin de Minéralogie* **103**, 267-286.

Waldbaum, D. R. & Thompson, J. B. Jr. (1969). Mixing properties of sanidine crystalline solutions IV: phase diagram from equation of state. *American Mineralogist* **54**, 1274-1298.

White, S. M., Crisp, J. A. & Spera, F. J. (2006). Long-term volumetric eruption rates and magma budgets. *Geochemistry, Geophysics, and Geosystems* **7**, Q03010, doi:10.1029/2005GC001002.

Whittington, A., Richet, P., Linard, Y. & Holtz, F. (2001). The viscosity of hydrous phonolites and trachytes. *Chemical Geology* **174**, 209-223.

Wilson, M. (2008). Upper mantle plumes – hotspots or wetspots ? International Geological Congress, Oslo, Norway.

Zeyen, H., Novak, O., Landes, M., Prodehl, C., Driad, L. & Hirn, A. (1997). Refraction-seismic investigations of the northern Massif Central (France). In: Fuchs, K., Altherr, R., Mueller, B. & Prodehl, C. (eds.). *Tectonophysics* **275**, 99-117.

TABLE AND FIGURE CAPTION

Table 1. Location, lithology and age of the Chaîne des Puys trachytes used in this study.

Table 2. Bulk-rock composition, phase assemblage and proportion of the CDP trachytes.

Table 3. Selected phenocrysts and glass compositions of the CDP trachytes.

Table 4. Species and content of volatiles dissolved in the CDP glasses.

Table 5. Magnetite-Ilmenite oxythermometry.

Table 6. Amphibole-Plagioclase thermobarometry.

Table 7. Amphibole thermobarometry.

Table 8. Biotite-Alkali feldspar (sanidine)-Magnetite geohygrometry.

Table 9. Experimental conditions, phase assemblage and proportions.

Table 10. Experimental Fe-Ti oxide compositions.

Table 11. Experimental biotite compositions.

Table 12. Experimental clinopyroxene compositions.

Table 13. Experimental amphibole compositions.

Table 14. Experimental feldspar compositions.

Table 15. Experimental glass compositions.

Table 16. Water content in parental basalts calculated from the model of fractional crystallisation of Maury *et al.* (1980).

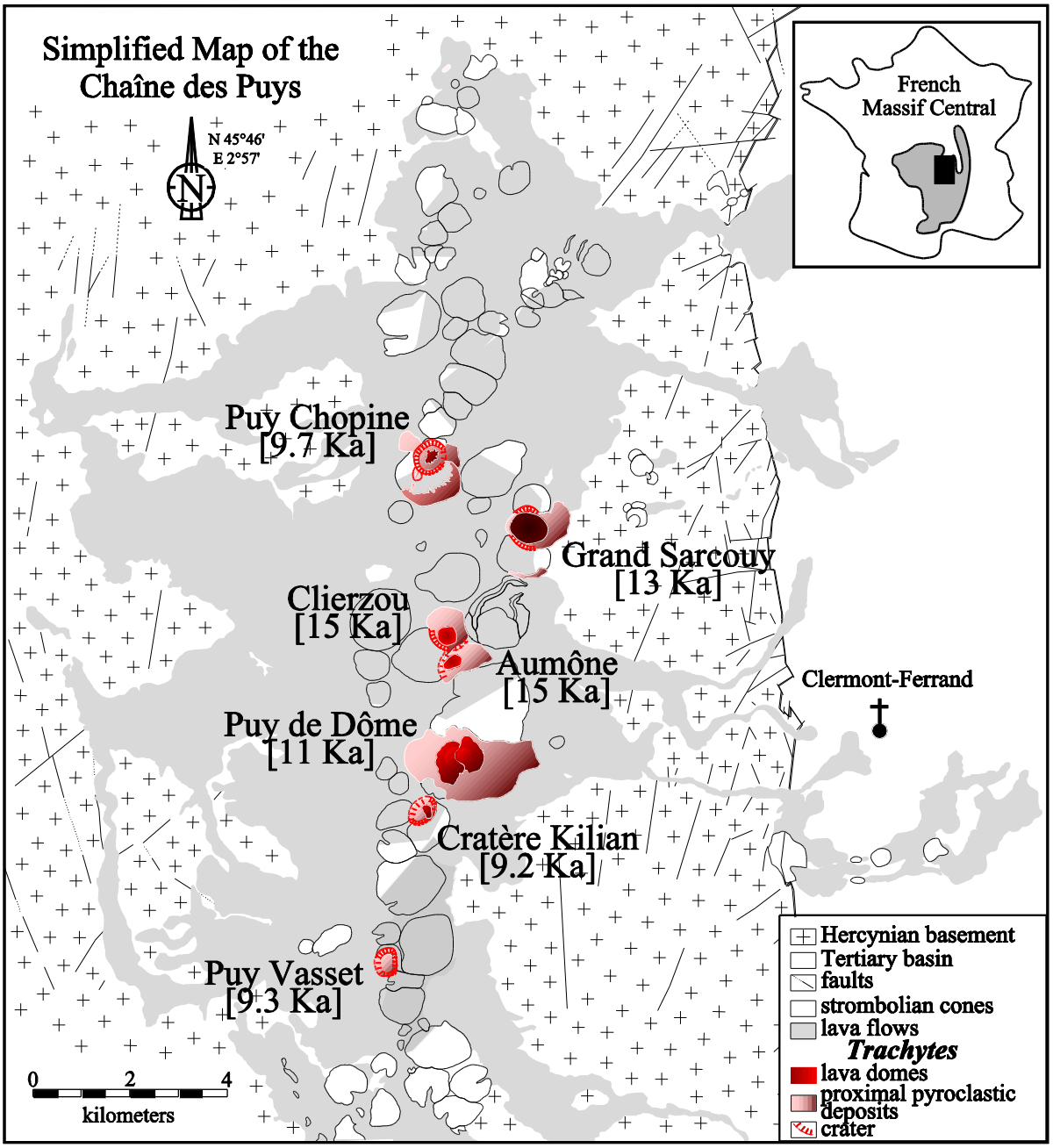

Figure 1

Figure 1. Geological setting of Massif Central and Chaîne des Puys.

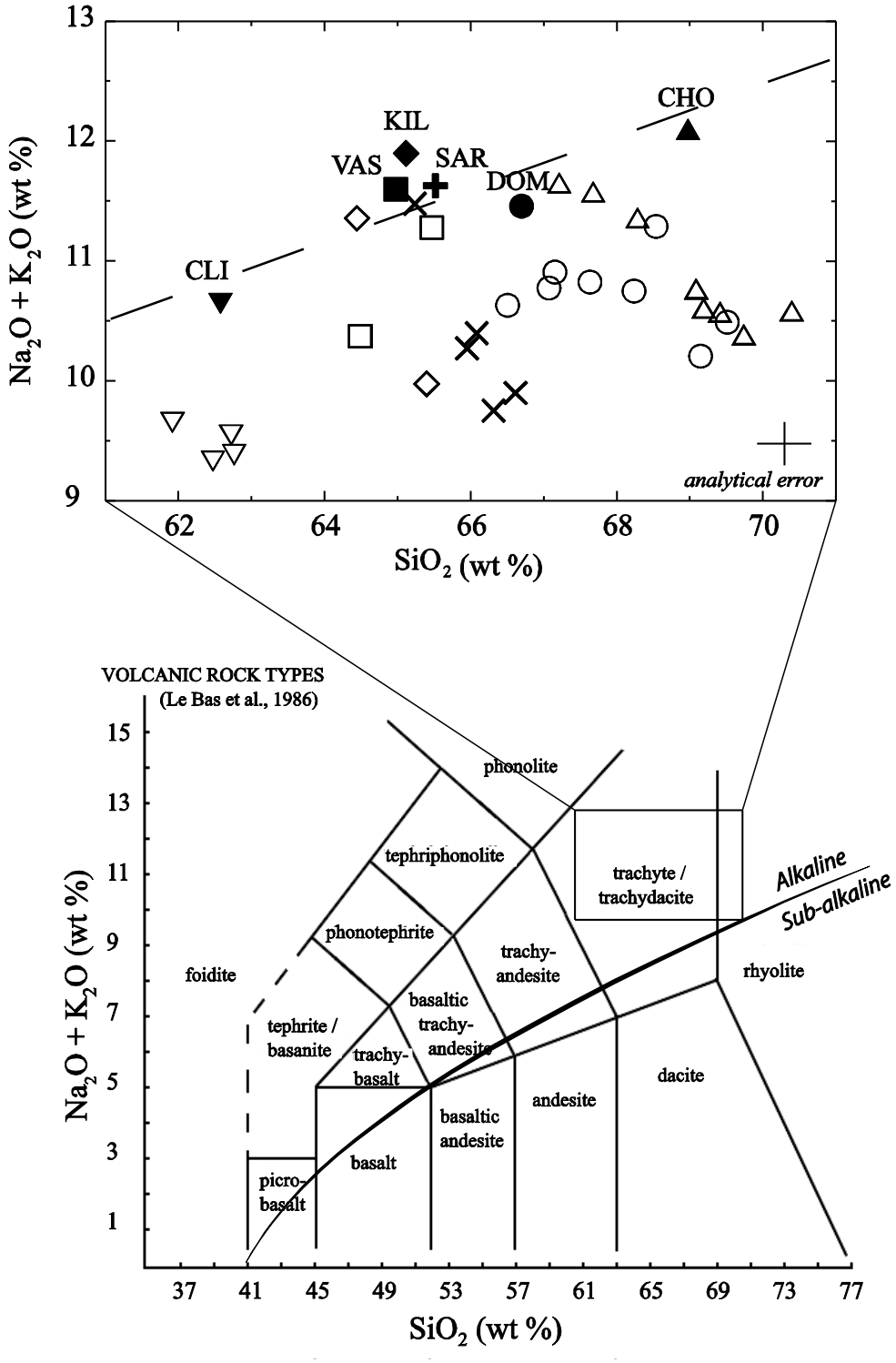

Figure 2

Figure 2. Bulk-rock composition of the CDP trachytes. Plain symbols are from the present study and open symbols are from Camus (1975), Pupin (1976), Maury *et al.* (1980), Foury

(1983), Arnaud (1989), and Guittet (1996). Upward-pointing triangles for CHO; circles for DOM; crosses for SAR; diamonds for KIL; squares for VAS; downward-pointing triangles for CLI; note that the data from the present study have higher alkali contents due to the alkali correction applied to the EMP analyses.

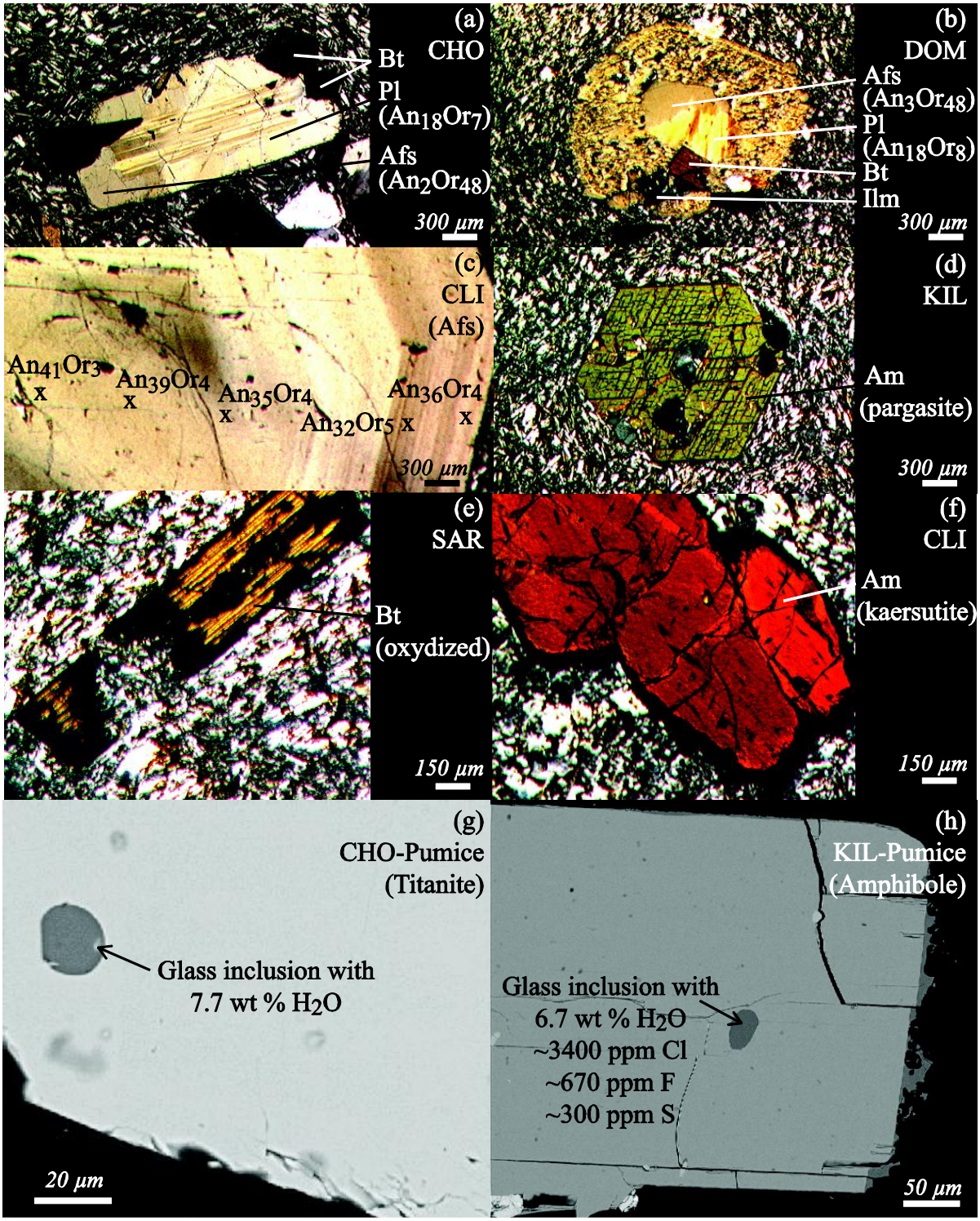

Figure 3

Figure 3. Textural details of the natural trachytes. Optical microscope pictures of minerals in CHO (a), DOM (b), CLI (c) and (f), KIL (d), and SAR (e). SEM pictures of glass inclusions trapped in a titanite from CHO_Pumice (g) and in an amphibole from KIL_Pumice (h).

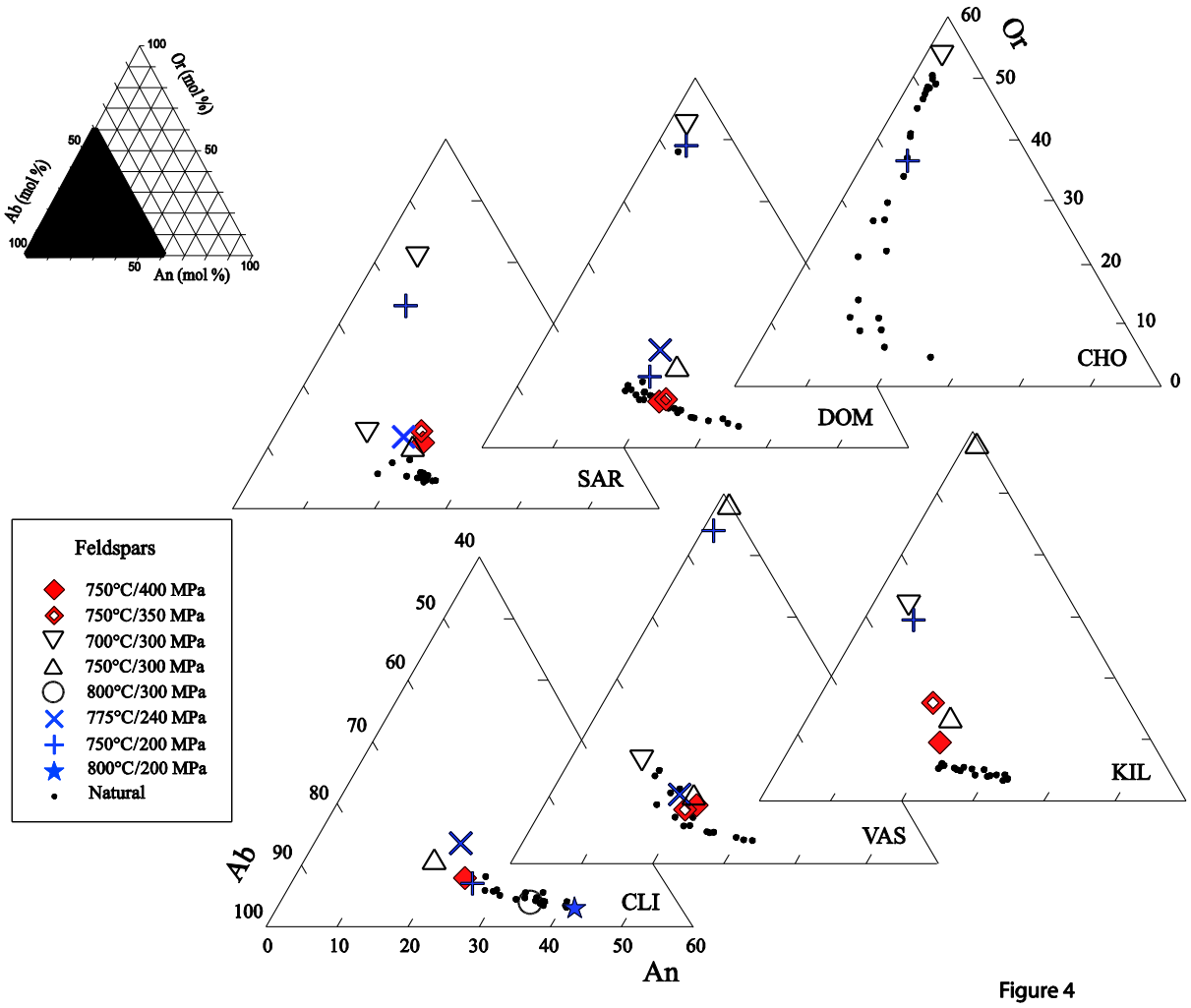

Figure 4. Feldspar compositions. The dots are the natural compositions, including those from Maury *et al.* (1980) for SAR and CLI, Foury (1983) for CLI, and Arnaud (1989) for CHO, DOM, VAS, and CLI.

Figure 5

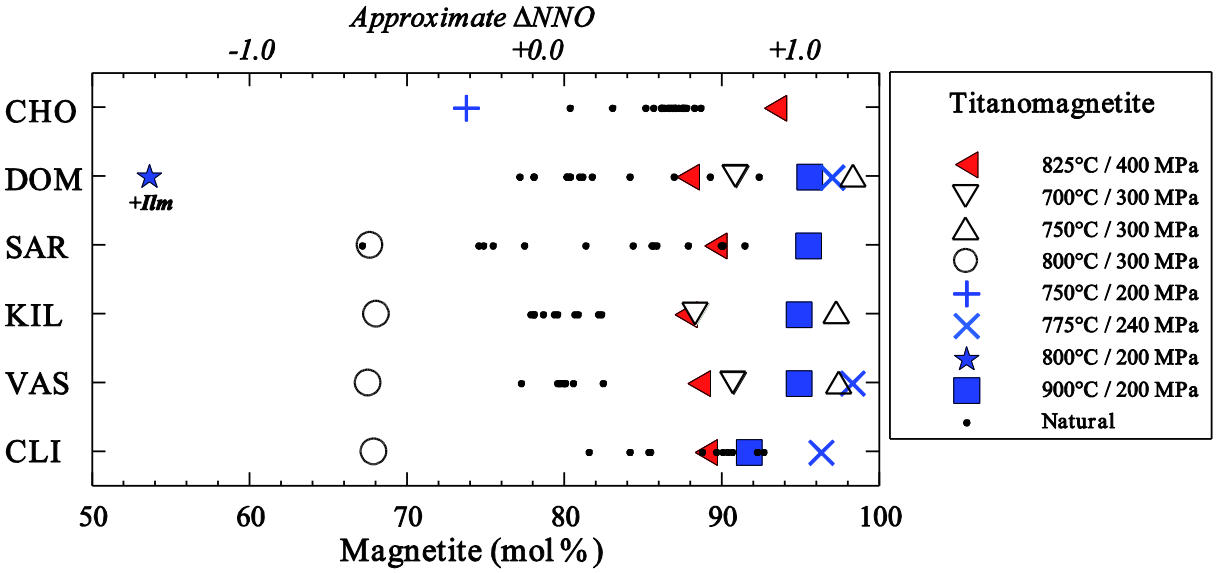

Figure 5. Magnetite compositions. The dots represent the natural compositions, including those from Maury *et al.* (1980) for DOM, SAR and CLI, Foury (1983) for CHO, SAR, and CLI, and Arnaud (1989) for DOM and VAS.

Figure 6

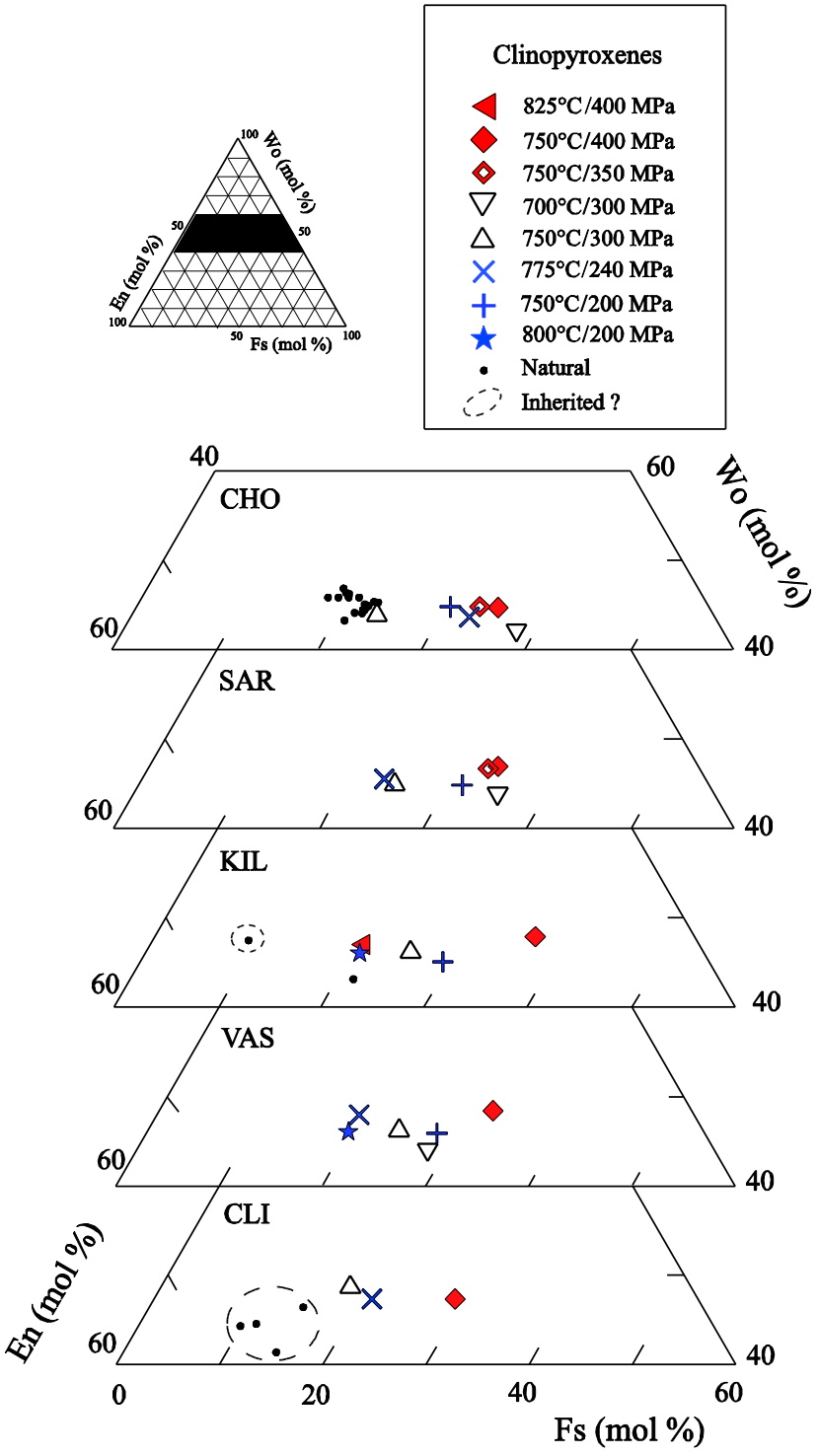
Clinopyroxenes
825°C/400 MPa
750°C/400 MPa
750°C/350 MPa
700°C/300 MPa
750°C/300 MPa
775°C/240 MPa
750°C/200 MPa
800°C/200 MPa
Natural
Inherited ?
Wo (mol %)
En (mol %)
Fs (mol %)
CHO
SAR
KIL
VAS
CLI
40
60
0
20

Figure 6. Clinopyroxene compositions. The dots are the natural compositions, including those from Maury *et al.* (1980) for CLI and Foury (1983) for CHO. The dashed circles delimit crystals that may be inherited from a mafic component.

Figure 7

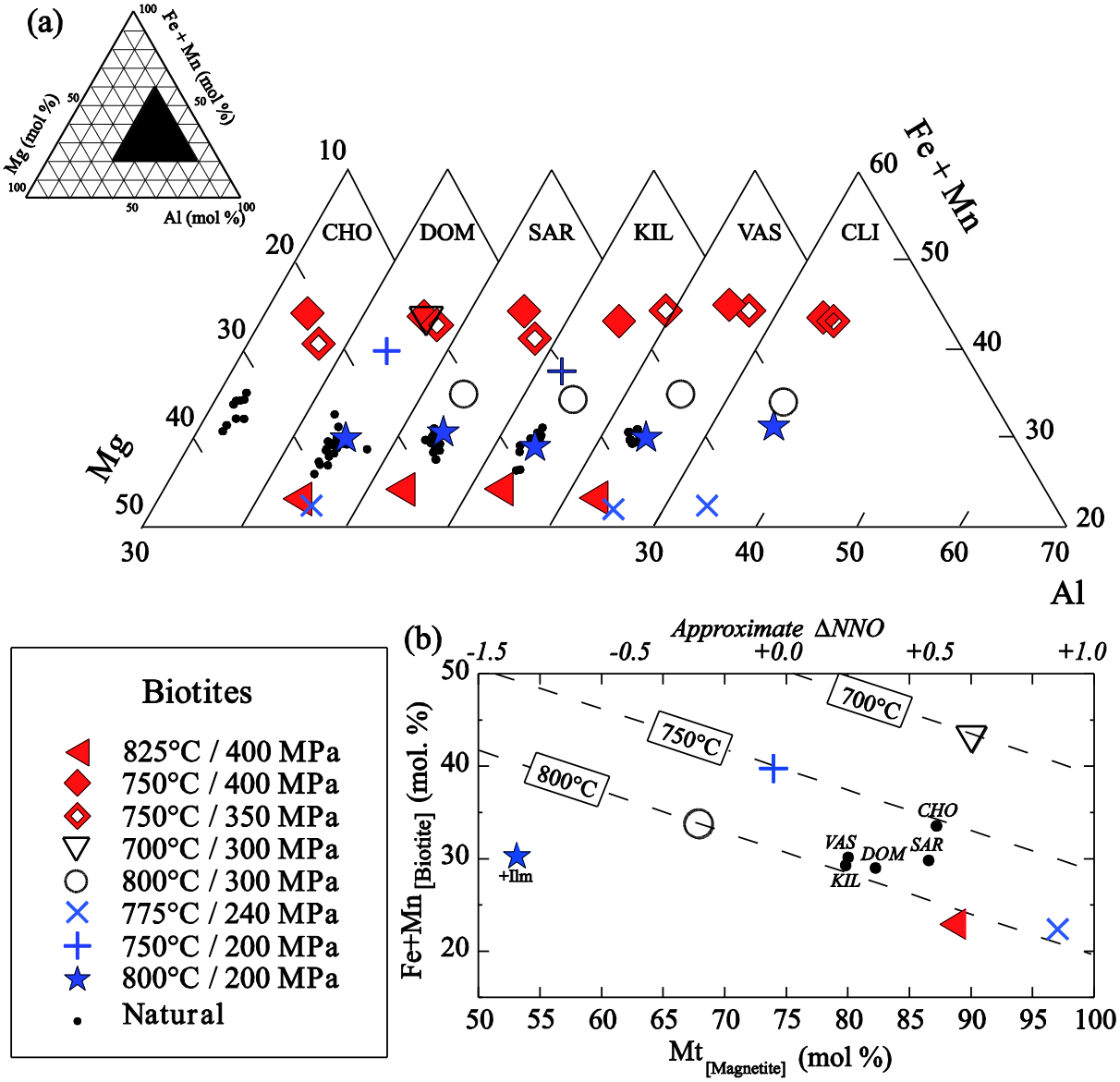

Figure 7. Biotite compositions (**a**) and cross-referencing with magnetite compositions (**b**). The dots are the natural compositions, including those from Maury *et al.* (1980) for DOM and SAR, Foury (1983) for CHO and SAR, and Arnaud (1989) for DOM.

Figure 8

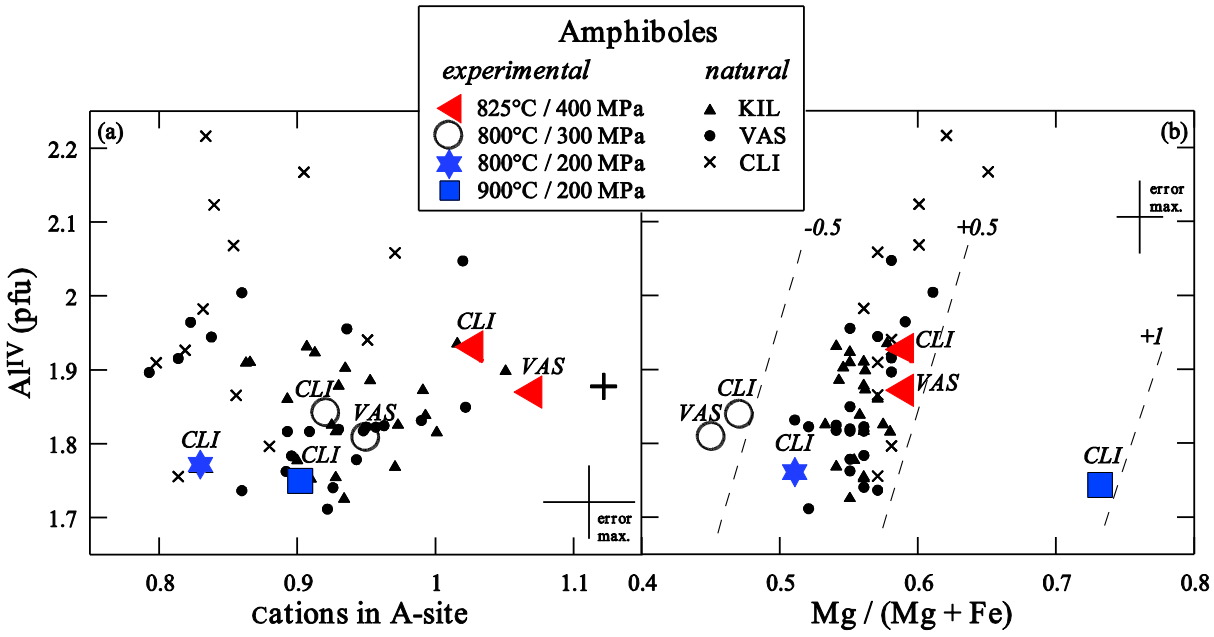

Figure 8. Amphibole compositions calculated after Richard & Clarke (1990); Al^{IV} versus the number of cations in the A-site (**a**); Al^{IV} versus Mg*=Mg/(Mg+Fe) (**b**). The natural compositions include those from Maury *et al.* (1980) for CLI, Foury (1983) for CLI, and Arnaud (1989) for VAS and CLI.

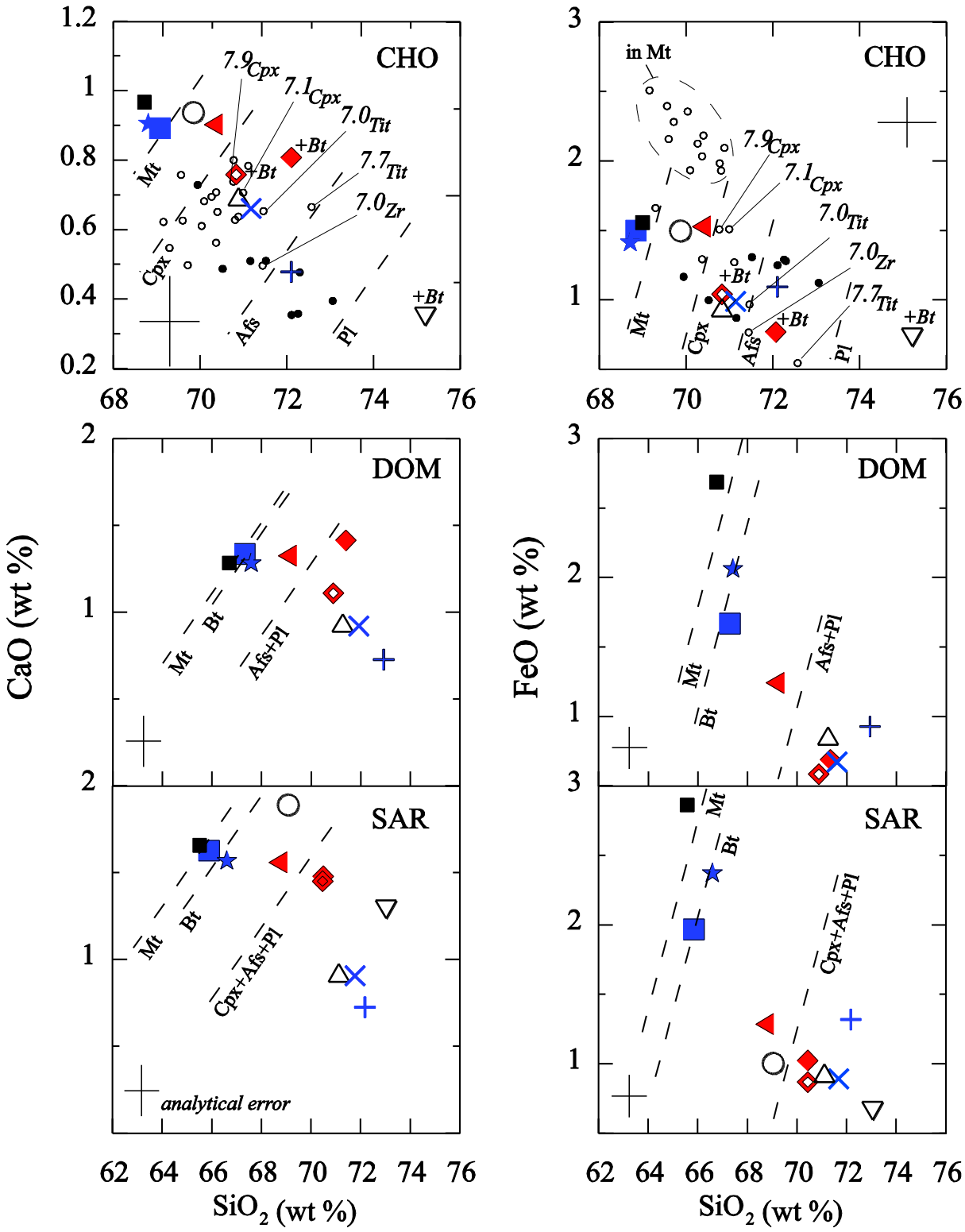
CHO
DOM
SAR
in Mt
7.9Cpx
7.1Cpx
7.0Tit
7.7Tit
7.0Zr
+Bt
Mt
Cpx
Afs
Pl
Bt
Afs+Pl
Cpx+Afs+Pl
analytical error
CaO (wt %)
FeO (wt %)
SiO2 (wt %)

Figure 9a

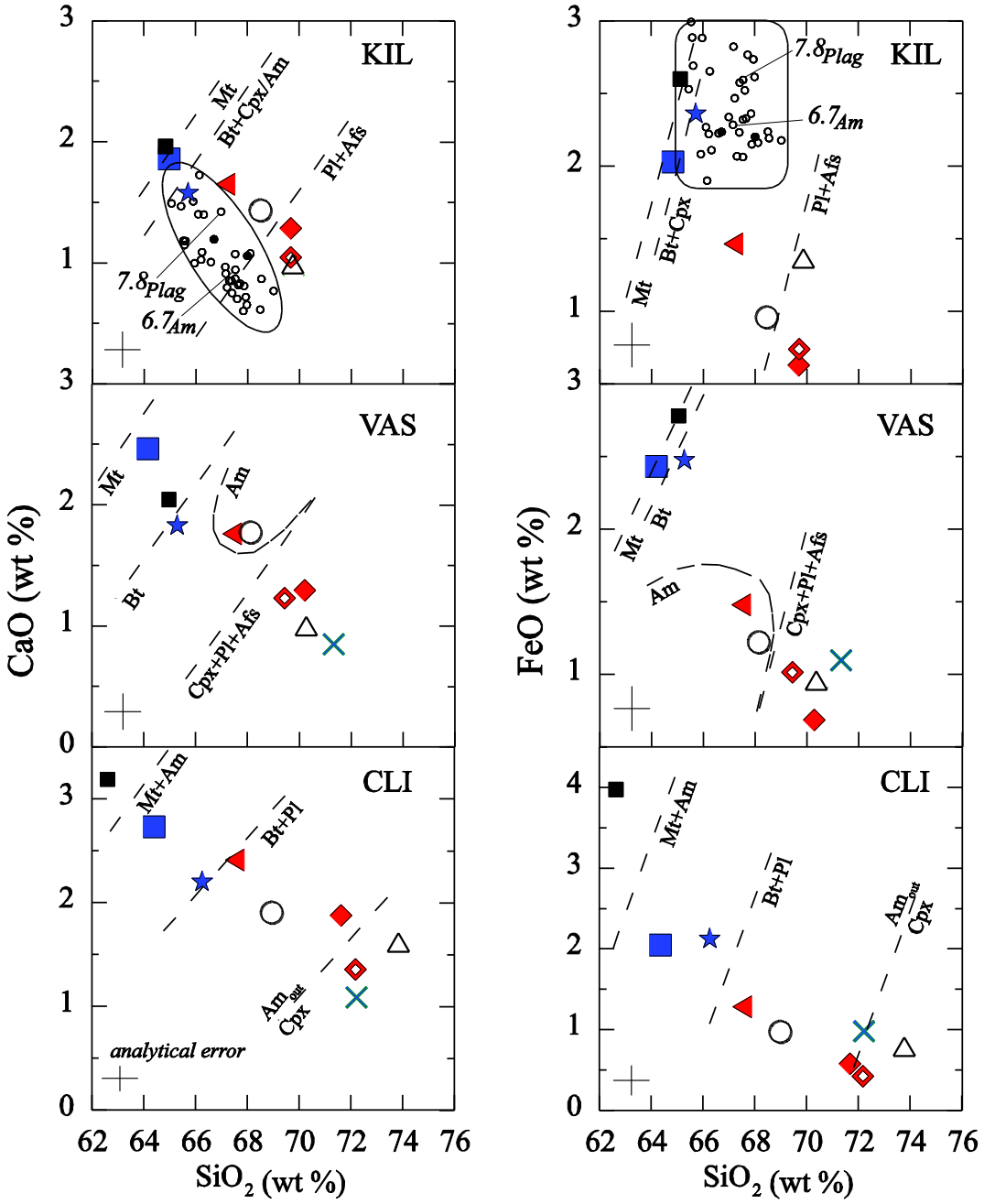
KIL
VAS
CLI
Mt
Bt+Cpx/Am
Pl+Afs
7.8Plag
6.7Am
Am
Bt
Cpx+Pl+Afs
Mt+Am
Bt+Pl
Amout
Cpx
analytical error
CaO (wt %)
FeO (wt %)
SiO2 (wt %)
Bt+Cpx
GLASSES
Experimental
700°C / 300 MPa
750°C / 300 MPa
800°C / 300 MPa
775°C / 240 MPa
750°C / 200 MPa
800°C / 200 MPa
900°C / 200 MPa
825°C / 400 MPa
750°C / 400 MPa
750°C / 350 MPa
Natural
Bulk rock
Interstitial glass
Melt inclusion
H2O wt%(host mineral)

Figure 9b

Figure 9. Glass compositions. The dots represent the natural compositions of the interstitial glasses and the little open circles are melt inclusions, some of them labelled with their volatile content and host mineral (abbreviation as in Table 2). The dashed lines represent the appearance curves of the experimental phases.

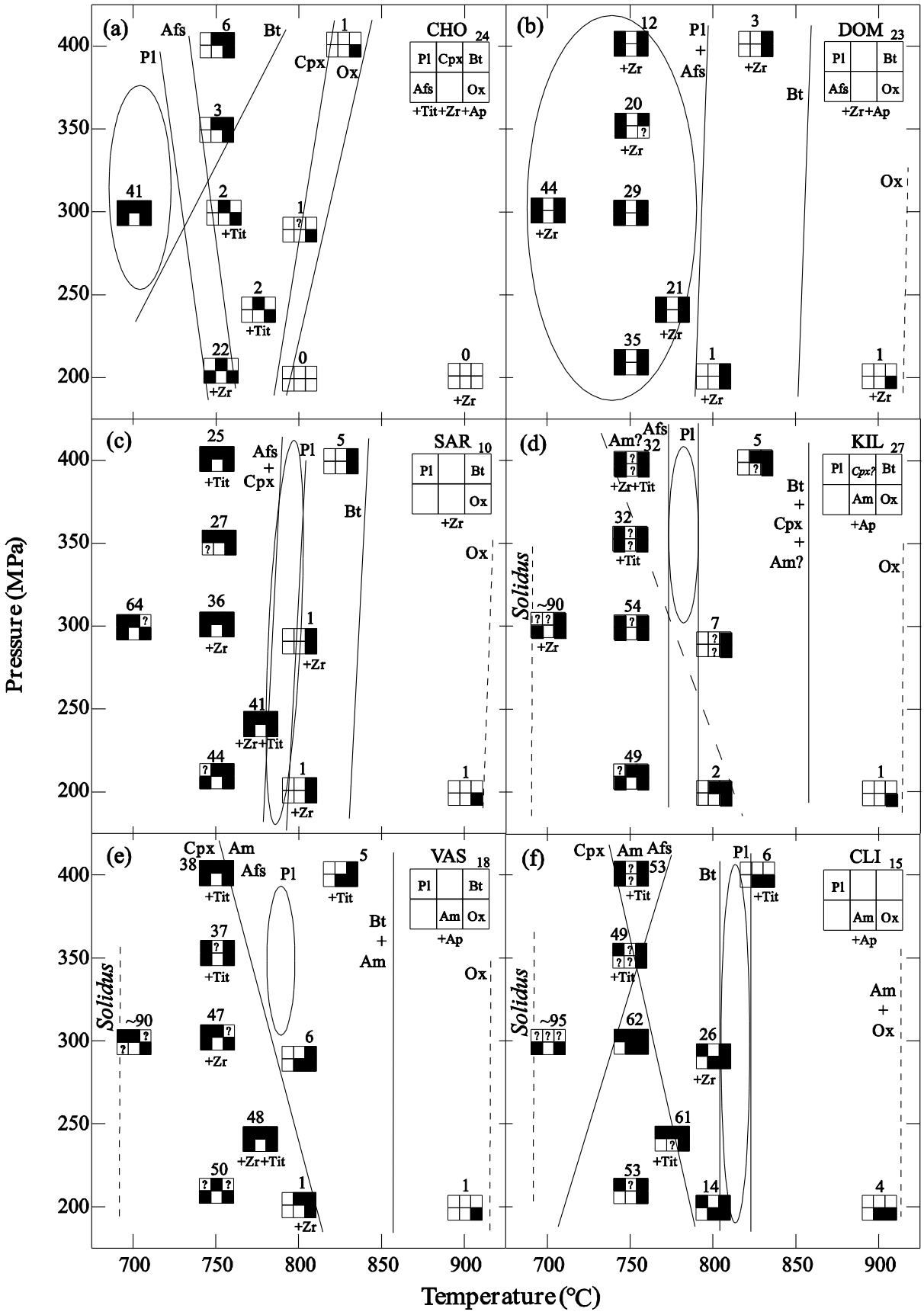
(a)
CHO 24
Pl Cpx Bt
Afs Ox
+Tit+Zr+Ap
(b)
DOM 23
Pl Bt
Afs Ox
+Zr+Ap
(c)
SAR 10
Pl Bt
Ox
+Zr
(d)
KIL 27
Pl Cpx? Bt
Am Ox
+Ap
(e)
VAS 18
Pl Bt
Am Ox
+Ap
(f)
CLI 15
Pl
Am Ox
+Ap
Solidus
Pressure (MPa)
Temperature (°C)

Figure 10

Figure 10. Phase relations for the six CDP trachytes for H_2O saturation conditions and f_{O2} ~NNO-1 to NNO+1. The block of six attached squares in the upper right corner of each phase diagram gives the natural phase assemblage (phase abbreviation as in Table 2) for a given trachyte sample, together with the phenocryst modal proportion in vol % (Table 2). The experimental phase assemblages are given by the black plain squares (same order than for the natural ones), with question-marks where the phases could not be clearly identified. The attached numbers show the experimental modal proportion in vol % (Table 9). The plain curves delimit the phase stability fields and the dashed line shows the solidus. The dashed area characterises *P-T* conditions for which the natural and experimental phase assemblages compare.

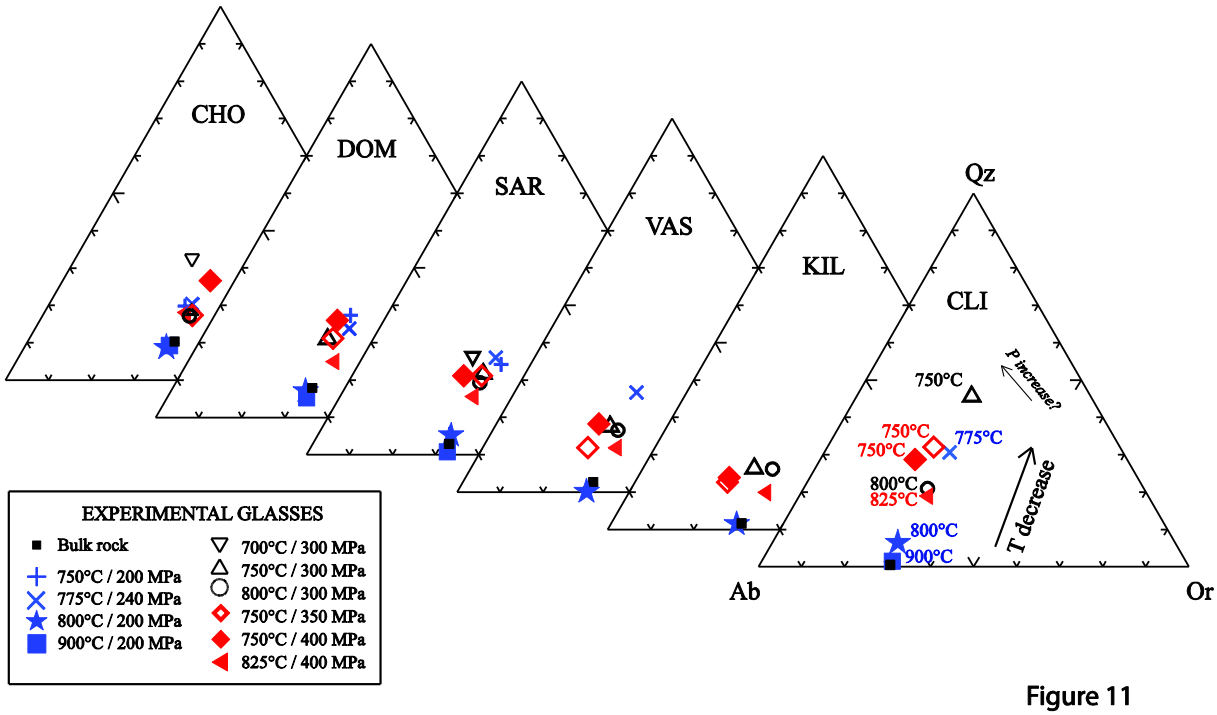

Figure 11

Figure 11. Experimental melt compositions in term of CIPW normative quartz (Qz), albite (Ab), orthoclase (Or) for each trachyte. The arrows indicate the effect of decreasing temperature on melt composition at constant pressure (i.e. an increase in crystallization), and the effect of increasing pressure at fixed temperature.

Figure 12

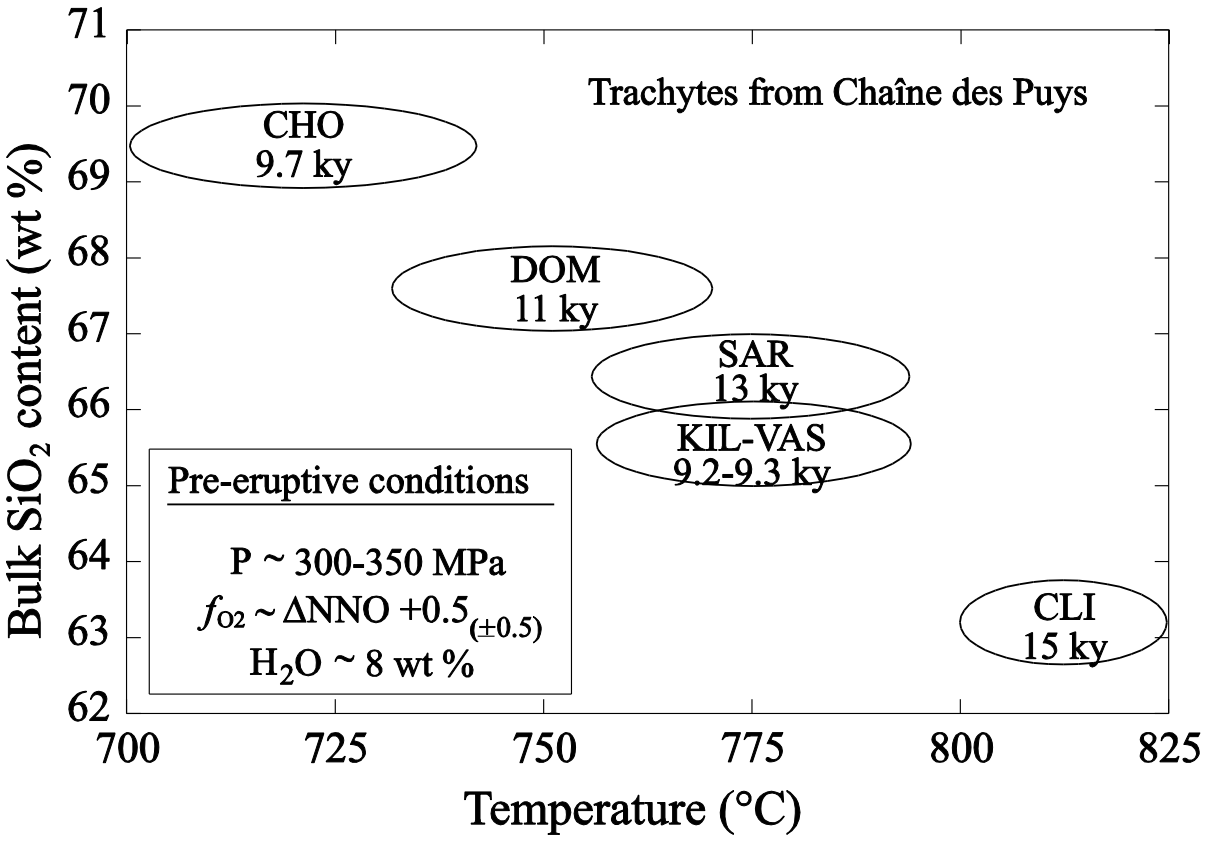

Figure 12. Pre-eruptive conditions of the CDP trachytes.

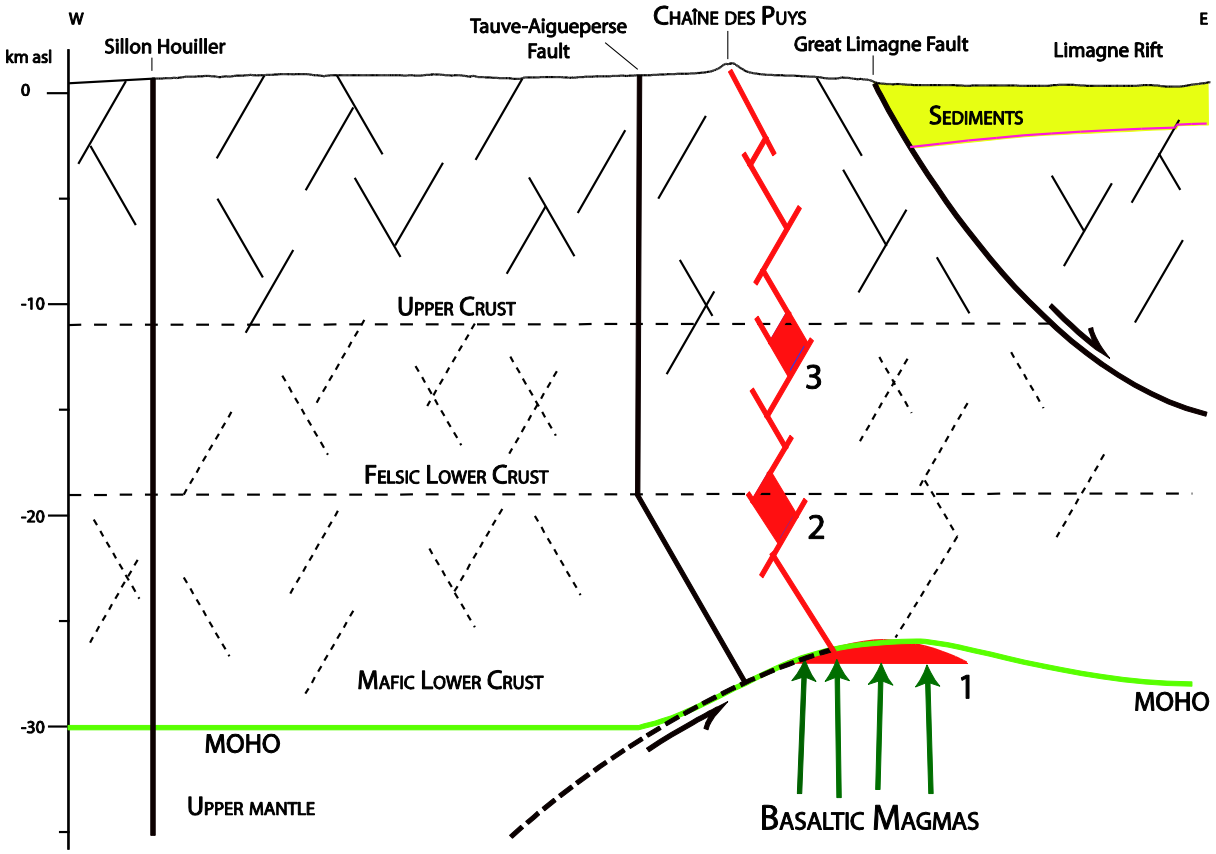

Figure 13

Figure 13. Schematic section of the continental crust below the CDP showing the possible levels of magma storage, after Zeyen *et al.* (1997), Merle & Michon (2001), Babuska *et al.* (2002), and Boivin *et al.* (2009). The horizontal and vertical scales compare (the size of the magma reservoirs is overestimated). The crust is highly crosscut by a tardi-hercynian and cenozoic network of N10-30 directed pull-apart faults. Based on seismic data, the crust can be divided into three parts separated by two discontinuities at 10-12 and 18-20 km. Therefore, the primitive magma ascending from the thermally-eroded zone by the asthenosphere uplift (1) may be temporarily retained by both discontinuities (2 and 3), with the trachytic magmas differentiating in the uppermost reservoirs (3).

Table 1. Location, lithology and age of the Chaîne des Puys trachytes used in this study.

Sample	Acronym	Age[a] (Ky)	Characteristics	Location
Cratère Kilian	KIL	9.2	Block of the lava dome	crater rim, part of the dome
Kilian pumices	KIL_Pumice	9.2	Explosive event deposit	next to crater
Puy Vasset	VAS	9.3	Block from a pyroclastic flow	Moreno Pass
Puy Chopine	CHO	9.7	Spine, grey and pinkish facies	spine
Chopine pumices	CHO_Pumice	9.7	Explosive event deposit	Lemptégy quarry
Puy de Dôme	DOM	11	Lava dome block (main facies)	East-side of the dome
Grand Sarcouy	SAR	13	Block of the lava dome	South-eastern quarry
Clierzou	CLI	15	Block of the lava dome	South quarry

[a]Edifice ages determined by radiocarbon on burned woods and tephrochronology (Miallier *et al*., 2004; pers. comm.).

Table 2. Bulk-rock composition, phase assemblage and proportion of the CDP trachytes.

Sample[a]	CHO	DOM	SAR	KIL	VAS	CLI
Bulk-rock composition[b]						
SiO_2	68.96(12)	66.68(13)	65.50(14)	65.10(36)	64.96(36)	62.56(23)
Al_2O_3	15.70(23)	16.49(11)	16.98(13)	17.02(18)	17.11(16)	17.16(12)
CaO	0.90(5)	1.30(5)	1.66(8)	1.93(7)	2.04(9)	3.21(8)
Na_2O	6.84(8)	6.61(8)	6.91(17)	7.32(21)	7.09(47)	6.58(6)
K_2O	5.27(12)	4.86(13)	4.73(9)	4.59(7)	4.52(9)	4.08(3)
FeO	1.56(22)	2.69(13)	2.68(10)	2.60(15)	2.60(19)	4.04(15)
MgO	0.18(2)	0.42(4)	0.53(2)	0.47(4)	0.55(5)	0.96(5)
MnO	0.21(10)	0.19(4)	0.23(8)	0.19(6)	0.26(5)	0.19(9)
TiO_2	0.20(12)	0.40(5)	0.42(5)	0.48(3)	0.50(6)	0.75(5)
P_2O_5	0.03(3)	0.17(2)	0.17(3)	0.16(7)	0.18(4)	0.29(4)
F	0.11(2)	0.16(3)	0.14(3)	0.13(2)	0.15(2)	0.14(2)
Cl	0.01(1)	0.01(1)	0.04(2)	0.01(1)	0.02(1)	0.01(1)
SO_3	0.01(1)	0.01(1)	0.01(1)	0.01(1)	0.01(1)	0.01(1)
Total	99.98	99.99	100.00	100.01	99.99	99.98
P.I.	1.08	0.99	0.97	1.00	0.97	0.89
CIPW norm (in wt %)						
Quartz	10.33	5.53	2.46	0.43	1.32	0.10
Orthoclase	31.62	28.73	27.96	27.13	26.72	24.11
Albite	52.20	55.93	58.46	61.93	59.99	55.67
Anorthite	0.00	0.98	1.35	0.03	1.52	5.24
Diopside	3.78	3.78	4.97	7.32	6.38	7.51
Hypersthene	1.45	3.72	3.41	1.73	2.52	5.08
Ilmenite	0.39	0.76	0.80	0.91	0.95	1.42
Apatite	0.07	0.40	0.40	0.38	0.43	0.69
Phenocryst proportion[c]						
Total	21 / 24	20 / 23	7 / 10	24 / 27	17 / 20	12 / 15
Mt + Ilm	1 / 2	1 / 2	<1 / 1	2 / 3	1 / 2	1 / 2
Pl	17 / 18	14 / 15	4 / 5	15 / 16	13 / 14	7 / 8
Afs	present	present				
Bt	2 / 3	5 / 6	3 / 4	5 / 6	1 / 2	
Cpx	1 / 1					
Am				2 / 2	2 / 2	4 / 5
Ap	<1	<1	<1	<1	<1	<1
Zr	<1	<1	<1	<1	<1	<1
Tit	<1					

[a]Sample as in Table 1.

[b]Bulk-rock compositions determined by EMP (corrected for Na loss), recalculated on anhydrous basis; Numbers in bracket give the statistical uncertainty on the last digits. All iron recalculated as FeO. P.I. is the Peralkalinity Index given as molar $(Na_2O+K_2O)/Al_2O_3$.

[c]Phenocryst proportion recalculated on the basis of a bubble-free matrix; Mt for magnetite; Ilm for ilmenite; Bt for biotite; Pl for plagioclase; Afs for alkali feldspar; Cpx for clinopyroxenes; Am for amphibole; Ap for apatite; Zr for zircon; Tit for titanite. The first number gives the modal proportions determined by point counting (with Pl and Afs counted together for CHO and DOM). The second number gives the phase proportion in wt % recalculated by mass balance with the appropriate mineral density (see text).

Table 3. Selected phenocryst and glass compositions of the CDP trachytes.

Sample[a]	Phase[b]	#	SiO_2	Al_2O_3	CaO	Na_2O	K_2O	FeO	MgO	MnO	TiO_2	P_2O_5	Total[c]	Calc[d]
CHO	Afs	J54	66.20	19.39	0.76	0.70	7.17	0.23	0.00	0.00	0.00	*nd*	99.99	$An_4Ab_{55}Or_{41}$
	Pl	J106	61.88	23.57	5.09	8.05	0.99	0.22	0.02	0.00	0.04	*nd*	99.86	$An_{24}Ab_{70}Or_6$
	Mt	J115	0.12	1.09	0.00	0.00	0.01	81.37	0.62	2.95	6.23	*nd*	92.39	Mt_{86}
	Mt	AH73	0.15	0.08	0.00	0.08	0.09	70.44	0.09	6.68	9.98	0.25	87.91	Mt_{78}
	Ilm	AH80	0.55	0.04	0.00	0.00	0.13	38.55	0.13	11.49	39.91	0.00	91.07	Ilm_{77}
	Bt	J91	36.14	13.32	0.03	0.63	8.68	19.48	10.74	1.44	5.47	*nd*	95.94	
	Cpx	J51	52.27	1.47	20.76	1.22	0.00	10.85	10.81	2.28	0.25	*nd*	99.92	$Wo_{45}En_{33}Fs_{22}$
CHO_Pumice	Afs	M1	66.18	19.57	0.55	5.54	8.44	0.17	0.00	0.00	0.00	0.03	100.60	$An_3Ab_{48}Or_{49}$
	Pl	AH28	63.50	20.90	2.63	7.98	1.98	0.22	0.02	0.07	0.00	0.09	97.37	$An_{14}Ab_{74}Or_{12}$
	Cpx	AH43	51.08	1.89	21.72	0.93	0.00	10.09	11.23	1.87	0.30	0.23	99.81	$Wo_{47}En_{34}Fs_{19}$
	Bt	M2	35.72	13.61	0.00	0.53	8.83	19.20	11.90	1.42	4.92	0.00	96.70	
	Mt	AI33	0.07	1.07	0.02	0.01	0.00	82.90	0.72	3.04	5.69	0.00	93.52	Mt_{88}
	Mt	AH11	0.15	1.01	0.00	0.00	0.00	77.16	0.68	3.02	5.82	0.03	88.08	Mt_{86}
	Ilm	M3	0.03	0.11	0.04	0.00	0.01	49.60	1.18	5.86	43.20	0.00	100.10	Ilm_{77}
	Tit	AI28	28.96	1.38	26.62	0.05	0.00	2.32	0.03	0.48	33.73	0.30	94.31	
	Ap	AH19	0.53	0.02	53.47	0.29	0.01	0.57	0.06	0.39	0.00	43.68	99.02	
	RG	AH9	69.89	15.42	0.72	6.57	5.59	1.17	0.04	0.30	0.23	0.07	100.00	*nd*
	RG	139	72.27	13.66	0.48	6.47	5.05	1.29	0.12	0.41	0.25	0.00	100.00	*nd*
	MI	AI21	71.37	15.57	0.50	6.12	5.39	0.77	0.05	0.00	0.13	0.09	100.00	7.0 (Zr)
	MI	AI42	71.38	16.65	0.65	4.88	5.00	0.97	0.00	0.05	0.30	0.11	100.00	7.0 (Tit)
	MI	AI27	72.50	16.90	0.66	4.10	4.90	0.55	0.02	0.00	0.28	0.08	100.00	7.7 (Tit_{AI28})
	MI	AH44	70.71	15.83	0.73	5.59	5.11	1.51	0.08	0.15	0.21	0.06	100.00	7.9 (Cpx_{AH43})
DOM	Afs	J131	65.03	19.46	0.63	5.33	8.06	0.17	0.00	0.00	0.00	*nd*	98.68	$An_3Ab_{49}Or_{48}$
	Pl	J122	61.49	24.00	5.52	7.84	0.92	0.26	0.01	0.00	0.01	*nd*	100.05	$An_{26}Ab_{69}Or_5$
	Mt	J136	0.18	1.56	0.01	0.02	0.00	80.98	1.07	2.32	6.38	*nd*	92.52	Mt_{84}
	Ilm	J149	0.13	0.15	0.00	0.01	0.00	47.25	1.06	2.16	44.31	*nd*	95.09	Ilm_{86}
	Bt	J129	36.34	13.61	0.00	0.64	8.90	18.61	11.75	0.92	5.29	*nd*	96.07	
SAR	Pl	I26	63.85	22.07	3.63	8.79	1.17	0.41	0.02	0.08	0.02	*nd*	100.05	$An_{17}Ab_{76}Or_7$
	Pl	I21	61.76	23.60	5.38	8.01	0.98	0.25	0.00	0.00	0.00	*nd*	99.99	$An_{26}Ab_{69}Or_5$
	Mt	I30	0.03	0.33	0.07	0.00	0.03	75.92	3.32	5.49	7.59	*nd*	92.78	Mt_{86}
	Ilm	I31	0.02	0.35	0.00	0.00	0.02	48.46	2.78	2.80	36.84	*nd*	91.27	Ilm_{69}
	Bt	I18	35.63	14.51	0.01	0.78	8.15	17.66	12.79	0.57	5.57	*nd*	95.68	
KIL	Pl	I114	59.71	25.22	6.95	7.31	0.68	0.33	0.00	0.04	0.05	*nd*	100.29	$An_{33}Ab_{63}Or_4$
	Mt	I109	0.12	1.75	0.03	0.04	0.00	82.11	1.39	2.92	7.98	*nd*	96.34	Mt_{81}
	Bt	I112	35.73	14.08	0.02	0.75	8.21	17.24	12.11	0.77	5.59	*nd*	94.49	
	Am	I116	41.17	11.26	11.36	2.76	1.27	15.34	10.85	0.83	3.72	*nd*	98.56	
	Cpx	*I134*	*50.67*	*4.60*	*23.14*	*0.40*	*0.02*	*4.99*	*15.05*	*0.14*	*0.86*	*nd*	*99.88*	$Wo_{48}En_{43}Fs_9$
KIL_Pumice	Am	AE85	39.72	11.12	10.68	2.61	1.28	15.46	11.07	0.90	3.38	*nd*	96.22	
	Pl	AE42	59.46	23.57	5.67	7.47	0.76	0.24	0.00	0.01	0.06	*nd*	97.25	$An_{28}Ab_{68}Or_4$
	Cpx	AE100	49.60	2.40	20.25	1.17	0.01	10.49	11.87	1.17	0.60	*nd*	98.10	$Wo_{44}En_{36}Fs_{20}$
	Bt	AE81	35.13	13.66	0.11	0.57	8.75	16.48	13.08	0.50	5.31	*nd*	93.58	
	RG	AE24	67.94	15.43	1.07	6.03	6.12	2.21	0.37	0.31	0.52	*nd*	100.00	*nd*
	MI	AE37	67.48	15.51	0.95	6.26	5.85	2.60	0.43	0.27	0.63	*nd*	100.00	7.8 (Pl_{AE42})
	MI	AE84	66.92	17.26	1.43	6.13	5.02	2.37	0.30	0.18	0.40	*nd*	100.00	6.7 (Am_{AE85})
VAS	Pl	I89	59.76	24.80	6.58	7.38	0.73	0.22	0.00	0.00	0.06	*nd*	99.55	$An_{32}Ab_{64}Or_4$
	Pl	I80	61.49	23.49	5.36	8.01	0.97	0.29	0.00	0.03	0.00	*nd*	99.65	$An_{25}Ab_{69}Or_6$
	Pl	I88	63.51	22.41	3.94	8.42	1.39	0.20	0.00	0.00	0.03	*nd*	99.90	$An_{19}Ab_{73}Or_8$
	Mt	I69	0.13	1.92	0.00	0.04	0.00	80.51	1.47	2.73	8.14	*nd*	94.94	Mt_{80}
	Bt	I64	36.22	13.49	0.00	0.70	8.34	16.96	12.41	0.70	5.50	*nd*	94.32	
	Am	I61	40.52	11.36	10.82	2.77	1.24	16.46	10.21	0.87	3.31	*nd*	97.56	
	Am	I173	39.96	12.34	11.12	2.79	1.19	15.36	10.49	0.69	3.92	*nd*	97.85	
CLI	Pl	J10	60.48	24.79	6.96	7.36	0.83	0.34	0.00	0.00	0.05	*nd*	100.76	$An_{33}Ab_{62}Or_5$

Mt	J41	0.14	0.32	0.00	0.08	0.08	79.58	2.19	3.15	4.88	*nd*	90.41	Mt_{90}
Ilm	J42	0.03	0.35	0.02	0.02	0.00	45.38	1.31	1.73	43.92	*nd*	92.78	Ilm_{88}
Am	J30	41.26	11.60	11.38	2.65	1.25	15.17	11.18	0.70	3.63	*nd*	98.84	
Am	*J7*	*39.72*	*13.63*	*11.7*	*2.58*	*1.07*	*13.39*	*11.49*	*0.22*	*5.14*	*nd*	*98.95*	
Cpx	*J2*	*48.14*	*8.47*	*20.86*	*0.82*	*0.00*	*8.13*	*12.51*	*0.14*	*2.09*	*nd*	*101.15*	$Wo_{47}En_{39}Fs_{14}$

[a]Sample name as in Table 1.

[b]Afs = alkali feldspar, Pl = plagioclase, Mt = titano-magnetite, Ilm = ilmenite, Cpx = clinopyroxenes, Am = amphibole, Tit = titanite, RG = residual glass, MI = melt inclusion; inherited phenocrysts in italic (not stable in the trachyte paragenesis). Glass compositions are recalculated on anhydrous basis.

[c]All oxides given in wt %.

[d]**Calc** gives the calculated structural formulae in mol % of anorthite (An), albite (Ab), and orthoclase (Or) for Pl, wollastonite (Wo), enstatite (En), and ferrosilite (Fs) for Cpx, magnetite (Mt), ilmenite (Ilm), and the H_2O content of the glass inclusion with the host crystal in bracket.

Table 4. Species and content of volatiles dissolved in the CDP glasses.

Sample[a]	Type[b]	SiO_2[c] (wt%)	n[d]	H_2O[e] (wt%)	Cl[f] (ppm)	S[f] (ppm)	F[f] (ppm)
CHO_Pumice	MI	68-70	4	0-8	$3400_{\pm 1400}$	$300_{\pm 300}$	$700_{\pm 300}$
	RG	70	1	~1-2	1700	900	800
KIL_Pumice	MI	65-70	47	0-8	*na*	*na*	*na*
	RG	67-69	3	~1-2	*na*	*na*	*na*
Basalt	MI	43-48	*na*	*na*	1500-2000	1000-2000	*na*
900CHO2	Liq	68.8	1	6.9	*na*	*na*	*na*
800CHO2	Liq	68.8	3	6.9	$60_{\pm 60}$	$200_{\pm 200}$	$1000_{\pm 1000}$
800CHO3	Liq	69.9	5	8.5	$300_{\pm 300}$	$100_{\pm 100}$	$600_{\pm 300}$

[a]Sample name as in Table 1; **Basalt** composition (Puy Beaunit, Chaîne des Puys) from Jannot *et al.* (2005). **800CHO2** and **800CHO3** are H_2O-saturated liquidus experiments performed starting with the CHO sample at 800°C-200 MPa and 800°C-300 MPa, respectively.
[b]**MI** = Melt Inclusion; **RG** = Residual glass.
[c]Range of SiO_2 content recalculated on anhydrous basis.
[d]Number of EMP analyses.
[e]Volatile content assumed to be mainly H_2O, measured by the EMP by-difference method, calibrated by the **900CHO2** (900°C, 200 MPa), **800CHO2** (800°C, 200 MPa), and **800CHO3** (800°C, 300 MPa) experimental glasses for which H_2O has been determined by KFT (see text).
[f]EMP analyses, $\pm$statistical error.
na for not analysed.

Table 5. Magnetite-Ilmenite oxythermometry.

Sample[a]	Mt[b]	Ilm[b]	log(Mg/Mn)[c]		GEOTHERM[d]			
			Mt	Ilm	T (°C)	log f_{O2}	ΔNNO	Mean
CHO_Pumice	AI33	M3	-0.38	-0.45	740	-14.38	+0.8	$750_{\pm 10}$°C
	AH11	M3	-0.40	-0.45	760	-13.85	+0.7	ΔNNO+0.7
DOM	J141	J149	-0.06	-0.07	787	-13.63	+0.4	
	J136	J149	-0.10	-0.07	722	-14.85	+0.7	$772_{\pm 38}$°C
	J141	J130	-0.06	-0.30	825	-12.54	+0.7	ΔNNO+0.7
	J136	J130	-0.10	-0.30	756	-13.75	+1.0	
SAR	I30	I31	0.03	0.24	888	-10.38	+1.6	
	I30	I32	0.03	0.30	884	-10.46	+1.6	$874_{\pm 29}$°C
	I33	I31	0.00	0.24	892	-10.36	+1.6	ΔNNO+1.6
	I33	I32	0.00	0.30	888	-10.44	+1.6	
	I58	I54	0.16	0.37	816	-11.74	+1.7	
VAS	A_I32	A_I33	-0.08	-0.03	976	-9.27	+1.2	$955_{\pm 21}$°C
	A_I34	A_I33	-0.02	-0.03	934	-9.81	+1.4	ΔNNO+1.3
CLI	J41	J42	0.09	0.12	635	-16.96	+1.0	$680_{\pm 45}$°C
	J31	J42	0.18	0.12	725	-14.87	+0.6	ΔNNO+0.8
800DOM2	P8	P7	0.04	0.09	796	-15.40	-1.6	$834_{\pm 38}$°C
	P8	P12	0,04	0,06	872	-13,35	-1.0	ΔNNO-1.3

[a]Sample name as in Table 1, except for **VAS** (data from Arnaud, 1989) and **800DOM2** (run product using DOM sample and performed at 800°C, 200 MPa, and ΔNNO -1).
[b]Magnetite (**Mt**) and ilmenite (**Ilm**) analysis reference as in Table 3.
[c]Chemical equilibrium test after Bacon & Hirschman (1988).
[d]Calculation after the formulation of Ghiorso & Sack (1991); ΔNNO = log f_{O2} – log f_{O2} of the NNO buffer calculated at the reference pressure of 300 MPa after Chou (1987).

Table 6. Amphibole-Plagioclase thermobarometry.

Sample[a]	Am[b]	Pl[b]	GEOTHERM[c]	
			P **(MPa)**	***T*** **(°C)**
VAS	I61	I80	200	823
			300	824
	I73	I89	300	821
CLI	J7	J10	300	830
	J30	J10	300	815
800CLI2	P75	P64	200	790

[a]Sample name as in Table 1, except for **800CLI2** (run product using CLI sample and performed 800°C and 200 MPa).

[b]Amphibole (**Am**) and plagioclase (**Pl**) analyses given in Table 3.

[c]Calculated temperature (***T***) for an assumed pressure (***P***) of 200 and 300 MPa, after the formulation of Holland & Blundy (1994).

Table 7. Amphibole thermobarometry.

Sample[a]	Amphibole[b]		AS95[c]		RR12[d]		
	#	Al_{tot}	*T* (°C)	$P_{\pm 60}$ (MPa)	$T_{\pm 25}$ (°C)	$P_{\pm 45}$ (MPa)	$\Delta NNO_{\pm 0.5}$
KIL	I116	1.98	800	391	910	341	+3.0
			850	236			
KIL_pumice	AE85	1.99	800	394	939	380	+3.4
			850	250			
VAS	I61	2.02	800	406	915	362	+3.0
			850	250			
	I173	2.20	800	477	806	351	+0.9
			850	315			
CLI	J30	2.04	800	414	782	288	+1.3
			850	257			
	J7	2.37	800	547	821	469	-0.5
			850	380			
825VAS4		2.00			942	378	+5.2
825CLI4		2.15			858	399	+3.6
800VAS3		2.03			779	270	+1.0
800CLI3		2.12	800	300	684	252	-0.3
800CLI2		2.11	800	290	828	342	+1.5
900CLI2		1.99			876	370	+4.5

[a]Sample name as in Table 1, except for the following run products: **825VAS4** and **825CLI4** performed at 825°C, 400 MPa, ~NNO+1, using VAS and CLI samples, respectively; **800VAS3 and 800CLI3** performed at 800°C, 300 MPa, ~NNO, and using VAS and CLI samples, respectively; **800CLI2** and **900CLI2** performed at 800°C and 900°C, respectively, 200 MPa, ~NNO+1, and using CLI sample;

[b]**#** gives the amphibole analysis number as in Table 3, with total Al content, $\mathbf{Al_{tot}}$ (in mol) recalculated on the basis of 13 cations after Leake *et al.* (1997).

[c]Formulation of Anderson & Smith (1995) based on $\mathbf{Al_{tot}}$ in Am; pressure (***P***) calculated for temperatures (***T***) of 800 and 850°C.

[d]Formulation of Ridolfi & Renzulli (2012), based on Am composition (recalculated on the basis of 13 cations; Leake *et al.*, 1997) with pressure (***P*)** calculated after their eq. 1b, temperature (***T*)** after their eq. 2 (without considering the last parameter on pressure "24.41Ln***P***" which increases *T* about 100°C and thus strongly deviates from the experimental *T*), and **ΔNNO** after their eq. 3.

Table 8. Biotite-Alkali feldspar (sanidine)-Magnetite geohygrometry.

T **(°C)**	**log** f_{O2} **(bar)**	**ΔNNO**	f_{H2O} **(bar)**	a_{H2O}	**H_2O melt (wt %)**
700	-15.42	+ 0.7	1177	0.59	4.0
725	-14.78	+ 0.7	1629	0.78	5.2
750	-14.17	+ 0.7	2221	1.01	> 7.0
750	-14.37	+ 0.5	1764	0.80	5.4
750	-13.97	+ 0.9	2796	1.27	> 7.0

All calculations performed for a pressure of 3000 bars. Bt, Afs, and Mt compositions from Table 3 (analyses #M2, M1, and AI33, respectively). See text for the calculation of f_{H2O}. $a_{H2O} = f_{H2O} / f_{H2O}°$ with $f_{H2O}°$ taken from Burnham *et al.* (1969). H_2O melt calculated from *P*, *T* and a_{H2O} (Burnham, 1979) with a melt having the composition of the melt inclusion #AI21 (Table 3).

Table 9. Experimental conditions, phase assemblage and proportions.

Sample[a]	Phase assemblage and proportion			
	Major phases (proportions in wt %)[b]	**ΣR²**[2,b]	**Gl/cryst**[c] **(vol %)**	**Minor phases**
	Run #2, 200 MPa, 900°C, f_{O2} ~NNO+1, 4 days			
900CHO2	$Gl_{(100)}$	0	100/0	Zr
900DOM2	$Gl_{(99)}$ + $Mt_{(1)}$	0.1	99/1	Zr
900SAR2	$Gl_{(99)}$ + $Mt_{(1)}$	0.1	99/1	
900KIL2	$Gl_{(99)}$ + $Mt_{(1)}$	0.3	99/1	
900VAS2	$Gl_{(99)}$ + $Mt_{(1)}$	0.7	99/1	
900CLI2	$Gl_{(95)}$ + $Mt_{(2)}$ + $Am_{(3)}$	0.3	96/4	
	Run #3, 200 MPa, 800°C, f_{O2} < NNO, 12 days			
800CHO2	$Gl_{(100)}$	0	100/0	
800DOM2	$Gl_{(98)}$ + $Ilm_{(<1)}$ + $Mt_{(<1)}$ + $Bt_{(1)}$	0.2	99/1	Zr
800SAR2	Gl + Ilm + Bt		99/1	Zr
800KIL2	Gl + Ilm + Bt + Cpx	0.3	98/2	
800VAS2	$Gl_{(98)}$ + $Ilm_{(<1)}$ + $Bt_{(1)}$ + $Cpx_{(1)}$	0.1	99/1	Zr
800CLI2	$Gl_{(86)}$ + $Ilm_{(1)}$ + $Bt_{(1)}$ + $Pl_{(2)}$ + $Am_{(10)}$	0.4	86/14	
	Run #4, 210 MPa, 750°C, f_{O2} ~NNO, 10 days			
750CHO2	$Gl_{(68)}$ + $Mt_{(1)}$ + $Cpx_{(3)}$ + $Afs_{(29)}$	0.8	78/22	Zr
750DOM2	$Gl_{(52)}$ + $Mt_{(2)}$ + $Bt_{(1)}$ + $Pl_{(22)}$ + $Afs_{(23)}$	0.4(1.2)	65/35	
750SAR2	Gl + Mt + Bt + Cpx + *Pl* + Afs		56/44	
750KIL2	Gl + Mt + Bt + Cpx + *Pl* + Afs		51/49	
750VAS2	Gl + Mt + *Bt* + Cpx + *Pl* + Afs		50/50	
750CLI2	Gl + Mt + Bt + *Cpx* + Pl		47/53	
	Run #5, 300 MPa, 750°C, f_{O2} ~NNO+1, 7 days			
750CHO3	$Gl_{(97)}$ + $Mt_{(1)}$ + $Cpx_{(3)}$	3.2(0.8)	98/2	Tit
750DOM3	Gl + Mt + Bt + Pl + Afs		71/29	
750SAR3	Gl + Mt + Bt + Cpx + Pl + Afs		64/36	Zr
750KIL3	Gl + Mt + Bt + *CPx/Am* + *Pl* + Afs		46/54	
750VAS3	Gl + Mt + *Bt* + Cpx + Pl + Afs		53/47	Zr
750CLI3	Gl + Mt + Bt + Cpx + Am + Pl + Afs		38/62	
	Run #6, 290 MPa, 800°C, f_{O2} ~NNO-0.5, 7 days			
800CHO3	Gl + Mt + *Cpx*		99/1	
800SAR3	$Gl_{(93)}$ + $Mt_{(1)}$ + $Bt_{(6)}$	0.6(4.3)	93/7	Zr
800KIL3	Gl + Mt + Bt + *Cpx/Am*		93/7	
800VAS3	$Gl_{(92)}$ + $Mt_{(1)}$ + $Bt_{(2)}$ + $Am_{(5)}$	0.6(4.0)	94/6	
800CLI3	$Gl_{(77)}$ + $Mt_{(2)}$ + $Bt_{(2)}$ + $Pl_{(10)}$ + $Am_{(11)}$	0.9(3.8)	74/26	Zr
	Run #7, 240 MPa, 775°C, f_{O2} ~NNO+1, 17 days			
775CHO2.5	Gl + Mt + Cpx		98/2	Tit
775DOM2.5	Gl + Mt + Bt + Pl + Afs		79/21	Zr
775SAR2.5	$Gl_{(55)}$ + $Mt_{(2)}$ + $Bt_{(2)}$ + $Cpx_{(1)}$ + $Pl_{(28)}$ + $Afs_{(12)}$	0.5(1.6)	59/41	Zr+Tit
775VAS2.5	Gl + Mt + Bt + Cpx + Pl + Afs		52/48	Zr+Tit
775CLI2.5	Gl + Mt + Bt + Cpx + Pl + *Am*		39/61	
	Run #8, 400 MPa, 825°C, f_{O2} ~NNO+1, 10 days			
825CHO4	$Gl_{(99)}$ + $Mt_{(1)}$	1.1(3.5)	99/1	
825DOM4	$Gl_{(96)}$ + $Mt_{(2)}$ + $Bt_{(3)}$	0.3(2.0)	97/3	Zr
825SAR4	$Gl_{(94)}$ + $Mt_{(1)}$ + $Bt_{(5)}$	0.4(2.9)	95/5	
825KIL4	Gl + Mt + Bt + Cpx	1.7(4.5)	95/5	

825VAS4	$Gl_{(94)}$ + $Mt_{(1)}$ + $Bt_{(<1)}$ + $Am_{(5)}$	0.3(2.7)	95/5	Tit
825CLI4	$Gl_{(88)}$ + $Mt_{(2)}$ + $Am_{(10)}$	0.9(4.7)	94/6	
	Run #9, 400 MPa, 750°C, f_{O2} ~NNO+1, 10 days			
750CHO4	$Gl_{(92)}$ + $Mt_{(1)}$ + $Bt_{(8)}$ + $Cpx_{(<1)}$	0.8(6.2)	94/6	
750DOM4	Gl + Mt + Bt + Pl + Afs		88/12	Zr
750SAR4	Gl + Mt + Bt + Cpx + Pl + Afs		75/25	Tit
750KIL4	Gl + Mt +Bt + *Cpx/Am* + Pl + Afs		68/32	Zr+Tit
750VAS4	Gl + Mt + Bt + Am + Pl + Afs		62/38	Tit
750CLI4	Gl + Mt + Bt + *Am* + Pl + Afs		47/53	Tit
	Run #10, 300 MPa, 700°C, f_{O2} ~NNO+1, 10 days			
700CHO3	Gl + Mt + Bt + Cpx + Pl + Afs		59/41	
700DOM3	Gl + Mt + Bt + Pl + Afs		56/44	Zr
700SAR3	Gl + Mt + *Bt* + Cpx + Pl + Afs		36/64	
700KIL3	Gl + Mt + Bt + *Cpx/Am* + *Pl* + Afs		~15/85	Zr
700VAS3	Gl + Mt + *Bt* + Cpx + Pl + *Afs*		~15/85	
700CLI3	Gl + Mt + *Bt* + *Cpx* + *Pl* + Afs		~5/95	
	Run #11, 350 MPa, 750°C, f_{O2} ~NNO+1, 4 days			
750CHO3.5	Gl + Mt + Bt + Cpx		97/3	
750DOM3.5	$Gl_{(79)}$ + *$Mt_{(2)}$* + $Bt_{(4)}$ + $Pl_{(15)}$ + Afs	1.1(2.6)	80/20	Zr
750SAR3.5	Gl + Mt + Bt + Cpx + Pl + *Afs*		73/27	
750KIL3.5	Gl + Mt + Bt + *Cpx/Am* + Pl + Afs		68/32	Tit
750VAS3.5	Gl + Mt + Bt + *Cpx* + Pl + Afs		63/37	Tit
750CLI3.5	Gl + Mt + Bt + *Cpx/Am* + Pl + *Afs*		51/49	Tit

[a]Run product is either CHO, DOM, SAR, KIL, VAS, or CLI (bulk-rock compositions in Table 2).

[b]Phase abbreviation as in Table 2; Phases in italic when not clearly identified. Numbers in brackets are phase proportions calculated by mass balance, with residual squares (**ΣR**) given in the next column (the main and bracketed number gives the residual square without considering Na_2O and with whole oxides, respectively, showing that the Na analysis is the main cause for some far too high **ΣR**). For 750DOM2, Mt composition is from 750DOM3; for 775SAR2.5, Mt and Bt are from 775VAS2.5 and Afs is from 750VAS3; for 750CHO4, Mt is from 750CHO3; for 750DOM3.5, Mt and Afs are from 700DOM3.

[c]Glass/crystal proportion determined by image analysis.

Table 10. Experimental Fe-Ti oxide compositions.

Run #[a]	Phase[b]	n[c]	SiO_2		Al_2O_3		CaO		Na_2O		K_2O		FeO		MgO		MnO		TiO_2		Total[d]	Mt/Ilm[e]	
900DOM2	Mt	5	0.14	*0.07*	2.26	*0.08*	0.02	*0.03*	0.02	*0.03*	0.09	*0.05*	81.47	*0.72*	2.34	*0.06*	2.01	*0.18*	2.61	*0.08*	90.96	95.52	*0.26*
900SAR2	Mt	4	0.08	*0.06*	2.32	*0.11*	0.03	*0.03*	0.01	*0.01*	0.04	*0.01*	79.78	*0.60*	2.60	*0.14*	2.12	*0.22*	2.61	*0.03*	89.58	95.45	*0.37*
900KIL2	Mt	4	0.12	*0.12*	1.84	*0.06*	0.06	*0.07*	0.04	*0.03*	0.03	*0.04*	81.17	*0.83*	2.34	*0.13*	2.14	*0.12*	2.84	*0.20*	90.57	94.85	*0.52*
900VAS2	Mt	4	0.08	*0.06*	2.07	*0.02*	0.01	*0.02*	0.04	*0.04*	0.04	*0.03*	81.26	*1.45*	2.55	*0.09*	2.16	*0.13*	2.85	*0.13*	91.05	94.85	*0.34*
900CLI2	Mt	3	0.06	*0.04*	2.71	*0.07*	0.15	*0.09*	0.04	*0.07*	0.04	*0.04*	79.74	*0.28*	3.40	*0.10*	1.40	*0.20*	3.45	*0.10*	90.99	91.67	*0.64*
800DOM2	Mt	3	2.62	*0.68*	2.71	*0.26*	0.05	*0.04*	0.28	*0.08*	0.29	*0.06*	67.64	*0.42*	1.16	*0.07*	1.94	*0.20*	14.90	*0.09*	91.60	53.57	*0.15*
	Ilm	3	0.11	*0.07*	0.15	*0.03*	0.17	*0.16*	0.06	*0.05*	0.14	*0.03*	42.58	*0.99*	1.81	*0.05*	2.77	*0.24*	46.51	*0.82*	94.31	91.37	*2.15*
800KIL2	Ilm	4	0.31	*0.23*	0.22	*0.04*	0.09	*0.12*	0.05	*0.06*	0.13	*0.04*	42.00	*0.33*	1.92	*0.12*	3.00	*0.10*	47.30	*0.39*	95.01	92.45	*0.71*
800VAS2	Ilm	3	0.17	*0.09*	0.17	*0.01*	0.12	*0.07*	0.02	*0.03*	0.10	*0.02*	41.28	*0.26*	2.20	*0.03*	3.14	*0.16*	47.49	*0.18*	94.68	92.63	*0.15*
800CLI2	Ilm	3	0.20	*0.05*	0.19	*0.04*	0.19	*0.04*	0.07	*0.03*	0.13	*0.07*	43.59	*0.59*	1.91	*0.02*	2.04	*0.08*	46.55	*0.48*	94.88	91.00	*0.75*
750CHO2	Mt	1	1.33		1.25		0.00		0.09		0.17		76.57		0.00		3.33		9.95		92.69	73.70	
750CHO3	Mt	4	0.16	*0.07*	1.05	*0.06*	0.06	*0.02*	0.04	*0.06*	0.07	*0.03*	81.93	*1.27*	0.62	*0.11*	3.55	*0.23*	3.10	*0.43*	90.58	96.43	*1.05*
750DOM3	Mt	5	0.16	*0.08*	1.29	*0.12*	0.24	*0.31*	0.01	*0.03*	0.03	*0.03*	83.19	*1.63*	0.62	*0.08*	2.56	*0.23*	1.95	*0.28*	90.06	98.34	*0.86*
750SAR3	Mt	4	0.31	*0.23*	1.01	*0.06*	0.08	*0.05*	0.05	*0.06*	0.05	*0.02*	81.89	*0.64*	0.67	*0.02*	3.07	*0.15*	3.23	*0.26*	90.35	95.13	*0.80*
750KIL3	Mt	4	0.13	*0.04*	0.93	*0.02*	0.07	*0.05*	0.03	*0.03*	0.04	*0.02*	82.99	*0.74*	0.61	*0.07*	2.95	*0.25*	2.51	*0.44*	90.25	97.26	*0.98*
750VAS3	Mt	3	0.07	*0.01*	0.96	*0.07*	0.04	*0.05*	0.17	*0.21*	0.05	*0.04*	82.73	*0.75*	0.68	*0.08*	3.11	*0.12*	2.54	*0.13*	90.36	97.43	*0.65*
750CLI3	Mt	3	0.34	*0.17*	1.08	*0.09*	0.31	*0.16*	0.06	*0.06*	0.05	*0.02*	84.03	*0.61*	0.65	*0.06*	2.08	*0.14*	2.02	*0.30*	90.64	97.13	*1.43*
800SAR3	Mt	5	0.45	*0.42*	1.80	*0.09*	0.05	*0.05*	0.01	*0.02*	0.11	*0.03*	73.93	*0.97*	0.70	*0.09*	2.38	*0.08*	11.28	*0.34*	90.71	67.62	*0.88*
800KIL3	Mt	4	0.28	*0.25*	1.67	*0.12*	0.10	*0.07*	0.05	*0.06*	0.07	*0.05*	74.78	*0.87*	0.76	*0.19*	2.28	*0.15*	11.21	*0.29*	91.19	68.03	*0.97*
800VAS3	Mt	4	0.48	*0.32*	1.86	*0.07*	0.14	*0.16*	0.03	*0.03*	0.10	*0.04*	74.24	*0.84*	0.67	*0.11*	2.06	*0.31*	11.18	*0.18*	90.77	67.50	*0.51*
800CLI3	Mt	3	0.39	*0.15*	1.98	*0.19*	0.18	*0.11*	0.03	*0.06*	0.10	*0.04*	74.13	*0.90*	0.71	*0.06*	1.65	*0.06*	10.80	*0.08*	89.97	67.87	*0.61*
775DOM2.5	Mt	1	0.71		1.62		0.08		0.16		0.12		79.26		0.99		3.20		2.75		88.91	96.80	
775VAS2.5	Mt	1	0.40		1.15		0.11		0.01		0.12		78.55		1.08		3.67		2.53		87.61	98.40	
775CLI2.5	Mt	4	0.52	*0.26*	1.26	*0.08*	0.15	*0.02*	0.02	*0.03*	0.08	*0.01*	80.85	*1.15*	1.09	*0.05*	2.41	*0.19*	2.49	*0.08*	88.84	96.30	*0.51*
825CHO4	Mt	2	0.80	*0.21*	1.35	*0.01*	0.06	*0.01*	0.03	*0.04*	0.02	*0.02*	83.34	*0.02*	0.98	*0.01*	2.95	*0.18*	3.78	*0.02*	93.30	93.35	*0.35*
825DOM4	Mt	4	0.32	*0.45*	2.10	*0.10*	0.01	*0.03*	0.02	*0.03*	0.12	*0.05*	81.33	*1.11*	1.27	*0.04*	2.10	*0.18*	5.05	*0.08*	92.31	87.80	*0.18*
825SAR4	Mt	4	0.11	*0.03*	1.83	*0.10*	0.04	*0.03*	0.02	*0.04*	0.04	*0.02*	82.36	*0.48*	1.40	*0.06*	2.29	*0.33*	4.65	*0.07*	92.72	89.55	*0.59*
825KIL4	Mt	4	0.08	*0.05*	1.66	*0.08*	0.01	*0.01*	0.03	*0.02*	0.04	*0.02*	82.39	*0.55*	1.40	*0.16*	2.09	*0.08*	5.05	*0.04*	92.74	87.68	*0.95*
825VAS4	Mt	5	0.11	*0.06*	1.88	*0.06*	0.07	*0.06*	0.03	*0.05*	0.07	*0.04*	81.96	*0.98*	1.39	*0.06*	2.28	*0.27*	4.97	*0.25*	92.75	88.50	*1.02*
825CLI4	Mt	2	0.15	*0.02*	2.17	*0.00*	0.20	*0.06*	0.07	*0.06*	0.07	*0.01*	82.19	*0.22*	1.31	*0.06*	1.49	*0.20*	4.37	*0.23*	91.99	88.95	*0.35*
700DOM3	Mt	2	0.29	*0.08*	0.86	*0.00*	0.02	*0.03*	0.00	*0.00*	0.08	*0.04*	82.70	*0.49*	0.20	*0.05*	2.37	*0.07*	4.21	*0.06*	90.72	90.85	*0.07*
700KIL3	Mt	1	0.37		0.64		0.08		0.02		0.12		83.90		0.27		1.48		4.63		91.49	88.30	

700VAS3	Mt	1	0.55	0.72	0.06	0.06	0.11	83.68	0.12	1.67	3.92	90.89	90.70

[a]Run number as in Table 9.
[b]Phase is either magnetite (Mt) or ilmenite (Ilm).
[c]Number of EMP analyses.
[d]Oxides and total of the oxides given in wt %. Numbers in italic give the statistical error on the preceding value.
[e]**Mt** or **Ilm** in mole percent; Numbers in italic give the statistical error on the preceding value.

Table 11. Experimental biotite compositions.

Run #[a]	n[b]	SiO_2		Al_2O_3		CaO		Na_2O		K_2O		FeO		MgO		MnO		TiO_2		Total[c]	Mg*[d]
800DOM2	8	35.66	*0.35*	14.03	*0.45*	0.02	*0.05*	0.74	*0.06*	8.19	*0.14*	17.57	*0.39*	11.17	*0.55*	0.45	*0.11*	4.45	*0.47*	92.26	0.53
800SAR2	4	35.75	*0.40*	14.17	*0.30*	0.00	*0.00*	0.82	*0.04*	8.34	*0.14*	17.48	*0.55*	11.63	*0.28*	0.50	*0.11*	4.09	*0.52*	92.77	0.54
800KIL2	2	35.39	*0.21*	14.07	*0.25*	0.09	*0.03*	0.80	*0.03*	8.19	*0.24*	17.27	*0.40*	11.58	*0.20*	0.34	*0.08*	4.72	*0.25*	92.45	0.55
800VAS2	4	35.49	*0.82*	13.96	*0.16*	0.04	*0.03*	0.88	*0.03*	8.14	*0.12*	16.60	*0.48*	12.11	*0.63*	0.47	*0.10*	4.53	*0.77*	92.21	0.57
800CLI2	2	35.03	*0.08*	14.98	*0.22*	0.06	*0.02*	0.93	*0.07*	8.30	*0.13*	18.04	*0.62*	10.94	*0.10*	0.48	*0.05*	4.92	*0.57*	93.68	0.52
750DOM2	1	33.40		12.81		0.35		0.44		8.46		22.08		7.80		0.00		4.27		89.61	0.39
750KIL2	1	34.12		12.42		0.88		0.82		6.85		19.81		9.21		0.90		3.22		88.24	0.45
800SAR3	3	34.51	*0.21*	14.16	*0.09*	0.06	*0.05*	0.60	*0.09*	8.39	*0.27*	19.97	*0.22*	10.36	*0.21*	0.73	*0.05*	4.41	*0.10*	93.17	0.48
800KIL3	4	35.71	*0.43*	14.25	*0.36*	0.05	*0.03*	0.98	*0.20*	7.96	*0.16*	19.24	*0.25*	9.44	*0.25*	0.75	*0.06*	4.51	*0.23*	92.86	0.47
800VAS3	1	35.20		14.51		0.24		0.77		7.96		19.61		10.04		0.76		3.90		92.98	0.48
800CLI3	2	34.64	*0.36*	14.91	*0.25*	0.16	*0.11*	0.66	*0.02*	8.26	*0.18*	19.73	*0.34*	10.20	*0.11*	0.56	*0.08*	4.23	*0.03*	93.32	0.48
775DOM2.5	2	38.93	*0.37*	14.28	*0.11*	0.14	*0.03*	0.91	*0.10*	8.53	*0.01*	12.19	*0.20*	13.51	*0.49*	1.09	*0.03*	3.60	*0.13*	93.17	0.67
775VAS2.5	2	40.50	*0.30*	14.27	*0.01*	0.23	*0.12*	1.14	*0.17*	8.31	*0.29*	11.59	*0.48*	13.78	*0.69*	1.17	*0.18*	3.39	*0.30*	94.37	0.68
775CLI2.5	2	36.97	*1.17*	13.64	*0.11*	0.27	*0.08*	0.71	*0.30*	8.97	*0.32*	12.31	*0.42*	14.11	*1.01*	0.78	*0.01*	3.59	*0.19*	91.34	0.68
825DOM4	4	35.88	*0.74*	14.48	*0.25*	0.25	*0.32*	0.66	*0.15*	8.77	*0.34*	13.98	*0.55*	14.34	*0.56*	0.56	*0.10*	4.20	*0.16*	93.12	0.65
825SAR4	3	37.17	*1.71*	14.20	*0.06*	0.10	*0.08*	0.90	*0.20*	8.69	*0.27*	13.82	*0.79*	14.25	*0.88*	0.61	*0.10*	3.62	*0.58*	93.37	0.65
825KIL4	2	35.96	*0.57*	14.45	*0.16*	0.05	*0.07*	0.81	*0.13*	8.82	*0.16*	13.85	*0.60*	15.12	*0.11*	0.61	*0.10*	4.25	*0.02*	93.90	0.67
825VAS4	4	35.51	*0.48*	14.55	*0.22*	0.03	*0.02*	0.73	*0.08*	8.72	*0.17*	14.44	*0.59*	14.68	*0.44*	0.71	*0.19*	4.20	*0.20*	93.58	0.64
750CHO4	2	35.74	*2.80*	12.92	*0.51*	0.11	*0.08*	0.54	*0.05*	8.27	*0.64*	23.49	*1.46*	6.66	*0.57*	1.33	*0.16*	4.65	*0.51*	93.71	0.34
750DOM4	3	35.75	*1.28*	14.46	*0.16*	0.04	*0.04*	0.57	*0.09*	8.37	*0.29*	24.44	*0.41*	6.42	*0.42*	0.92	*0.06*	4.55	*0.22*	95.52	0.32
750SAR4	2	36.64	*1.30*	13.73	*0.11*	0.17	*0.09*	0.73	*0.27*	8.18	*0.17*	23.60	*0.28*	6.51	*0.22*	0.90	*0.15*	4.28	*0.01*	94.72	0.33
750KIL4	3	34.90	*0.41*	14.05	*0.16*	0.13	*0.03*	0.62	*0.16*	8.28	*0.14*	24.99	*0.33*	6.42	*0.13*	0.89	*0.06*	4.52	*0.31*	94.81	0.31
750VAS4	4	35.19	*0.75*	14.07	*0.19*	0.06	*0.05*	0.58	*0.07*	8.52	*0.18*	23.81	*1.27*	6.94	*0.30*	1.03	*0.12*	4.65	*0.13*	94.83	0.35
750CLI4	3	34.32	*0.20*	13.93	*0.13*	0.22	*0.16*	0.53	*0.09*	8.68	*0.26*	24.24	*0.96*	7.07	*0.29*	0.70	*0.15*	4.56	*0.14*	94.24	0.34
750CHO3.5	1	40.21		13.47		0.07		0.96		7.90		20.85		6.56		1.05		3.98		95.05	0.36
750DOM3.5	2	35.98	*3.95*	14.32	*0.01*	0.14	*0.08*	0.79	*0.40*	8.19	*0.54*	23.04	*2.82*	6.00	*1.37*	0.97	*0.04*	4.07	*0.73*	93.48	0.32
750SAR3.5	1	38.95		14.62		0.16		0.98		8.33		21.91		6.57		0.94		4.04		96.50	0.35
750KIL3.5	4	37.42	*1.84*	13.98	*0.24*	0.17	*0.04*	0.85	*0.17*	7.88	*0.68*	22.86	*1.70*	5.56	*0.43*	1.00	*0.08*	3.94	*0.46*	93.66	0.30
750VAS3.5	1	38.98		13.53		0.30		1.32		7.59		21.19		4.65		0.99		3.47		92.01	0.28
750CLI3.5	1	35.86		14.12		0.35		0.62		8.33		23.89		6.75		0.67		4.39		94.98	0.34
700DOM3	1	42.16		13.23		0.29		0.81		7.55		21.37		5.95		1.62		3.20		96.16	0.33

[a]Run number as in Table 9.
[b]Number of EMP analyses.
[c]Oxides and total given in wt %; Numbers in italic give the statistical error on the preceding value.
[d]**Mg*** = [Mg/(Mg+Fe)] in mol %.

Table 12. Experimental clinopyroxene compositions.

Run #[a]	n[b]	SiO_2		Al_2O_3		CaO		Na_2O		K_2O		FeO		MgO		MnO		TiO_2		Total[c]	Wo[d]	En[d]	Fs[d]
800KIL2	4	49.40	*0.93*	2.31	*1.00*	21.22	*0.18*	0.56	*0.20*	0.07	*0.01*	10.47	*1.18*	11.27	*0.60*	1.41	*0.23*	0.73	*0.21*	97.43	45.96	33.94	20.10
800VAS2	8	50.33	*1.01*	1.70	*0.76*	21.52	*0.32*	0.44	*0.13*	0.05	*0.03*	10.58	*0.61*	11.44	*0.43*	1.36	*0.17*	0.66	*0.28*	98.07	46.01	34.03	19.96
750CHO2	5	49.22	*0.75*	3.82	*0.74*	19.44	*0.59*	1.35	*0.21*	0.33	*0.16*	13.65	*0.92*	7.64	*0.45*	3.24	*0.55*	1.19	*0.33*	99.89	44.91	24.58	30.51
750SAR2	5	48.86	*1.30*	2.30	*0.69*	20.40	*0.63*	0.94	*0.14*	0.08	*0.06*	14.95	*1.17*	7.57	*0.44*	3.31	*0.36*	0.97	*0.36*	99.39	45.11	23.31	31.58
750KIL2	1	53.10		4.32		18.42		1.82		0.60		12.75		7.75		2.24		0.61		101.62	45.00	26.35	28.65
750VAS2	1	48.61		5.19		17.72		1.92		0.88		11.36		7.09		2.83		2.39		97.99	45.81	25.49	28.70
750CHO3	8	48.59	*1.39*	4.52	*0.61*	19.25	*0.94*	1.54	*0.13*	0.29	*0.25*	10.15	*0.87*	9.97	*0.35*	2.98	*0.38*	0.97	*0.31*	98.26	44.36	31.99	23.65
750SAR3	3	49.08	*1.02*	4.34	*0.21*	19.88	*0.28*	1.47	*0.09*	0.16	*0.02*	11.41	*0.82*	9.30	*0.32*	2.64	*0.63*	0.66	*0.28*	98.94	45.37	29.54	25.09
750KIL3*	1	56.47		11.58		10.01		3.11		2.41		5.70		4.52		1.26		1.03		96.09	46.05	28.89	25.06
750VAS3	4	48.21	*1.83*	7.42	*0.84*	17.93	*2.03*	1.88	*0.29*	0.76	*0.46*	10.40	*1.04*	8.01	*0.79*	1.93	*0.30*	1.85	*0.36*	98.37	46.29	28.80	24.91
750CLI3	1	49.70		6.67		17.67		1.64		1.01		7.77		8.66		1.16		0.98		95.25	48.14	32.83	19.03
750CLI3*	1	57.18		10.47		11.40		2.99		2.09		6.22		5.65		1.06		0.38		97.43	45.69	31.49	22.82
775CHO2.5	1	48.61		2.73		19.60		0.88		0.04		16.02		7.41		2.83		0.49		98.62	43.89	23.10	33.01
775SAR2.5	1	48.55		2.76		20.85		1.19		0.07		10.88		9.92		2.55		1.10		97.87	46.17	30.57	23.26
775VAS2.5	1	48.29		4.47		17.94		1.25		0.76		7.81		8.59		1.84		3.25		94.18	47.92	31.92	20.16
775CLI2.5	1	48.95		5.62		19.49		0.97		0.57		10.24		9.60		1.29		1.29		98.02	46.57	31.90	21.53
825KIL4	3	49.72	*0.99*	2.66	*0.53*	21.37	*0.58*	0.89	*0.08*	0.20	*0.08*	10.48	*1.32*	10.96	*1.33*	1.32	*0.40*	0.59	*0.12*	98.18	46.62	33.20	20.18
750CHO4	4	49.07	*0.41*	1.88	*0.31*	20.45	*0.57*	0.84	*0.11*	0.10	*0.06*	17.10	*0.57*	6.62	*0.16*	3.30	*0.36*	0.93	*0.27*	100.27	44.84	20.18	34.98
750SAR4	4	47.80	*0.58*	3.01	*0.44*	21.34	*0.23*	0.71	*0.05*	0.04	*0.03*	17.44	*0.39*	6.12	*0.19*	2.21	*0.22*	0.88	*0.19*	99.56	47.20	18.84	33.96
750KIL4*	2	56.22	*0.96*	11.12	*0.20*	11.87	*0.01*	2.19	*0.21*	2.63	*0.61*	9.98	*0.34*	2.87	*0.36*	1.54	*0.11*	1.00	*0.11*	99.40	47.78	16.01	36.21
750VAS4	1	43.97		5.87		21.27		0.95		0.04		16.45		5.91		2.03		2.17		98.65	48.40	18.72	32.88
750CLI4*	2	52.14	*2.39*	7.88	*0.80*	16.14	*1.80*	1.85	*0.17*	1.02	*0.32*	11.93	*1.95*	5.80	*0.05*	1.16	*0.04*	1.20	*0.50*	99.09	46.85	23.53	29.62
700CHO3	2	54.35	*1.99*	6.34	*1.00*	13.26	*1.35*	1.69	*0.43*	1.33	*0.54*	12.27	*0.21*	4.44	*0.21*	3.11	*0.11*	0.35	*0.17*	97.12	42.09	19.62	38.29
700SAR3	3	47.29	*0.56*	3.13	*0.27*	18.91	*0.40*	1.29	*0.02*	0.23	*0.11*	15.59	*0.73*	6.35	*0.56*	4.14	*0.27*	1.22	*0.39*	98.16	43.79	20.43	35.78
700VAS3	3	45.98	*4.96*	5.38	*1.36*	16.80	*1.98*	1.83	*0.06*	0.62	*0.72*	11.22	*0.71*	7.60	*0.77*	3.06	*0.49*	1.89	*0.09*	94.38	43.52	27.44	29.04
750CHO3.5	5	49.47	*0.57*	2.02	*0.51*	20.07	*0.52*	0.85	*0.16*	0.16	*0.07*	15.73	*0.26*	6.99	*0.20*	3.30	*0.32*	0.51	*0.18*	99.10	44.92	21.79	33.29
750SAR3.5	4	47.86	*1.02*	3.77	*0.57*	20.07	*1.11*	1.02	*0.16*	0.24	*0.20*	15.94	*0.73*	6.09	*0.32*	2.22	*0.23*	0.77	*0.07*	98.00	46.94	19.83	33.23

[a]Run number as in Table 9. Samples followed by an asterisk give compositions intermediate between clinopyroxene and amphibole, probably resulting from intergrowths of both phases;

[b]Number of EMP analyses

[c]Oxides and total given in wt %. Numbers in italic give the statistical error on the preceding value.

[d]**Wo**, **En**, and **Fs** are the mole percents of wollastonite, enstatite, and ferrosilite, respectively.

Table 13. Experimental amphibole compositions.

Run #[a]	n[b]	SiO_2		Al_2O_3		CaO		Na_2O		K_2O		FeO		MgO		MnO		TiO_2		Total[c]	[4]Al[d]	SumA[d]	Mg*[d]
900CLI2	3	41.71	*0.70*	11.36	*0.36*	11.53	*0.09*	2.54	*0.11*	1.06	*0.02*	9.81	*0.55*	14.52	*0.42*	0.47	*0.09*	2.91	*0.13*	95.91	1.75	0.90	0.73
800CLI2	6	39.87	*0.83*	11.48	*0.52*	11.15	*0.16*	2.47	*0.14*	1.01	*0.08*	15.89	*0.33*	9.27	*0.17*	0.61	*0.10*	3.10	*0.09*	94.84	1.77	0.83	0.51
800VAS3	4	39.21	*0.31*	10.91	*0.24*	10.89	*0.09*	2.44	*0.06*	1.24	*0.04*	18.14	*0.57*	8.45	*0.13*	1.18	*0.22*	2.93	*0.16*	95.37	1.81	0.95	0.45
800CLI3	5	39.30	*0.57*	11.46	*0.70*	11.17	*0.20*	2.28	*0.10*	1.12	*0.08*	17.93	*0.51*	8.87	*0.16*	0.81	*0.05*	2.72	*0.24*	95.65	1.84	0.92	0.47
825VAS4	4	39.76	*0.75*	11.14	*0.47*	11.54	*0.08*	2.61	*0.05*	1.35	*0.10*	14.47	*0.82*	11.55	*0.38*	1.08	*0.11*	2.71	*0.14*	96.19	1.87	1.07	0.59
825CLI4	5	39.80	*0.75*	12.13	*0.52*	11.79	*0.32*	2.36	*0.09*	1.21	*0.18*	14.69	*0.97*	11.69	*0.72*	0.65	*0.09*	2.53	*0.34*	96.84	1.93	1.02	0.59

[a]Run number as in Table 9.
[b]Number of EMP analyses.
[c]Oxides and total given in wt %; Numbers in italic give the statistical error on the preceding value.
[d]**[4]Al** and **SumA** are the tetra-coordinated Al (in mol %) and the number of cations in the A site, respectively (calculation on the basis of 23 O with all Fe as FeO, after Richard & Clarke, 1990); **Mg*** = [Mg/(Mg+Fe)].

Table 14. Experimental feldspar compositions.

Run #[a]	Phase[b]	n[c]	SiO_2		Al_2O_3		CaO		Na_2O		K_2O		FeO		MgO		MnO		TiO_2		Total[d]	Or[e]	An[e]	Ab[e]
800CLI2	Pl	5	56.60	*0.38*	26.41	*0.24*	8.58	*0.19*	6.24	*0.08*	0.43	*0.04*	0.48	*0.18*	0.03	*0.02*	0.06	*0.06*	0.02	*0.02*	98.84	2.50	42.09	55.41
750CHO2	Afs	6	65.07	*0.87*	19.56	*0.30*	1.14	*0.26*	6.48	*0.68*	6.29	*1.05*	0.42	*0.11*	0.01	*0.01*	0.01	*0.01*	0.05	*0.05*	99.01	36.83	5.60	57.57
750DOM2	Pl	2	63.18	*0.06*	21.87	*0.88*	3.75	*0.74*	8.14	*0.47*	1.91	*0.45*	0.70	*0.36*	0.09	*0.09*	0.00	*0.00*	0.02	*0.02*	99.66	11.05	17.98	70.97
	Afs	1	65.41		17.96		0.78		4.60		7.22		0.87		0.03		0.00		0.37		97.23	48.57	4.38	47.05
750SAR2	Afs	1	64.95		19.76		1.60		6.67		5.56		0.98		0.02		0.00		0.13		99.67	32.60	7.91	59.49
750KIL2	Afs	4	66.11	*0.42*	19.95	*0.22*	1.47	*0.58*	7.27	*0.89*	5.01	*1.72*	0.32	*0.15*	0.01	*0.01*	0.02	*0.02*	0.02	*0.02*	100.17	29.01	7.11	63.88
750VAS2	Afs	1	65.85		18.72		0.32		4.96		8.99		0.55		0.03		0.00		0.08		99.50	53.53	1.59	44.88
750CLI2	Pl	2	60.25	*0.30*	22.15	*0.78*	5.24	*0.46*	7.65	*0.37*	1.13	*0.30*	1.02	*0.09*	0.03	*0.01*	0.09	*0.09*	0.04	*0.01*	97.56	6.53	25.70	67.77
750DOM3	Pl	1	62.94		22.16		4.20		7.57		2.07		0.51		0.01		0.00		0.07		99.53	12.09	20.64	67.27
750SAR3	Pl	1	61.99		22.06		4.29		7.78		1.58		0.70		0.00		0.00		0.11		98.52	9.31	21.21	69.48
750KIL3	Afs	2	64.04	*0.25*	18.94	*0.22*	0.44	*0.07*	4.08	*0.08*	9.94	*0.11*	0.29	*0.01*	0.04	*0.04*	0.00	*0.00*	0.01	*0.01*	97.76	60.22	2.23	37.55
	Pl	1	61.72		21.78		4.08		7.46		2.00		0.85		0.29		0.02		0.00		98.21	11.92	20.44	67.64
750VAS3	Afs	1	63.98		18.91		0.41		3.98		10.09		0.35		0.01		0.10		0.00		97.82	61.25	2.08	36.67
	Pl	1	60.91		22.47		4.14		7.69		1.69		0.98		0.47		0.03		0.17		98.54	10.05	20.62	69.33
750CLI3	Pl	1	64.04		22.23		4.03		8.33		1.82		0.69		0.00		0.00		0.00		101.15	10.17	18.96	70.87
800CLI3	Pl	4	57.95	*0.72*	25.32	*0.36*	7.23	*0.31*	6.89	*0.18*	0.57	*0.04*	0.34	*0.10*	0.03	*0.03*	0.03	*0.03*	0.04	*0.03*	98.39	3.31	35.49	61.20
775DOM2.5	Pl	4	62.14	*0.55*	21.00	*0.49*	3.62	*0.41*	7.63	*0.10*	2.52	*0.35*	0.54	*0.07*	0.04	*0.03*	0.07	*0.07*	0.04	*0.03*	97.60	14.71	17.72	67.57
775SAR2.5	Pl	5	62.59	*0.30*	21.24	*0.28*	3.82	*0.35*	8.05	*0.11*	1.88	*0.18*	0.82	*0.28*	0.06	*0.05*	0.07	*0.07*	0.06	*0.05*	98.58	10.86	18.49	70.65
775VAS2.5	Pl	4	61.90	*0.39*	21.29	*0.76*	3.79	*0.46*	7.94	*0.21*	1.79	*0.38*	0.84	*0.21*	0.01	*0.01*	0.04	*0.04*	0.06	*0.03*	97.65	10.55	18.67	70.78
775CLI2.5	Pl	2	63.09	*0.18*	21.69	*0.28*	4.11	*0.16*	7.61	*0.35*	2.37	*0.52*	0.60	*0.41*	0.00	*0.00*	0.06	*0.05*	0.00	*0.00*	99.51	13.66	19.84	66.50
750DOM4	Pl	4	62.54	*0.33*	21.94	*0.67*	4.36	*0.17*	8.12	*0.20*	1.22	*0.19*	0.17	*0.20*	0.01	*0.01*	0.06		0.03		98.44	7.10	21.25	71.65
750SAR4	Pl	3	62.11	*0.57*	21.63	*0.74*	4.32	*0.38*	7.65	*0.30*	1.70	*0.77*	0.30	*0.08*	0.00	*0.00*	0.06	*0.06*	0.07	*0.02*	97.85	10.02	21.42	68.56
750KIL4	Pl	1	61.88		21.08		4.18		7.81		1.48		0.81		0.01		0.07		0.10		97.41	8.76	20.83	70.41
750VAS4	Pl	2	62.57	*1.06*	21.75	*0.37*	4.36	*0.40*	7.74	*0.56*	1.49	*0.33*	0.67	*0.11*	0.02	*0.02*	0.08	*0.08*	0.07	*0.05*	98.77	8.87	21.63	69.50
750CLI4	Pl	5	62.16	*1.02*	22.17	*0.67*	4.95	*0.55*	7.76	*0.29*	1.26	*0.14*	0.90	*0.50*	0.04	*0.04*	0.04	*0.04*	0.11	*0.01*	99.38	7.31	24.15	68.54
700CHO3	Afs	2	63.53	*0.14*	18.24	*0.65*	0.42	*0.11*	4.99	*0.26*	9.22	*0.34*	0.53	*0.20*	0.09	*0.06*	0.01	*0.01*	0.04	*0.04*	97.06	53.76	2.09	44.15
700DOM3	Afs	1	64.33		18.67		0.59		5.21		9.03		0.47		0.16		0.04		0.34		98.84	51.75	2.86	45.39
700SAR3	Afs	1	63.59		17.94		1.17		5.93		6.82		1.49		0.13		0.13		0.54		97.75	40.57	5.87	53.56
	Pl	2	64.01	*0.42*	20.17	*1.08*	2.78	*0.57*	8.86	*0.34*	2.13	*0.33*	1.09	*0.37*	0.09	*0.09*	0.17	*0.01*	0.11	*0.08*	99.40	11.93	12.97	75.10
700KIL3	Afs	2	64.75	*0.52*	19.23	*0.07*	1.16	*0.08*	7.58	*1.20*	5.68	*1.45*	0.64	*0.06*	0.09	*0.02*	0.00	*0.00*	0.04	*0.02*	99.16	31.30	5.37	63.33
700VAS3	Pl	1	63.45		19.61		2.30		9.07		3.05		0.82		0.25		0.02		0.05		98.62	16.27	10.29	73.44
750DOM3.5	Pl	1	62.58		22.87		4.46		7.88		1.24		0.30		0.00		0.00		0.00		99.34	7.33	22.09	70.58
750SAR3.5	Pl	4	62.13	*0.62*	21.56	*0.78*	4.08	*0.41*	7.48	*0.22*	2.00	*0.68*	0.69	*0.22*	0.03	*0.02*	0.06	*0.05*	0.10	*0.09*	98.11	11.88	20.44	67.68
750KIL3.5	Pl	1	63.89		21.11		3.20		7.30		2.51		0.57		0.05		0.11		0.02		98.75	15.42	16.50	68.08
750VAS3.5	Pl	2	61.37	*0.47*	21.61	*0.14*	4.09	*0.06*	7.97	*0.16*	1.40	*0.23*	1.22	*0.52*	0.05	*0.05*	0.03	*0.03*	0.45	*0.23*	98.17	8.26	20.28	71.46

[a]Run number as in Table 9.
[b]Phase is either plagioclase (Pl) or alkali feldspar (Afs).
[c]Number of EMP analyses.
[d]Oxides and total given in wt %; Numbers in italic give the statistical error on the preceding value.
[e]**Or**, **An**, and **Ab** orthoclase, anorthite, and albite in mol %, respectively.

Table 15. Experimental glass compositions.

Sample[a]	n[b]	SiO_2	Al_2O_3	CaO	Na_2O	K_2O	FeO	MgO	MnO	TiO_2	Mg*[c]	P.I.[d]
900CHO2	7	68.84	16.08	0.91	6.84	5.23	1.51	0.17	0.18	0.25	0.10	1.08
900DOM2	7	67.24	16.94	1.34	6.85	5.03	1.67	0.39	0.15	0.39	0.19	0.98
900SAR2	6	65.77	17.36	1.64	7.27	4.96	1.86	0.45	0.29	0.39	0.20	1.00
900KIL2	5	64.79	17.75	1.88	7.60	4.75	2.03	0.44	0.21	0.54	0.18	0.99
900VAS2	6	64.17	17.69	2.48	7.23	4.63	2.29	0.52	0.51	0.48	0.19	0.95
900CLI2	6	64.38	18.10	2.74	6.88	4.32	2.08	0.70	0.24	0.54	0.25	0.88
800CHO2	5	68.71	16.07	0.97	7.00	5.12	1.43	0.19	0.26	0.25	0.12	1.06
800DOM2	4	67.36	16.99	1.31	6.68	4.77	2.06	0.26	0.19	0.38	0.11	0.95
800SAR2	5	66.56	17.32	1.58	6.81	4.65	2.23	0.26	0.24	0.36	0.10	0.93
800KIL2	5	65.70	17.71	1.60	7.45	4.42	2.36	0.25	0.15	0.38	0.09	0.96
800VAS2	5	65.29	17.68	1.85	7.48	4.52	2.33	0.32	0.16	0.37	0.12	0.97
800CLI2	5	66.24	17.82	2.22	6.66	4.24	2.14	0.25	0.13	0.32	0.10	0.87
750CHO2	4	72.08	15.61	0.48	5.47	5.07	1.10	0.03	0.07	0.10	0.03	0.93
750DOM2	3	72.88	15.76	0.73	4.52	4.91	0.93	0.05	0.07	0.14	0.05	0.81
750SAR2	3	72.16	15.81	0.74	4.71	5.16	1.27	0.01	0.00	0.14	0.01	0.84
750CHO3	6	70.88	16.46	0.69	5.29	5.30	0.94	0.09	0.20	0.16	0.09	0.88
750DOM3	4	71.28	16.73	0.93	5.42	4.54	0.84	0.02	0.10	0.14	0.02	0.82
750SAR3	4	71.02	16.82	0.92	5.27	4.69	0.91	0.06	0.11	0.19	0.06	0.82
750KIL3	3	69.75	17.24	1.00	6.19	3.86	1.37	0.25	0.13	0.22	0.15	0.83
750VAS3	2	70.40	17.12	0.99	6.14	4.10	0.95	0.03	0.22	0.05	0.03	0.85
800CHO3	5	69.87	16.61	0.94	5.23	5.17	1.51	0.15	0.28	0.26	0.09	0.85
800SAR3	4	69.06	18.21	1.89	5.19	4.52	0.96	0.00	0.01	0.15	0.00	0.74
800KIL3	4	68.48	18.39	1.44	5.67	4.53	0.96	0.01	0.18	0.34	0.01	0.77
800VAS3	3	68.16	18.59	1.79	5.61	4.26	1.16	0.02	0.24	0.17	0.02	0.74
800CLI3	4	68.96	18.51	1.91	5.15	4.20	0.98	0.02	0.09	0.18	0.02	0.70
775CHO2.5	6	71.14	16.44	0.67	5.22	5.24	0.98	0.01	0.14	0.16	0.01	0.87
775DOM2.5	2	71.55	16.76	0.93	4.66	5.06	0.67	0.01	0.23	0.13	0.01	0.78
775SAR2.5	2	71.64	16.84	0.93	4.65	4.73	0.87	0.09	0.12	0.13	0.09	0.76
775VAS2.5	4	71.32	17.29	0.88	4.82	4.28	1.06	0.01	0.18	0.16	0.01	0.72
775CLI2.5	4	72.19	16.73	1.10	4.27	4.35	1.03	0.06	0.06	0.22	0.05	0.70
825CHO4	6	70.32	16.23	0.91	5.24	5.17	1.54	0.16	0.22	0.21	0.09	0.87
825DOM4	6	69.08	17.17	1.33	5.51	5.05	1.24	0.11	0.19	0.33	0.08	0.84
825SAR4	4	68.69	17.62	1.57	5.57	4.71	1.23	0.12	0.11	0.38	0.09	0.81
825KIL4	4	67.16	18.07	1.66	6.04	4.80	1.48	0.20	0.27	0.32	0.12	0.84
825VAS4	6	67.44	18.20	1.78	5.86	4.68	1.41	0.13	0.14	0.36	0.08	0.81
825CLI4	3	67.51	18.79	2.42	5.01	4.27	1.30	0.21	0.13	0.37	0.14	0.68
750CHO4	4	72.07	16.35	0.81	4.50	5.14	0.78	0.01	0.21	0.13	0.01	0.79
750DOM4	4	71.32	17.11	1.43	4.74	4.43	0.69	0.00	0.14	0.14	0.00	0.73
750SAR4	4	70.40	17.29	1.49	5.55	3.96	0.99	0.00	0.13	0.18	0.00	0.77
750KIL4	5	69.64	17.81	1.29	7.12	3.32	0.64	0.00	0.09	0.09	0.00	0.86
750VAS4	4	70.23	17.70	1.32	6.20	3.59	0.68	0.05	0.15	0.08	0.07	0.79
750CLI4	1	71.60	17.39	1.89	5.15	3.27	0.57	0.00	0.00	0.13	0.00	0.69
700CHO3	3	75.18	14.61	0.35	4.54	4.37	0.75	0.02	0.10	0.08	0.03	0.83
750CHO3.5	4	70.80	16.47	0.76	5.36	5.40	1.05	0.02	0.06	0.08	0.02	0.89
750DOM3.5	3	70.84	17.34	1.12	5.19	4.63	0.59	0.01	0.18	0.10	0.02	0.78
750SAR3.5	2	70.41	17.37	1.46	5.15	4.49	0.85	0.03	0.17	0.07	0.03	0.77
750KIL3.5	2	69.64	17.75	1.05	7.30	3.31	0.75	0.00	0.13	0.07	0.00	0.88
750VAS3.5	2	69.40	17.38	1.24	6.97	3.75	0.98	0.03	0.19	0.07	0.03	0.89
750CLI3.5	1	72.16	17.61	1.37	4.52	3.65	0.43	0.02	0.17	0.08	0.04	0.64

[a]Run number as in Table 9.
[b]Number of EMP analyses.
[c]**Mg*** = [MgO/(MgO+FeO)], with an error of 0,01.
[d]Peralkalinity Index given as molar [$(Na_2O+K_2O)/Al_2O_3$].

Oxides given in wt %, recalculated on anhydrous basis.

Table 16. Water content in parental basalts calculated from the model of fractional crystallisation of Maury *et al.* (1980).

Parental magma (SiO_2)[a]	**CDP1 (47.2)**	**CDP2 (48.5)**	**CDP3 (52.2)**	**CDP4 (53.1)**	**CDP5 (57.1)**
Derived magma (SiO_2)[a]	CDP2 (48.5)	CDP3 (52.2)	CDP4 (53.1)	CDP5 (57.1)	CDP6 (60.2)
F[a]	*74.7*	*64.3*	*79.7*	*67.9*	*75.0*
Olivine	4.1	0.9			
Pyroxene	10.0	15.4	10.0	2.9	2.1
Magnetite	1.7	3.8		6.6	5.7
Amphibole		6.6	4.6	9.5	14.7
Plagioclase	9.1	9.5	6.2	15.0	
Bulk H_2O[b]	**1.5**	**2.0**	**2.9**	**3.5**	**4.9**

[a]The formulation is based on the repartition of Si, Ti, Al, Fe, Mg, Ca, Na, K, and is calculated following the least-square method; it calculates for each step the weight percentages of derived magma (*F*) and fractionated minerals from parental magma with a precision ~2 %; CDP1 to CPD7 are magma compositions given in Maury *et al.* (1980), with bulk SiO_2 in wt % reported in brackets.

[b]Bulk H_2O content (in wt %) of the parental magma, starting with a bulk H_2O content of 6.4 wt % in the trachytes (CDP6, close to CLI sample) corresponding to 8 wt % in the melt in thermodynamic equilibrium with ~20 wt % phenocrysts (Table 2).